2018

Non-Hermitian Optics

Absar Ulhassan
University of Central Florida

NON-HERMITIAN OPTICS

by

ABSAR ULHASSAN

B.S. Lahore University of Management Sciences, 2013
M.S. University of Central Florida, 2015

A dissertation submitted in partial fulfillment of the requirements
for the degree of Doctor of Philosophy
in CREOL/The College of Optics & Photonics
at the University of Central Florida
Orlando, Florida

Summer Term
2018

Major Professor: Demetrios N. Christodoulides

ABSTRACT

From the viewpoint of quantum mechanics, a system must always be Hermitian since all its corresponding eigenvalues must be real. In contrast, the eigenvalues of open systems-unrestrained because of either decay or amplification-can be in general complex. Not so long ago, a certain class of *non-Hermitian* Hamiltonians was discovered that could have a completely real eigenvalue spectrum. This special class of Hamiltonians was found to respect the property of commutation with the parity-time (PT) operator. Translated into optics, this implies a balance between regions exhibiting gain and loss. Traditionally, loss has been perceived as a foe in optics and something that needs to be avoided at all costs. As we will show, when used in conjunction with gain, the presence of loss can lead to a host of counterintuitive outcomes in such non-Hermitian configurations that would have been otherwise unattainable in standard arrangements. We will study PT symmetric phase transitions in various optical settings that include semiconductor microrings and coupled fiber cavities, and show how they can allow mode-selectivity in lasers. One of the key outcomes of this effort was the realization of higher order degeneracies in a three-cavity laser configuration that can exhibit orders-of-magnitude larger sensitivity to external perturbations. We will also consider systems that display nonlinear effects such as gain saturation, thus allowing novel phase transitions. Some interesting properties associated with degeneracies in non-Hermitian settings will be investigated as well. Such degeneracies, called exceptional points (EPs), are much more drastic compared to standard degeneracies of eigenvalues because the corresponding eigenvectors also coalesce, which in turn reduces the dimensionality of the phase space. We will show that dynamic parameter contours enclosing or close to EPs can lead to a

robust chiral mode conversion process – something that can be potentially used to realize omni-polarizing optical devices.

ACKNOWLEDGMENTS

I would first like to thank my advisor, Dr. Demetrios Christodoulides for always being a source of inspiration for me. I really enjoyed having lengthy discussions with him on a wide range of topics, most importantly those within the realm of optics, but also those concerned with life, ethics, philosophy and religion. I appreciate his willingness to share his curiosities and also to let me express my ideas. I have learned many qualities from him, and in my opinion, humility is one that stands out among them – something that is the mark of all great scientists. Through my interaction with him over these years, I have discovered that the surest way to tread the scientific path is by remaining ever curious: always keeping an eye open for new avenues and not limiting yourself to a certain theme, even if you are good at it.

During my time at CREOL, I got the chance of collaborating with a number of remarkable people. It was an honor for me to have Professors Khajavikhan, LiKamWa and Kaup on my committee. I have thoroughly enjoyed and benefited from discussing ideas with them. I was never good on the experimental side and truly appreciate spending time in the lab with Dr. LiKamWa and Dr. Khajavikhan. Advice and support given by Dr. Kaup also goes a long way in shaping up my career. I would also like to sincerely thank my friends at CREOL for all the good times that they brought along with them, for all the fun and discussions and arguments. They include, but are not limited to: Amin, Billy, Midya, Fan, Nick, Helena, Ali Kazemi, Jinhan, Gisella, Ali Miri, Hossein, Sara, Muhammad, Monica, Alma and Rachel.

In the end, I would like to thank my parents and my brother for being immensely supportive during these years and would finally like to thank Allah for everything that He gave me.

TABLE OF CONTENTS

LIST OF FIGURES

only after removing the loss segment. (b**)**, A model composed of discrete components to replace the continuum model in (a): the interfaces are replaced with localized mirrors, and the distributed gain and loss are replaced with lumped components – an amplifier (amplification factor G) and an attenuator (attenuation factor $\mathcal{L}$), respectively. PT-symmetry requires that $R1 = R3 = R$. The cavity corresponding to the gain layer alone is formed of the side mirrors containing the amplifier. (c), Schematic of an experimental realization of the system shown on the left in (b) using single-mode optical fibers. Specially designed fiber Bragg grating (FBGs) are used as partially reflecting mirrors with reflectivies R, $R2$, and R from left to right. Gain is provided by a semiconductor optical amplifier (SOA) and attenuation by a variable optical attenuator (VOA). (d), Optical setup in (c) after inserting an additional 1-km-long fiber spool. A polarization controller (PC) is added to maintain the state of polarization throughout the cavity. 70

Figure 3.15 (a), Without detuning, the resonance frequencies of the gain (red) and lossy (blue) sub-cavities are aligned. (b), In the presence of detuning Δ, the sub-cavity resonances are no longer aligned. (c) Gaussian or (d) Uniform distributions as candidates for the detuning probability distribution $P(\Delta)$ (e)-(f), Trajectories of (e) the real and (f) imaginary components of the eigenvalues $\lambda 1,2$ for a linear PT-symmetric configuration $g + \gamma 1 = \gamma 2$. Dashed curves represent $\Delta = 0$, and solid curves depict $\Delta = \omega FSR/10$. Shaded regions correspond to all the intermediate detuning values. As g increases, Reλ tend to coalesce whereas Imλ bifurcate. The exceptional point at zero-detuning (yellow triangle) occurs at $g = \kappa$, whereupon Re$\lambda = 0$ and Im$\lambda = \gamma 1$. We define a transition between an unbroken PT-symmetric phase (U) and a broken PT-symmetric phase (B) at the EP. Lasing occurs when Im$\lambda < 0$, which may occur before or after the bifurcation. The green circle depicts the experimental values for the lasing threshold corresponding to $R2 = 6.8\%$. Inset in (e) shows the PT-cavity configuration. (g), A general schematic for the lasing domains is provided when $\gamma 1 = 0$. Along the dotted line, the PT-symmetric condition $g = \gamma 2$ is satisfied and the dashed line corresponds to $g + \gamma 2 = 2\kappa$. From Eq. (3.61), the system is in the unbroken domain if $g < 2\kappa - \gamma 2$ – circles, and is instead in the broken domain beyond this region – edges. The lasing and non-

CHAPTER 1. INTRODUCTION

It is commonly believed that real eigenvalues of an observable are associated with a Hermitian operator [1], where Hermiticity or self-adjointness for an operator $\hat{O}$ means that the transpose-conjugate of the matrix representation for this operator leaves it unchanged i.e. $\hat{O}^{\dagger} = \hat{O}$. But there were a few numerical studies that hinted at the possibility of having the spectrum of an observable as real and positive even when the operator was non-Hermitian. An example was $H = p^2 + x^2 + ix^3$ studied by Bessis [2]. Later on, Bender and Boettcher discovered that such a Hamiltonian in fact belonged to a wide class of non-Hermitian Hamiltonians that exhibit entirely real spectra - Hamiltonians that commute with the parity-time ($\hat{P}\hat{T}$) operator [2]. This means that all the eigenfunctions of the operator are simultaneously eigenfunctions of the PT operator [3]. Using the notation $(\hat{p}, \hat{x})$ for momentum and space respectively, the action of the parity operator $\hat{P}$ is defined by the relations $\hat{p} \to -\hat{p}, \hat{x} \to -\hat{x}$ while that of the time operator $\hat{T}$ by $\hat{p} \to -\hat{p}, \hat{x} \to \hat{x}, i \to -i$. Realizing non-Hermitian systems of a quantum nature are still a matter of debate, however, optics has proven to be a productive domain for their study. The main reason for this is the isomorphism between the Schrödinger equation and the paraxial wave equation. Gain and loss are the most basic ingredients that constitute non-Hermiticity – damping (loss) is inherent in optical waveguides due to absorption/scattering effects and amplification (gain) is also not difficult to implement, it can be introduced by optical/electric pumping mechanisms in a suitable gain material. In recent times, a flurry of research in this field has led to the demonstration of PT-symmetric effects in systems ranging from optics [4-9] to electronics [10-12] and even in acoustics [13,14]. Some intriguing possibilities have been suggested; including solitons in PT lattices [15], Bloch oscillations [16], unidirectional invisibility [17]; and also demonstrated [18-22]. Such realizations have triggered a significant amount of activity and more possibilities are coming to the front with time. One of them is that of obtaining super-sensitivity. This relies on the fact that a class of highly interesting mathematical entities, known as exceptional points (EPs), are inherent to such non-Hermitian systems. Chapters 2 and 3 are dedicated to both linear and nonlinear PT-symmetric optical structures, with

a focus on how we can utilize this concept to obtain some desired properties such as enhanced detection capabilities and mode filtering.

The physical reason why the phenomenon is called PT 'symmetry' is that the modes in such structures are symmetrically divided (intensity-wise) in the comprising channels, for example, the optical intensity profiles in two coupled waveguides will be exactly the same even though one of them is providing gain and the other one loss. But if the gain-loss contrast is too high, this symmetry vanishes and there is an unequal distribution of the field in the two waveguides. Moreover, in the symmetric regime, although the eigenvalues are real, the vector space in such non-Hermitian settings is skewed since the eigenvectors are no longer orthogonal. If the Hamiltonian H depends on a parameter ϵ, that is a measure of its 'non-Hermiticity,' after a certain threshold value for ϵ [2] a sharp symmetry-breaking transition occurs and as a result, the eigenvalues of the system cease to be entirely real – causing a net amplification/loss. In addition, this transition to the broken PT-symmetry phase is associated with a passage through an exceptional point in the parameter space [7]. At an EP not only do the eigenvalues coalesce but so do the corresponding eigenvectors. Appearance of a degeneracy in the eigenvectors is in stark contrast from Hermitian systems that are known to only support degeneracies in the eigenvalues at so-called diabolic points (DPs) [23-25].

In Chapter 2, the benefits afforded by these EPs will be studied in some detail with a special emphasis on the eigenvalue bifurcation upon a slight perturbation around such points. These bifurcations are found to be proportional to $\varepsilon^{1/N}$ where ε is the perturbation and N is the order of the EP. An immediate conclusion derivable from this behavior is the possibility of using EPs in enhancing the sensitivity of detection. The fact that $\varepsilon^{1/N} \gg \varepsilon$ leads to a major advantage compared to regular optical setups such as high-Q micro-cavities where the locations of resonances vary on the order of ε. These schemes have been abundantly used in the past for biosensing [26, 27] and detecting nanoparticles in a small monitored region [28, 29]. For demonstrating the advantage of using exceptional points, we first study a second order system. The most straightforward realization of this is through a coupled dimer of micro-cavities. We will show by numerical simulations that operating this system close to the EP results in a much larger change in the

resonance frequency compared to the same system but far away from the EP. The highly degenerate nature of the system at hand will allow us to write Jordan chain vectors for the Hamiltonian where orthogonality properties, along with some matrix algebra would be used to show that the eigenvalue splitting is indeed proportional to the N^{th} root of the perturbation. These findings will be confirmed through experimental results, both in two-cavity and three-cavity optical settings.

In Chapter 3, we study a system of coupled cavities that undergo saturation effects. Lasers are by nature nonlinear devices and we theoretically and experimentally discuss these nonlinear effects within the context of PT-symmetry. Linear studies have already been extensively conducted, we thereby construct a saturable model of coupled multiple quantum well (MQW) semiconductor micro-cavities where one experiences saturated gain and the other saturated loss, on top of a linear loss due to absorption and scattering effects.

This analysis would result in a quite unexpected conclusion, serving as an interesting twist to the commonly believed notions based on linear PT symmetric systems. The nonlinear nature of the system would be shown to lead to a reversal of the phase transition – broken-symmetry phase to an un-broken-symmetry phase – upon increasing the saturated gain-loss contrast. We also provide the first large-scale fiber-optic realization of PT-symmetric lasers. We will show that this setting demonstrates phase transitions despite the statistical nature of the optical fields that oscillate inside the (up to a km) long coupled fiber cavities.

Chapter 4 is devoted to the analysis of effects associated with the encirclement of exceptional points in the domain of parameters that define our system. We will differentiate between two scenarios: a static encirclement of an EP, which leads to the accumulation of a geometric phase [30]; and a dynamic encirclement of an EP, that results in a chiral mode conversion process. The former leads to an interchange of the eigenvalues and eigenvectors, while in the later, only one of the eigenvectors dominates at the output [31]. This phenomenon has been studied in some detail in earlier works [32, 33] where an experimental observation was made in the microwave domain in 2001 [34]. However, the later provides much more intriguing conclusions – no matter what state the system is initialized in, the output is dominated only by a single eigenstate. We will formally prove the existence of this mode-preference mechanism and the fact

that only the direction of dynamic encirclement (clockwise or counter-clockwise) determines which of the two eigenstates dominates in a 2D system. At the end of this Chapter, experimental realizations are suggested, including the possibility of creating optical omni-polarizing devices that can convert arbitrary polarization states into a desired output state.

Finally, in Chapter 5, we summarize our results and provide an outlook for future works.

1.1 References

[1] R. Shankar, *Principles of Quantum Mechanics*, 2nd ed. Springer 1994

[2] C. M. Bender and S. Boettcher, *Phys. Rev. Lett.* **80**, 5243 (1998)

[3] C. M. Bender, D. C. Brody, and H. F. Jones, *Phys. Rev. Lett.* **89**, 270401 (2002)

[4] R. El-Ganainy et al., *Opt Lett.* **32**, 2632 (2007).

[5] K. G. Makris et al., *Phys. Rev. Lett.* **100**, 103904 (2008).

[6] A. Mostafazadeh, *Phys. Rev. Lett.* **102**, 220402 (2009).

[7] S. Klaiman, U. Guenther, and N. Moiseyev, *Phys. Rev. Lett*. **101**, 080402 (2008).

[8] S. Longhi, *Phys. Rev.* A **81** (2010).

[9] E. M. Graefe and H. F. Jones, *Phys. Rev.* A **84**, 013818 (2011)

[10] J. Schindler et al., *Phys. Rev.* A **84**, 040101(R) (2011)

[11] J. Schindler et al., *J. Phys. A: Math. Theor*. **45**, 444029 (2012).

[12] M. Chitsazi, et al., *Phys. Rev.* A **89**, 043842 (2014).

[13] R. Fleury, D. Sounas, and A. Alù, *Nature Communications* **6**, 5905 (2015)

[14] X. F. Zhu et al., *Phys. Rev. X* **4**, 031042 (2014).

[15] Z. H. Musslimani et al., *Phys. Rev. Lett*. **100**, 030402 (2008)

[16] S. Longhi, *Phys. Rev. Lett*. **103**, 123601 (2009)

[17] Z. Lin et al., *Phys. Rev. Lett* **106**, 213901 (2011)

[18] A. Guo, et al., *Phys. Rev. Lett*. **103**, 093902 (2009)

[19] C. E. Ruter et al., *Nature Physics* **6**, 192 (2010).

[20] A. Regensburger et al., *Nature* **488**, 167 (2012)

[21] L. Feng et al., *Nature Materials* **12**, 108 (2013)

[22] B. Peng et al., *Science* **346**, 328 (2014)

[23] W. R. Hamilton, *Trans. R. Irish Acad*. 17, 1–144 (1831)

[24] M. V. Berry and M. Wilkinson, *Proc. R. Soc. London, Ser. A* 392, 15–43 (1984).

[25] Wörner et al., *Science* **334** (6053), 208 (2011)

[26] F. Vollmer and S. Arnold, *Nature Methods* **5**, 591 (2008)

[27] Armani et al., *Science* **317** (5839), 783 (2007)

[28] J. Zhu et al., *Nature Photonics* **4**, 46 (2010).

[29] L. He et al., *Nature Nanotechnology* **6**, 428 (2011)

[30] A. A. Mailybaev, O. N. Kirillov, and A. P. Seyranian, *Phys. Rev*. A **72**, 014104 (2005)

[31] M. V. Berry and R. Uzdin, *J. Phys. A: Math. Theor*. **44**, 435303 (2011)

[32] R. Uzdin, A. Mailybaev, and N. Moiseyev, *J. Phys. A: Math. Theor*. **44**, 435302 (2011).

[33] W. D. Heiss, *J. Phys. A: Math. Theor*. **45**, 444016 (2012).

[34] C. Dembowski et al., *Phys. Rev. Lett*. **86**, 787 (2001)

CHAPTER 2. PARITY-TIME SYMMETRIC OPTICAL STRUCTURES

Evolution of a quantum system can generally be described by the Schrödinger equation, which in the normalized form is given as $i\Psi_t = \hat{H}\Psi$, for a time-independent potential, $\hat{H} = \hat{p}^2/2 + V(\hat{x})$. Under the condition of PT symmetry we proceed to derive a well-known relation for the potential involved in the Hamiltonian. The commutation $[\hat{H}, PT] = 0$ implies,

$$\left(\frac{\hat{p}^2}{2} + V(x)\right) PT\, \Psi(x) = PT\left(\frac{\hat{p}^2}{2} + V(x)\right)\Psi(x) \qquad (2.1)$$

$$\left(\frac{\hat{p}^2}{2} + V(x)\right)\Psi^*(-x) = PT\left(\frac{\hat{p}^2}{2}\Psi(x) + V(x)\Psi(x)\right)$$

$$\frac{\hat{p}^2}{2}\Psi^*(-x) + V(x)\Psi^*(-x) = \frac{\hat{p}^2}{2}\Psi^*(-x) + V^*(-x)\Psi^*(-x)$$

$$\Longrightarrow \quad V^*(-x) = V(x) \qquad (2.2)$$

This shows that a necessary (but not sufficient) condition for PT symmetry to hold is that the potential should satisfy $V(x) = V^*(-x)$ [1,2]. In other words, the real part of the complex potential must be an even function of position, while the imaginary part must be odd. The PT operator has the quite useful property that $(PT)^2 = 1$. This means that the eigenvalues of PT are of the form $e^{i\theta}$ [3]; consider an eigenfunction such that $PT\phi_{PT} = \lambda_{PT}\phi_{PT}$ where a second application of the PT operator on the left will give $\phi_{PT} = \lambda_{PT}^*(\lambda_{PT}\phi_{PT}) \Longrightarrow |\lambda_{PT}|^2 = 1$ and hence the eigenvalue should have a unit-complex number form. The commutation between PT and H also means that they share the same set of eigenvectors in the symmetric regime whereas in the broken symmetry regime the eigenvectors of PT and H are no longer all the same [3]. The reality of the spectrum of a PT-symmetric Hamiltonian can be derived considering the following stationary eigenvalue problem where $\psi(x)$ is a common eigenfunction of both H and PT,

$$H\psi(x) = E\psi(x) \qquad (2.3)$$

$$PTH\psi(x) = E^* e^{i\theta}\psi(x)$$

$$HPT\psi(x) = E^* e^{i\theta}\psi(x)$$

$$Ee^{i\theta}\psi(x) = E^* e^{i\theta}\psi(x)$$

$$\Longrightarrow \quad E^* = E \qquad (2.4)$$

The previous discussion has a direct relation to optics in the sense that it provides a fertile ground to investigate *PT*-symmetric Hamiltonians [2,4-6]. The transition from quantum mechanics to optics can be formally justified by considering the isomorphism between the Schrödinger equation and the paraxial wave equation [2,7] which is given as,

$$i\frac{\partial E}{\partial z} + \frac{1}{2n_0k_0}\frac{\partial^2 E}{\partial x^2} + k_0[n_R(x) + in_I(x)]E = 0, \qquad (2.5)$$

where $k_0 = 2\pi/\lambda_0$, n_0 is the substrate index, $n_{R,I}$ are the real/imaginary parts of the index distribution and $n_0 \gg n_{R,I}$. Considering the 1-D Schrödinger equation, $\Psi_t = \left(-\frac{\hbar^2}{2m}\frac{\partial^2}{\partial x^2} + V(x)\right)\Psi$, it is easy to see that the complex refractive index profile plays the role of an optical potential, *i.e.* $V(x) = k_0(n_R(x) + in_I(x))$.

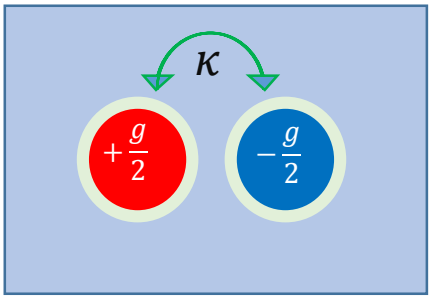

Figure 2.1 Schematic of a PT two-level system

Hence, in optical systems, PT symmetry demands that the spatial distribution of the refractive index is an even function ($n_R(x) = n_R(-x)$), whereas the imaginary component (representing gain or loss) is an odd function of position ($n_I(x) = -n_I(-x)$). One can also show that in high contrast settings, where the electrodynamic problem must be treated fully vectorially, the condition for PT symmetry is expressed

through the complex permittivity, *e.g.* $\varepsilon(\boldsymbol{r}) = \varepsilon^*(-\boldsymbol{r})$ [37]. Nonetheless, since in most systems the imaginary part of the complex refractive index function is considerably smaller than its real counterpart, the PT condition in these two scenarios is almost equivalent.

Dynamics of a PT system and the features associated with exceptional points are easily understood considering the schematic shown in Fig.2.1. It is a coupler of two cylindrically symmetric waveguides where one waveguide experiences gain $(+g/2)$ and its counterpart an equal amount of loss $(-g/2)$. It is assumed that the presence of gain or loss does not alter the real part of the refractive index in the guiding regions so that effectively the system models an even distribution of n_R and an odd distribution of n_I considering the line of reflection between the two waveguides [4,5]. Note that as opposed to space, a time domain approach suitable for cavities can also be used as an example where the exchange of energy between two resonators would occur periodically over time. Considering time dependence of the electric field to be of the type $e^{-i\omega t}$, evolution dynamics for the slow-varying portions of the fields in the waveguides with gain (a) and loss (b) are described by:

$$\begin{aligned} i\frac{d}{dz}a - i\frac{g}{2}a + \kappa b = 0 \\ i\frac{d}{dz}b + i\frac{g}{2}b + \kappa a = 0. \end{aligned} \qquad (2.6)$$

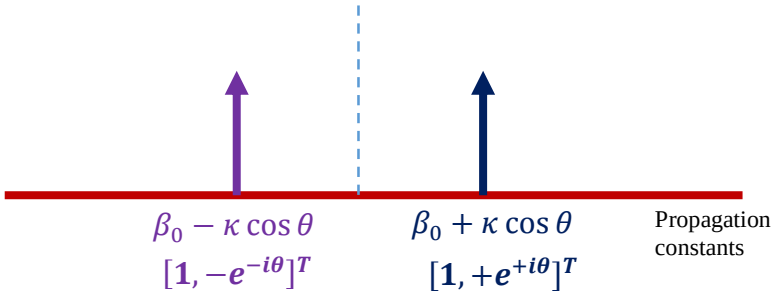

Figure 2.2 Distribution of the eigenvalues and the corresponding supermodes for the formalism of coupling in space.

Here κ is the coupling strength and z is the propagation direction. This system supports two supermodes with distinct characteristics depending on the ratio between gain/loss (g) and coupling (κ). When $g/2\kappa < 1$, the two eigenvalues, which are found by assuming $[a \;\; b]^T = [a_0 \;\; b_0]^T e^{i\lambda z}$, are real and are given by

$\lambda_{1,2} = \pm\kappa\cos(\theta)$ where $\theta = sin^{-1}(g/2\kappa)$ and the corresponding eigenvectors are $|1\rangle = [1 \quad e^{i\theta}]^T$ and $|2\rangle = [1 \quad -e^{-i\theta}]^T$. The two real eigenvalues imply that the two supermodes have propagation constants that lie on either side of the original propagation constant (β_0) of a single waveguide by an amount $\kappa\cos(\theta)$, shown in Fig. 2.2. And it reverts to the well-known result of $\lambda = \pm\kappa$ if there is no gain/loss, i.e. $\theta = 0$. Note that these eigenvectors are not orthogonal in spite of the fact that the spectrum is real. In this case, neither of the two modes experiences a net gain or loss *i.e*. they remain neutral.

On the other hand, the characteristics of the supermodes drastically change as soon as the gain-loss contrast exceeds the coupling strength ($g/2\kappa > 1$). In this regime, the eigenvalues are expressed by $\lambda_{1,2} = \pm\sinh(\theta)$ where $\theta = cosh^{-1}(g/2\kappa)$, and their corresponding non-orthogonal eigenvectors turn out to be $|1\rangle = [1 \quad ie^{-\theta}]^T$ corresponding to $\lambda_1 = +\sinh(\theta)$ and $|2\rangle = [1 \quad ie^{\theta}]^T$ corresponding to $\lambda_2 = -\sinh(\theta)$. Note that the relative intensity in a is greater than in b for $|1\rangle$ and vice versa for $|2\rangle$ indicating that the symmetry of each mode is broken such that one of them resides mostly in the gain waveguide and gets amplified while the other one inhabits the lossy counterpart and decays down with distance. Fig. 2.3 displays the complex eigenvalues as a function of $g/2\kappa$.

The transition point ($g/2\kappa = 1$) between these two different regimes is called the exceptional point, EP. At this crossing, the dimensionality of the vector space is abruptly reduced from 2 to 1. This is evident from the fact that the two eigenvectors become entirely identical $[1 \quad i]^T$ and neither oscillate nor vary exponentially. Instead the modal amplitudes depend algebraically on time ($\sim C_0 + C_1 t$). Since this space was originally two-dimensional, this exceptional point is called an EP-2. This point exhibits a square-root singularity and it is known that the eigenvalues bifurcate as $\varepsilon^{1/2}$ upon a slight perturbation ε [9]. We shall consider this and higher order EPs in the next section and establish their connection with ultra-sensitivity.

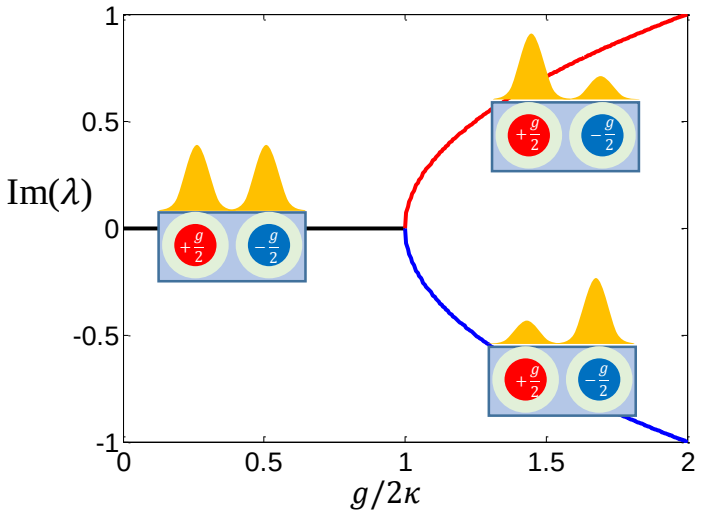

Figure 2.3 The imaginary part of the eigenvalue vs. the gain-loss to coupling ratio for a PT two-level system. After the exceptional point, one of the supermodes experiences amplification, while the other attenuation.

2.1. Enhancing The Sensitivity of Optical Micro-sensors

A second order exceptional point is not exclusive to a PT-symmetric system. It is possible to obtain such a point in a single microcavity, e.g. a microdisk [10,11]. Such a cavity on its own supports both a clockwise and an anticlockwise whispering gallery mode (WGM) [12,13]. It should be noted that most of the optical sensors, especially biosensors for molecular detection [12,14,15], employ such modes for detecting a shift in the resonance wavelength as small as a few fm [16]. WGMs exist in resonant geometries that include microspheres, microtoroids, microdisks and micro-rings. The Q-factors offered by these structures are usually in excess of 10^6 which means that the photon lifetimes are on the order of tens of ns and light gets a chance to circulate several thousands of times in the cavity if input is switched off. This allows very small linewidths $\delta\lambda_r \sim 1$ pm that are a thousand times smaller than those available in fluorescence or absorption

spectroscopy. Fig. 2.4 shows simulation results of a WGM in a micro-ring of outer radius 10 μm, width 500 nm and depth 200 nm

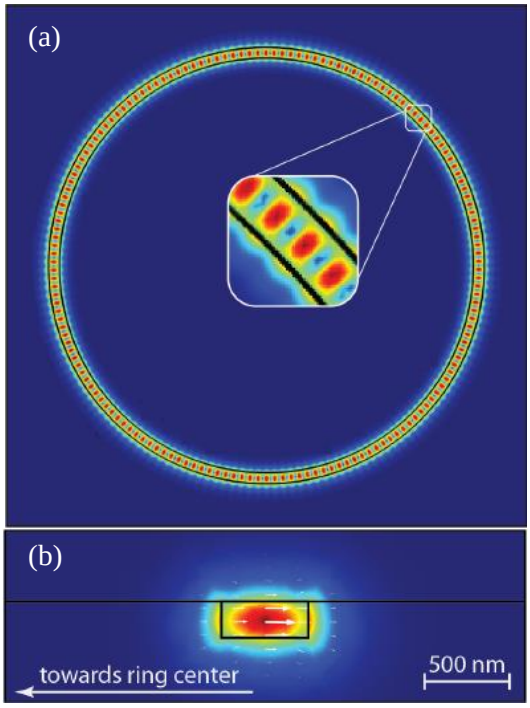

Figure 2.4 (a) A typical whispering gallery mode in a micro-ring resonator (b) The first transverse mode is shown in a cross-section of the ring

The modes (a_R − clockwise, a_L − anticlockwise) in a single micro-disk/ring are effectively described by the following dynamics where Ω is the resonant frequency,

$$i\frac{da_R}{dt} - \Omega a_R = 0 \qquad (2.7)$$

$$i\frac{da_L}{dt} - \Omega a_L = 0 \qquad (2.8)$$

It admits eigenvalues and eigenvectors given by,

$$\lambda_{1,2} = \Omega, \qquad \begin{bmatrix}1\\0\end{bmatrix}, \begin{bmatrix}0\\1\end{bmatrix}. \qquad (2.9)$$

In the presence of a perturbation which could be caused by a scatterer, a coupling is induced between a_R and a_L. Denoting the perturbation by ε, which appears in the off-diagonal terms, the new Hamiltonian for the system and the corresponding eigen-values/vectors are given by,

$$H = \begin{bmatrix} \Omega & \varepsilon \\ \varepsilon & \Omega \end{bmatrix} \tag{2.10}$$

$$\lambda_{1,2} = \Omega \pm \varepsilon, \qquad \begin{bmatrix} 1 \\ 1 \end{bmatrix}, \begin{bmatrix} 1 \\ -1 \end{bmatrix} \tag{2.11}$$

It is obvious that due to the backscattering there arises a splitting in the eigenvalues and that this splitting is proportional to the amount of perturbation. Moreover, lifting of the degeneracy also gave rise to a doublet of standing wave modes (↑↑ and ↑↓). This is the mechanism behind the self-referenced detection schemes reported recently [17]. A schematic of the set-up is shown in Fig. 2.5 [18].

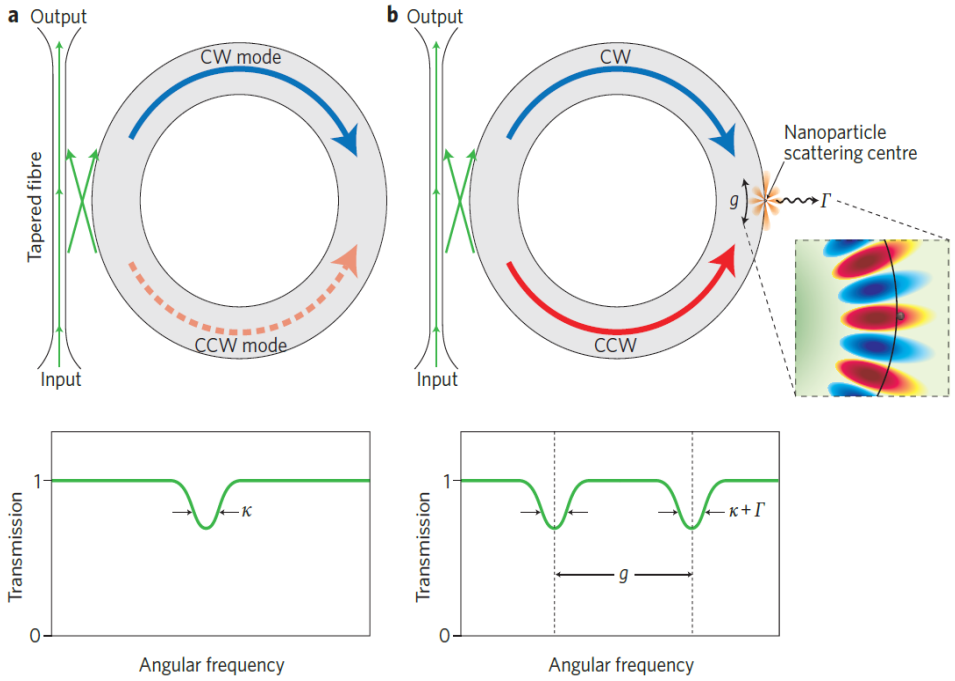

Figure 2.5 (a) Degenerate clockwise and anti-clockwise modes in a single ring resonator (b) Degeneracy is lifted upon a perturbation by a nanoparticle.

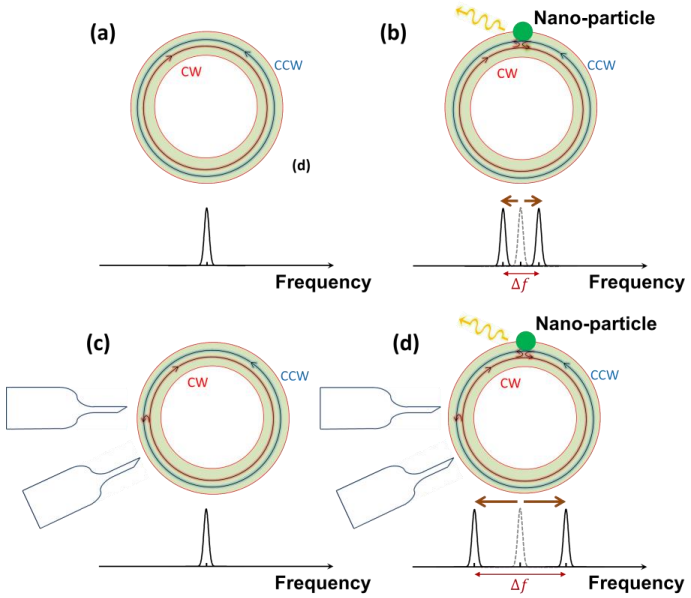

Figure 2.6 A microcavity supports both CW and CCW traveling waves. (a) In the absence of sidewall roughness (scatterings), the frequency of these CW and CCW waves is exactly equal creating a DP. (b) Introducing a target nanoparticle splits the frequency. The splitting is proportional to the perturbation. (c) By judiciously positioning two fiber NSOM-tips it is possible to position the system at an EP. (d) At an EP, the introduction of the target nano-particle results in frequency splitting proportional to the square root of the perturbation.

In 2010 a study reported the controlled manipulation of WGMs in a microcavity with the help of two nano fiber probes [10]. Coalescence of the two resonances was associated with the presence of an exceptional point and later studies [11] analyzed in detail the method of generating an EP-2 in a single microcavity using two scatterers around it, based on the earlier reported experiment. Later on, it was suggested that the presence of an exceptional point in these optical systems can in fact enhance the sensitivity of detection due to the square-root dependence of the frequency-splitting [19]. The system at the exceptional point modeled a completely asymmetric coupling (playing the role of the perturbation – A) between the intrinsic clockwise and anticlockwise modes and the Hamiltonian was shown to be,

$$H_0 = \begin{bmatrix} \Omega & A \\ 0 & \Omega \end{bmatrix}. \qquad (2.12)$$

where splitting of the resonance frequencies is now $\sim \sqrt{A}$. Comparing with the diabolic point – degeneracy between the clockwise and anticlockwise modes in a standalone micro-cavity – there is a quite significant improvement in the amount of splitting. The two possibilities are schematically depicted in Fig. 2.6.

Having established that there is an increase in the amount of splitting at the EP, the next obvious step is to find alternative means of generating such a point. One reason for doing so is the quite cumbersome nature of precisely positioning the two nano-fiber probes in the vicinity of a cavity. Moreover, it is also limited to the attainment of a second-order EP; we will show later on that via the PT-symmetric arrangement higher order EPs can be conveniently obtained.

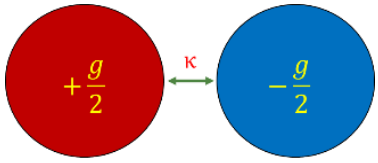

Figure 2.7 Coupled cavities with gain loss contrast g and coupling κ

Based on the earlier discussion of balanced coupled waveguides, consider now two micro-cavities that undergo a coupling in time as opposed to space, see Fig. 2.7, where the dynamics are given by,

$$i\frac{d}{dt}\begin{bmatrix}a\\b\end{bmatrix}+\begin{bmatrix}-\Omega-\frac{ig}{2} & \kappa\\ \kappa & -\Omega+\frac{ig}{2}\end{bmatrix}\begin{bmatrix}a\\b\end{bmatrix}=0, \qquad (2.13)$$

where a, b represent field amplitudes in the gain and loss cavities respectively. Similar to the waveguide case, eigenvalues and eigenvectors coalesce at $\theta = \pi/2$, i.e. $g = 2\kappa$. But the situation under a perturbation ε, say over the cavity with gain, is worth considering. The perturbed Hamiltonian, H and the corresponding eigenvalues $\lambda_{1,2}$ near the EP are as follows,

$$H=\begin{bmatrix}-\Omega-\frac{ig}{2}+\varepsilon & \kappa\\ \kappa & -\Omega+\frac{ig}{2}\end{bmatrix} \qquad (2.14)$$

$$\lambda_{1,2} = \Omega + \frac{\varepsilon}{2} \pm \frac{1}{2}\sqrt{\varepsilon^2 + i2g\varepsilon}. \quad (2.15)$$

Clearly, $|\varepsilon^2| \ll g|\varepsilon|$, which implies,

$$\lambda_{1,2} = \Omega + \frac{\varepsilon}{2} \pm \frac{1}{2}\sqrt{i2g\varepsilon} \quad (2.16)$$

$$\Delta\Omega \propto \sqrt{g\varepsilon} \quad (2.17)$$

This shows that the frequency splitting is again proportional to the square-root of the perturbation. But another interesting aspect is the scaling of this splitting with the amount of gain/loss contrast g. Not only do we get an enhancement due to the nature of the EP, but on top of it there exists the possibility of boosting it even more by using a higher value of g (and also of κ accordingly). The convenience afforded by such an approach is based on a direct control over the value of g through changing the pump level in a cavity and over κ through adjusting the intra-cavity separation or other geometric factors such as the outer curvature of the cavities. We move on towards an extrapolation of these ideas to configurations of multiple photonic cavities that would lead to higher order EPs.

2.2. Experimental Realization of Enhanced Sensitivity Using Coupled Microrings

A convenient method of establishing PT-symmetric configurations is based on coupled cavities where the dimensionality of the system is directly given by the number of interacting modes of these cavities. For instance, in a dual microring arrangement, one can describe the optical dynamics via two coupled differential equations. Similarly, a trimer geometry can be described by a set of three coupled differential

equations. In order to fulfil the requirements of PT-symmetry, one should be able to control not only the optical gain and loss but also the refractive index distribution [20-23]. The former is achieved by carefully tailoring the pumping profile in an InP based semiconductor quantum well structure while the later needs some extra measures. Although fabrication facilities are quite advanced, the fabricated microring structures can still experience errors on the order of 10 nm which can lead to resonance-detuning between adjacent resonators. To alleviate such deleterious effects, we utilize the thermo-optic effect, dynamically tuning the resonance frequencies of the microrings using microheaters (placed underneath) so that the resonances of interest in the adjacent cavities eventually overlap in the spectrum. Such a delicate control over both the gain-loss distribution (imaginary part of the refractive index) and the locations of the resonance frequencies (real part of the refractive index) is essential for establishing higher-order exceptional points [24] for improving the bifurcation response [25-27]. We demonstrate for the first time enhanced sensitivity both in a binary (EP-2) and ternary (EP-3) PT-symmetric microring laser system. The resulting bifurcations in the frequency domain are then monitored and characterized by allowing the system to experience net gain. Perturbations in the form of resonance detuning were introduced using the microhearters.

PT-symmetric coupled geometries of two and three resonators are depicted in Fig.2.8 (a). Figure 2.8 (b) provides a schematic of the ternary PT-symmetric coupled microring system used in our experiments. As previously mentioned, the two side ring resonators are subjected to equal amounts of gain and loss (g) while the ring in the middle is maintained neutral. In addition, the rings are evenly exchanging energy with each other with a coupling strength κ. Three gold heaters are positioned underneath each cavity. An SEM image of the structure, at an intermediate stage of fabrication, is shown in Fig.2.8 (c). In general, the modal field evolution in this structure obeys $id\vec{V}/dt + H\vec{V} = 0$, where $\vec{V} = [a, b, c]^T$ represents the modal column vector (a, b, and c represent field amplitudes in the amplifying, neutral, and lossy cavity, respectively) and H is the associated 3×3 non-Hermitian Hamiltonian, i. e.,

$$H = \begin{bmatrix} -ig + \epsilon & \kappa & 0 \\ \kappa & 0 & \kappa \\ 0 & \kappa & ig \end{bmatrix}. \qquad (2.18)$$

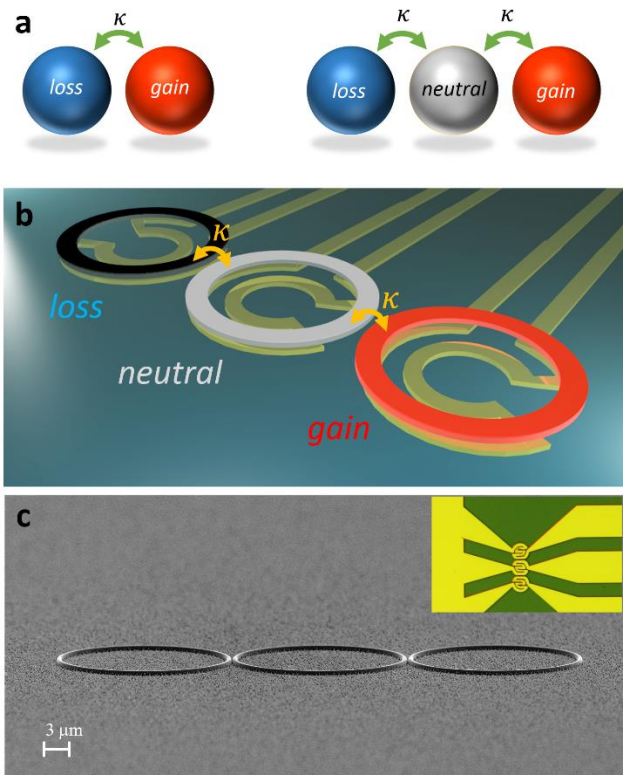

Figure 2.8 (a) Schematics of two possible PT-symmetric photonic molecule arrangements (b) A PT-symmetric ternary microring system, with all cavities equidistantly spaced from each other. The two side ring resonators are experiencing a balanced level of gain and loss while the one in the middle is kept neutral. Three micro-heaters are positioned underneath each cavity for fine-tuning the resonance wavelengths and for subsequently introducing thermal perturbations. (c) An SEM image of the structure at an intermediate fabrication step. The heating elements are shown in the inset.

Here g accounts for the gain/loss levels and κ is the coupling strength between successive resonators. ϵ denotes an external perturbation, that generally could be introduced anywhere along the diagonal elements of the matrix. Without loss of generality, the perturbation has been imposed on the cavity with gain.

In the absence of any disturbance ($\epsilon = 0$), one can directly determine the complex eigenfrequencies ($\omega_n, n = -1,0,1$) of this trimer by solving the following cubic algebraic equation:

$$\omega_n(\omega_n^2 - 2\kappa^2 + g^2) = 0. \qquad (2.19)$$

Equation (2.19) indicates that when the gain/loss contrast attains a critical value, in this case $g = \sqrt{2}\kappa$, all three eigenfrequencies coalesce at $\omega_n = 0$, where the system is operating at a third-order exceptional point. Moreover, at this specific point, the three eigenmodes of this ternary photonic molecule fuse at $[a, b, c]^{EP} = A_0[1, -i\sqrt{2}, -1]$, indicating that the energy in the central (neutral) cavity is twice as much of that circulating in the other two resonators which are subjected to gain and loss.

To understand how a small detuning or gain variation may affect this arrangement, we next assume that ϵ is finite. In this respect, the three complex eigenfrequencies of this PT-symmetric configuration can be obtained by solving the characteristic cubic equation associated with the Hamiltonian matrix (2.18). Of particular interest is how this system reacts around the EP3 singularity, when $g = \sqrt{2}\kappa$. This response is highlighted in the two cross sections (in both the real and imaginary domain) in Figs. 2.9 (a) and (b) as well as in Figs. 2.9 (c) and (d) (solid curves). The differential between two eigenfrequencies (in this case ω_0 and ω_1) is also plotted in Fig. 2.9 (e) (solid curve) as a function of ϵ. By considering the logarithmic behavior

of this latter curve (solid line in Fig. 2.9 (f)), one finds that the slope of the response is 1/3, thus numerically confirming that indeed perturbations around EP3 experience an enhancement of the type $\epsilon^{1/3}$.

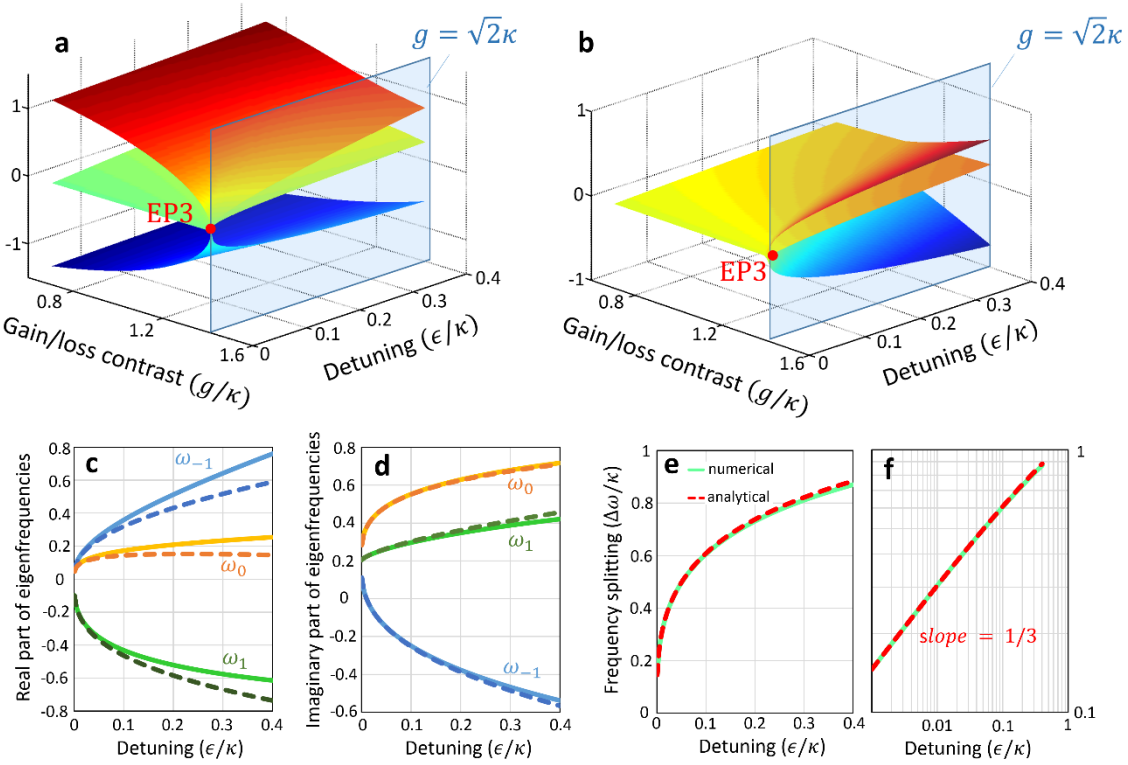

Figure 2.9 (a) The real parts of the three eigen-frequencies of the ternary PT-symmetric system as a function of the gain/loss contrast and detuning. The exceptional point is located at $g = \sqrt{2}\kappa$ and $\epsilon = 0$ (b) Same as in (a) for the imaginary parts of the eigen-frequencies. (c) Analytical results (dashed lines) and numeral solutions (solid lines) for the real parts of the eigen-frequencies as the applied detuning varies when $g = \sqrt{2}\kappa$. (d) Same as in (c) for the imaginary part of the eigen-frequencies. (e) Analytical (dashed red line) and numerical (solid green line) results depicting the difference between ω_{n2} and ω_{n3} in the real domain, illustrating a cubic-root behavior. (f) Same result as in (e) only now shown in a log-log scale. A slope of 1/3 confirms the cubic-root response with respect to detuning.

To analytically explain this intriguing behavior, one can resort to perturbation theory. Around the EP3 point, the characteristic equation now assumes the form:

$$\omega_n^3 - \epsilon\omega_n\left(\omega_n - i\sqrt{2}\kappa\right) + \epsilon\kappa^2 = 0. \qquad (2.20)$$

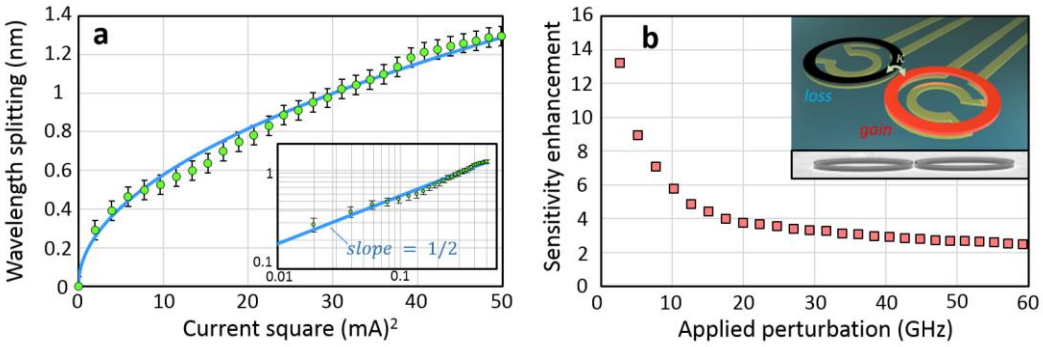

Figure 2.10 (a) Observed square root wavelength splitting of the lasing modes as a function of power dissipated in the heaters ($\propto I^2$) in a binary PT-symmetric system operating around an exceptional point (EP2). In this case, the perturbation is imposed on the active cavity. The corresponding inset demonstrates a slope of 1/2 in a log-log scale, characteristic of an EP2 singularity. (b) Measured enhancement factor as a function of induced perturbation. An order of magnitude enhancement is obtained for a detuning of ~10 GHz between the two resonators. The enhancement is defined in terms of experimentally accessible quantities, as the ratio $\Delta\omega_n^{EP}/\epsilon$, where in this experiment ϵ represents the detuning observed in a single isolated cavity for the same heater power. Inset: a schematic and an SEM image of the microring laser arrangement under study.

The roots of this cubic equation can be perturbatively and self-consistently obtained by assuming that $\omega_n = c_1\epsilon^{1/3} + c_2\epsilon^{2/3} + \cdots$, in stark contrast to what one might expect in Hermitian settings, where the perturbative series proceeds on integer powers of ϵ. From here, one finds that $\omega_n = e^{i(2n+1)\pi/3}\kappa^{2/3}\epsilon^{1/3} - i\sqrt{2}e^{-i(2n+1)\pi/3}\kappa^{1/3}\epsilon^{2/3}/3$. Based on this latter expression, the system response is plotted as dashed curves in Figs. 2.9 (c)-(f), in close agreement to that obtained numerically. Our analysis indicates that the real parts of the pair ω_{-1}, ω_1 as well as those of ω_0, ω_1 diverge from each other in an $\epsilon^{1/3}$ fashion, while the differential between ω_1, ω_2 (that happened to be originally degenerate) varies instead according to $\epsilon^{2/3}$. Hence, in characterizing the sensitivity response of this ternary laser arrangement we will monitor the separation of the ω_0, ω_1 spectral lines. In this case, the anticipated frequency splitting is given by:

$$\Delta\omega^{EP3} = \frac{3}{2}\,\kappa^{2/3}\,\sqrt[3]{\epsilon}. \qquad (2.21)$$

The microring resonators used in this study had a radius of 10 nm, a width of 500 nm, and a height of 210 nm. The cross-section of the rings is appropriately designed so as to ensure single-mode TE conditions at the wavelength of operation $\lambda_0 \sim 1600\ nm$. The system was implemented by utilizing InGaAsP quantum wells, needed to provide the necessary modal gain, estimated to be $\sim 200\ cm^{-1}$. Given that the optical group index in these nano-waveguides is around 4, one finds that $g \sim 10^{12}\ s^{-1}$. Meanwhile, the coupling coefficients κ were designed to reach similar levels by varying the distance between neighboring rings. In all our experiments, the imaginary components of the refractive index in the different regions of the structure are engineered by appropriately shaping the pump beam at 1064 nm. This is done via translation of a knife edge that is imaged onto the surface of the sample. On the other hand, the real part of the index profile is fine-tuned using micro-heaters, as mentioned before. Both these procedures are necessary in bringing the coupled microring lasers at their respective exceptional points, where all the lasing frequencies coalesce into one line. The gain cavity is then perturbed by supplying current into the corresponding heater. By doing so, the change in the refractive index varies linearly with the electrical power dissipated in the resistor ($\epsilon \propto I^2$). As a result, the lasing frequencies begin to diverge and the ensuing splitting – expected to vary in a square-root and cubic root manner for a dimer and trimer configuration, respectively – is then monitored with respect to ϵ. Since we can directly measure the current injected to the heaters, the induced differential detuning was experimentally characterized with respect to the power of the heaters ($\propto I^2$).

We first characterize the bifurcation behavior of an EP2 singularity associated with a PT-symmetric coupled-microring structure (see inset of Fig.2.10). Once a small frequency mismatch ϵ is thermally introduced to this optical oscillator around the EP2, the two lasing frequencies then split according to $\Delta\omega^{EP2} = \sqrt{2\epsilon\kappa}$. The coupling factor in this binary arrangement is $10^{12}\ s^{-1}$. Figure 2.10 (a) clearly demonstrates a square root wavelength splitting with respect to the power dissipated in the heater, in accord with theoretical expectations. A log-log plot with a linear slope of 1/2 reaffirms this behavior (inset in Fig.

2.10 (a)). Figure 2.10 (b) depicts the measured enhancement in sensitivity as a function of the induced perturbation (in terms of shift in resonance frequency). In our study, the enhancement is defined in terms of experimentally accessible quantities, as the ratio $\Delta\omega^{EP2}/\epsilon$. Clearly, because of the presence of an exceptional point, the enhancement factor increases for small values of ϵ. In this case, we observed up to 13 times enhancement in the detuning range below 10 GHz.

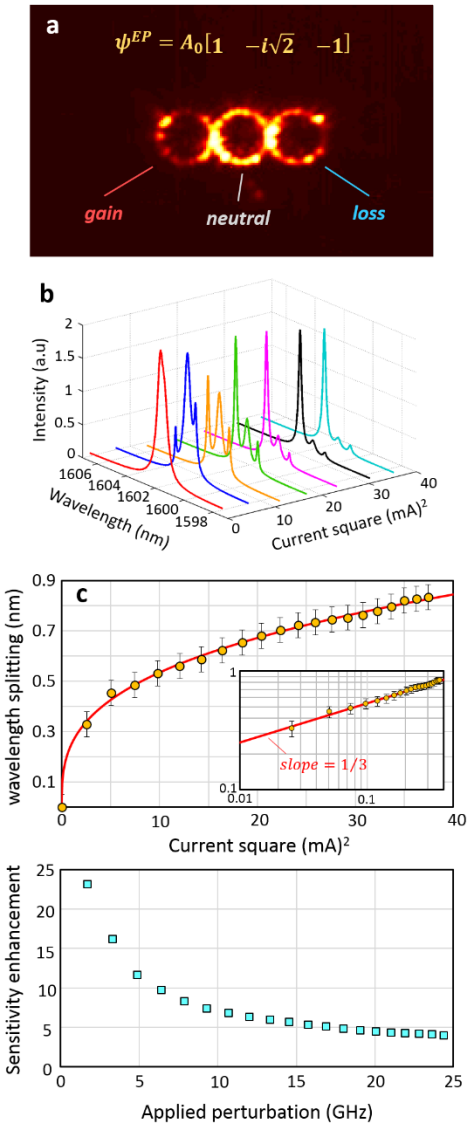

Figure 2.11 (a) Image of the intensity profile of the lasing mode in a PT-symmetric ternary laser arrangement operating around the exceptional point (EP3). The energy in the central (neutral) cavity is approximately twice that in the side resonators. (b) Spectra of the three lasing modes as the system departs

from the exceptional point due to an imposed perturbation on the gain cavity. (c) Resulting cubic-root splitting between two neighboring lasing wavelengths as a function of I^2. Inset: a log-log curve indicates a slope of 1/3. (d) Observed sensitivity enhancement in this arrangement when biased at an EP3 point. An enhancement as large as ~23 is now measured when the detuning is below 10 GHz. The enhancement factor is defined as in Fig. 2.10.

This same approach is employed to investigate the sensitivity of a ternary PT-symmetric system operating close to EP3. The structure is comprised of three microrings equally spaced in a line and having a coupling strength of $\sim 7 \times 10^{11}\, s^{-1}$. To establish PT-symmetry in the system, the pump beam is completely withheld from one of the side rings. In addition, the central ring (neutral region) is partially illuminated while the third ring is fully pumped. By adjusting the position of the knife edge and the pump level, the three lasing modes of this structure gradually coalesce into one line (1602 nm), associated with the emergence of the third order exceptional point. The intensity profile (Fig. 2.11 (a)) of the lasing mode at this point is captured via a CCD camera and is in qualitative agreement with that expected from theory. Once the system is set on an EP3, the heater underneath the pumped cavity is activated. As a consequence of this perturbation, the single lasing mode splits into three distinct branches as anticipated from Fig. 2.9 (c). The spectral evolution of this transition is collected using a spectrometer with an array detector (Fig. 2.11 (b)). As previously indicated, in this experiment we monitor the difference between the resonance frequencies ω_0, ω_1. Figure 2.11 (c) indicates that indeed the frequency separation $\Delta\omega^{EP3}$ follows a cubic root function with respect to ϵ. This is also confirmed after plotting these data in a logarithmic scale from where one can directly infer a slope of 1/3. Finally, the enhancement factor corresponding to this trimer is plotted in Fig.2.11 (d). In this case, the sensitivity is magnified ~ 23 times when the detuning between the active and neutral resonators is below 5 GHz. We would like to mention that around exceptional points, the linewidth of a laser also undergoes an enhancement due to the Petermann factor which can reduce the

sensitivity of the pertutbation measurement. Such a limitation can be decreased by switching to other gain systems or by employing coherence improving geometries [28-29].

2.3. Transverse Optical Mode Filtering

Integrated photonic laser systems with larger cross sections are desirable for many applications since they allow for higher energies within the cavities while managing the thermal load and keeping the impact of optical nonlinearities in check. Unfortunately however, merely enlarging the transverse dimensions of the waveguides inevitably gives rise to competing higher-order spatial modes, given that the refractive index contrast is not altered. This, in turn, compromises the spectral and spatial fidelity of the laser and limits the power that can be extracted from a specific mode [30]. These limitations exist on all scales, and may even be exacerbated in chip-scale semiconductor lasers, where the large gain bandwidths of the active media already pose a challenge in promoting single-mode operation [31]. So far, utilizing intra-cavity dispersive elements has been the primary approach for longitudinal mode selection [32], while tapering along the direction of propagation, engineering the refractive index in the cross section, as well as evanescent filtering are some of the extensively explored techniques to enforce single spatial mode operation in such arrangements [33-36]. Yet, in spite of their success, they are not always compatible with on-chip microcavity structures and in most cases are quite sensitive with respect to fabrication inaccuracies. In this respect, it would be desirable to explore alternative avenues to address these issues.

The selective breaking of parity-time (PT) symmetry has been proposed as a viable strategy for obtaining single longitudinal mode operation [37]. By pairing an active resonator/waveguide with a lossy but otherwise identical partner, it is possible to enforce single- mode performance even in the presence of strong mode competition in multi-moded laser/amplifier configurations. The principle of operation is based on the spontaneous breaking of PT symmetry, which serves as a virtual lasing threshold and encourages single longitudinal mode operation. As in the previous subsection on enhanced sensitivity, PT-symmetry is achieved using a coupled microring system in which the pump power is selectively withheld from one of

the cavities. For a longitudinal mode at wavelength λ, the two eigenvalues of this gain-loss balanced system are given by,

$$\omega_{1,2}(\lambda) = \pm\sqrt{\kappa^2 - g(\lambda)^2}, \qquad (2.22)$$

where the inter-resonator coupling κ for different longitudinal modes is practically the same, but the gain-loss contrast $g(\lambda)$ varies with the wavelength due to the shape of the gain spectrum. If the coupling is now adjusted such that only the mode in the center of the gain spectrum (the fundamental mode) experiences a gain-loss differential exceeding κ, one could obtain complex eigenvalues exclusively for the fundamental longitudinal mode. Specifically, if $g(\lambda_0) > \kappa$, only the mode at λ_0 exists in the PT-symmetry broken phase – enjoying amplification, while all other adjacent longitudinal modes stay in the PT-unbroken phase – remaining neutral [21,22].

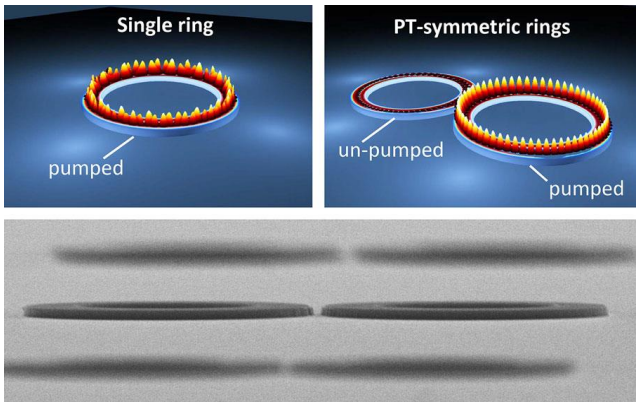

Figure 2.12 Schematic representation of a multimode isolated ring versus a single mode PT symmetric arrangement. (a) In an isolated microring resonator, multiple transverse and longitudinal modes can lase simultaneously. (b) On the other hand, in a PT-symmetric arrangement, only one longitudinal mode with the lowest order transverse profile can lase. (c) Typical SEM image of a PT symmetric double ring structure during an intermediate fabrication step.

We show that PT symmetry can also be utilized in promoting the fundamental *transverse* (or radial) mode in spatially multi-moded micro-ring lasers. As it is well-known, higher order spatial modes systematically exhibit stronger coupling coefficients due to their lower degree of confinement. In mathematical terms it can be stated as $\kappa_0 < \kappa_1 < \kappa_2$ for the first three transverse modes TE_0 TE_1 and TE_2. Consequently, in a PT symmetric arrangement, the fundamental mode is the first in line to break its symmetry as the gain increases (when $g > \kappa$), thus experiencing a net amplification. On the other hand, for this same gain level, the rest of the modes retain an unbroken symmetry and therefore remain entirely neutral. Indeed, following our approach, one can globally enforce single-mode behavior in both the spatial (transverse modes) and spectral domains.

Figures 2.12 (a) and (b) schematically illustrate the transition from multimode behavior in a microring laser to single mode operation in a twin-ring configuration as enabled by preferential PT symmetry breaking. Our experiments were conducted in high-contrast active ring resonators of quaternary Indium-Gallium-Arsenide-Phosphide (InGaAsP) multiple quantum wells embedded in silicon dioxide (SiO_2) and air. An electron micrograph of such rings during an intermediate fabrication step is shown in Fig. 2.12 (c). Based on our measurements, we estimate the quality factor of the fabricated microrings to be on the order of 120,000. The gain bandwidth of the active medium spans the spectral region between 1290 and 1600 nm [38]. Whereas the quantum wells are present in all wave-guiding sections, gain and loss are implemented by selectively pumping the respective rings (pump wavelength: 1064 nm). Accordingly, the effective pump powers are proportional to the geometric overlap between the active medium and the pump profile. In our proof-of-principle design, a ring of an outer radius of 6 μm and waveguide dimensions of 0.21 μm × 1.5 μm was chosen to simultaneously realize a comparably large free spectral range (λFSR=16 nm) and three readily discernible sets of transverse modes (see Fig. 2.13).

Figures 2.13 (a)-(c) depict the transverse intensity profiles of different spatial modes supported by such a single microring resonator. The curvature of the ring imposes a radial potential gradient, which deforms the mode fields into whispering-gallery-like distributions. Whereas the centroid of all modes shifts towards the

ring center, the exponential decay outside the ring still grows strongly with the mode order. Note that the curvature-induced deformation and lateral displacement of the mode profiles slightly reduce the mutual overlap of their respective intensity profiles compared to a straight waveguide. Nevertheless, the competition for gain from the commonly occupied area of the active medium persists. As a result, even in microscopic ring geometries, locally introduced losses in principle cannot be prevented from impacting the desirable mode as well. Indeed, it is this fundamental limitation that the PT-symmetric approach can overcome.

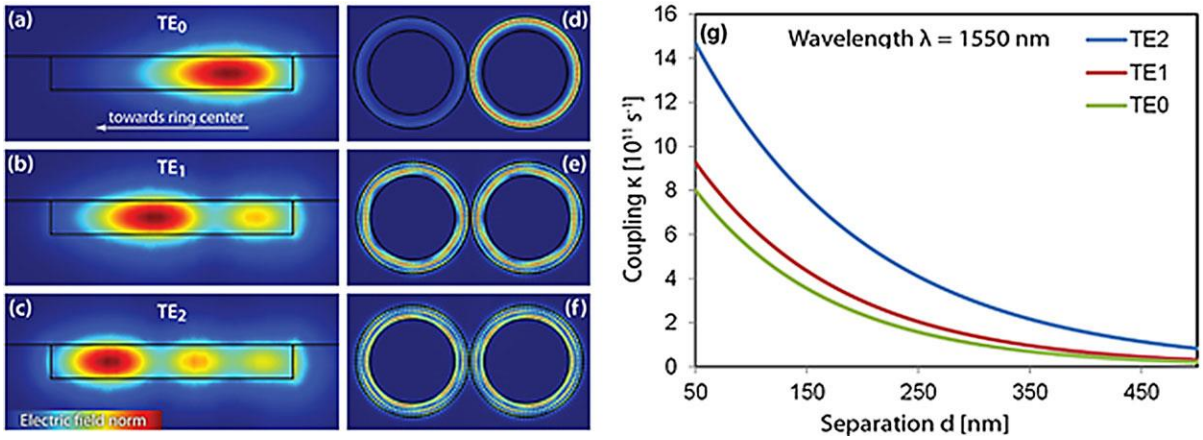

Figure 2.13 Spatial mode profiles and coupling strength for different transverse modes in the structure (a)-(c) Intensity distributions in a microring resonator with a cross section 0.21 μm × 1.5 μm and a radius of $R = 6$ μm as obtained by finite element simulations for the first three transverse modes. (d)-(f) Corresponding intensity distribution of these same modes within the PT symmetric ring resonators. While the TE0 mode operates in the broken PT symmetry regime and lases, all other modes remain in their exact PT phase and therefore exhibit no net gain whatsoever. (g) Exponential decay of the temporal coupling coefficients κ with cavity separation d. Higher order modes exhibit larger coupling coefficients than their lower-order counterparts, providing an additional degree of freedom for tailoring the virtual lasing threshold.

As shown in Figs. 2.13 (d)-(f), an appropriate choice of the coupling coefficient set by the distance between the two rings yields a selective breaking of PT symmetry for the TE0 mode, while all the higher order mode

sets (TE1, TE2) remain in the unbroken PT phase and hence occupy both rings equally. This behavior is mediated by the dependence of the coupling strength on the mode number, which is plotted as a function of the geometric separation between the two rings (see Fig. 2.13 (g)). For a given width of this gap, the coupling coefficient increases with the order of the transverse mode, since the effective indices of higher order modes lie closer to that of the surrounding medium and therefore allow for stronger evanescent interactions across the cladding region. This trend persists for all wavelengths, and in conjunction with the difference in confinement, enables the PT symmetry breaking transition to be employed as a transverse mode-selective virtual loss.

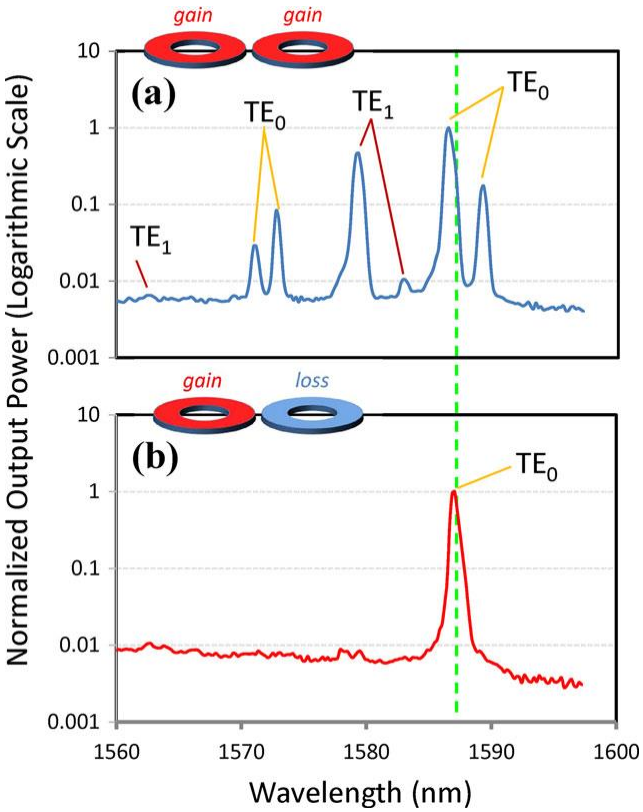

Figure 2.14 PT-mediated single mode operation in the presence of higher order transverse modes. (a) Measured emission spectrum from a coupled arrangement of evenly pumped microrings, comprised of various TE0 and TE1 modes. (b) Global single-mode operation in the PT arrangement. Selective breaking of PT symmetry is used to suppress the entire set of TE1 modes as well as all competing longitudinal resonances from the TE0 set. The minimum separation between the coupled rings is 50 nm. The resolution

of the spectrometer is set at 0.5 nm. More refined measurements using scanning Fabry-Perot techniques reveal a line width of 10 GHz at 1.5 times the threshold.

The emission spectra of the fabricated microring structures were collected using a micro-PL characterization set-up. Utilizing a rotating diffuser, the output of a single mode pump laser is converted to spatially incoherent light with a large and uniform spot size at the sample plane. The knife-edge in the path of the pump beam allows the selective withholding of illumination from specific rings. The location of the shadow in respect to the rings is adjusted by translating the knife-edge and is monitored via the incorporated confocal microscope. The intensity distribution and the spectrum of the light oscillating in the microrings are then observed via scattering centers by means of an infrared camera and a grating spectrometer, respectively. In order to illustrate the selective breaking of PT symmetry, we consider a scenario where a coupled arrangement of identical microring resonators is evenly illuminated by the pump beam. In this case, as shown in Fig. 2.14 (a), every resonance in each ring bifurcates into a doublet because of coupling between the two resonators. In our system, the modes can be distinguished both theoretically and experimentally by considering their wavelength splitting (coupling strength) as well as their corresponding free spectral ranges. For example, the TE1 supermodes exhibit greater frequency splitting compared to the TE0 ones due to their higher coupling coefficient. In the PT-symmetric system, Fig. 2.14 (b), where only one of the two rings is pumped, the TE0 modes preferentially undergo PT symmetry breaking due to a smaller value for the coupling coefficient and fuse into a singlet. In addition, given that different *longitudinal* modes experience different amounts of gain, one can restore the PT symmetry of only one of the TE0 modes by adjusting the pump level. As a result, global single mode operation (spectrally and spatially) can be achieved in this twin-microring system, as only one single longitudinal resonance of the fundamental TE0 mode experiences sufficient gain to induce PT symmetry breaking. Figure 2.14 (b) shows the fusion of a doublet in the frequency domain and the formation of a single lasing mode.

Conventional approaches for the suppression of transverse modes rely on implementing mode-dependent losses, e.g. by means of evanescent coupling to a lossy waveguide [30,39]. Although widely used, these

schemes invariably introduce losses to all modes – including the desirable, fundamental one. Although the PT-inspired design approach presented here likewise exploits the fact that various transverse modes exhibit different degrees of confinement, it differs fundamentally from traditional filtering techniques. The abrupt onset of PT symmetry breaking at the exceptional point relocates the selected mode to the active region, whereas all higher order modes remain equally distributed between loss and gain. Consequently, our approach offers a high degree of mode discrimination, without any detrimental effect on the overall lasing efficiency

2.4. Dark-state Lasers

Microring resonators have emerged as important building blocks of photonic integrated circuits [40,41]. Their small footprint, high quality factor, and modularity make them ideal candidates for on-chip laser systems. Within the domain of these micro-structures, recently, dark state lasers have been proposed as a new class of resonators that make use of the intrinsic properties of non- Hermitian exceptional points to enforce single longitudinal mode operation [42]. Unlike PT-symmetric lasers [21,22] and judiciously balanced gain-loss arrangements [43-45], here the emergence of exceptional points results from the unique geometrical arrangement. In dark state lasers, single-mode lasing is accomplished by selectively endowing one of the supermodes with a substantially higher quality factor. Inspired by the design provided in [42], here we demonstrate lasing in the dark state mode in a coupled microring system. This is implemented by coupling two dissimilar microrings through a common central waveguide channel on an InP-based multi-quantum well semiconductor gain material. In this system, single-frequency emission was enforced with a 30 dB sidemode suppression ratio (SMSR). In addition, by the means of adjusting the ambient temperature, an 8 nm hop-free continuous wavelength tunability was achieved. Figure 2.15 (a) provides a schematic of the configuration used in our experiments. This arrangement is composed of two dissimilar microring resonators (same widths and heights, different radii), indirectly coupled to each other via a central

waveguide. The cross section of the three identical guides is designed so as to favor a single transverse TE mode. Figure 2.15 (b) depicts an SEM image of the fabricated structure.

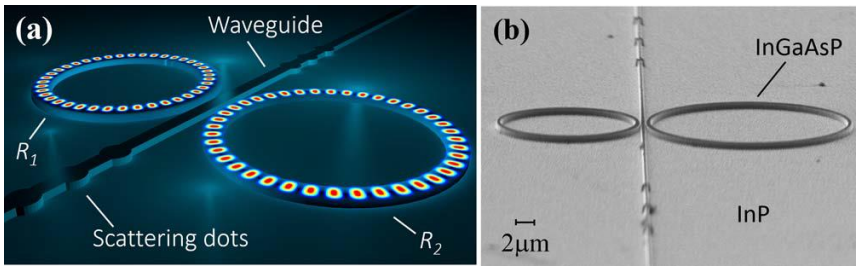

Figure 2.15 (a) Schematic of a dark state laser. Two active microring resonators of different radii are coupled through a central waveguide. The dots on the middle waveguide are used to scatter the light for detection in this channel. (b) SEM image of the dark state laser system at an intermediate fabrication step

The presence of exceptional points and the ensuing mode discrimination in the above dark state arrangement can be explained by investigating the corresponding eigenvalue spectrum provided in Fig. 2.16 and considering Eqs. (2.23)-(2.26). The passive dark state arrangement without any intrinsic gain or loss is considered in this analysis. Here, the eigenfrequencies and eigenmodes of the system can be determined using temporal coupled mode formulations [42,46,47]. By considering the nth longitudinal resonance frequency of the system, the equations representing the evolution of the fields in the two resonators and the bus waveguide can be written as follows:

$$\frac{da}{dt} = -i\omega_1 a - \gamma a - \gamma c + i\mu b_i \qquad (2.23)$$

$$b_0 = b_i + i\mu a + i\mu c \qquad (2.24)$$

$$\frac{dc}{dt} = -i\omega_2 c - \gamma c - \gamma a + i\mu b_i \qquad (2.25)$$

In this model, the ring resonators are viewed as two oscillators with field amplitudes $a(t)$ and $c(t)$, normalized in such a way that $|a(t)|^2$and $|c(t)|^2$ represent stored energies in the rings, b_i and b_0 represent the amplitudes of the input and output waves in the bus channel normalized to the power. $\omega_{1,2}$ are the

resonance frequencies of the rings – deliberately kept different, and μ is the coupling coefficient between each resonator and the bus waveguide. In this analysis, γ represents the out-coupling loss of the two cavities. Note that μ and γ are not independent parameters and conservation of energy demands that $\mu = \sqrt{2\gamma}$. Assuming eigenmode solutions of the form $(a, c) = (a_0, c_0)e^{-i\omega t}$, one can find the longitudinal eigenfrequencies to be

$$\omega_n^{(1,2)} = \left(\frac{\omega_1+\omega_2}{2}\right) - i\gamma \pm \sqrt{\left(\frac{\omega_1-\omega_2}{2}\right)^2 - \gamma^2}\,, \qquad (2.26)$$

The associated eigenmodes can be written as,

$$\begin{pmatrix} a_0 \\ c_0 \end{pmatrix} = \begin{pmatrix} 1 \\ i\delta \pm \sqrt{1-\delta^2} \end{pmatrix}, \qquad (2.27)$$

where $\delta = (\omega_2 - \omega_1)/(2\gamma)$. When the resonance frequencies of the two dissimilar rings are relatively far away from each other $(\omega_1 - \omega_2 \gg \gamma)$, Eq. (2.26) reveals that the eigenfrequencies bifurcate in the real frequency domain. In this scenario, the supermodes are effectively localized in each cavity [notice modal content in the cavities a and c from Eq. (2.27)] and require higher pump levels to reach the lasing threshold, as indicated in Fig. 2.16 (a)-(b). The system is exactly at the exceptional point when the detuning between the two rings satisfies $(\omega_1 - \omega_2 = \pm 2\gamma)$. At this singular point, the two eigenfrequencies and their respective eigenvectors coalesce, as indicated by Eqs. (2.26) and (2.27). Finally, if $(\omega_1 - \omega_2 \ll \gamma)$, the system is operating beyond the phase transition point. In this case, the two coinciding resonances tend to fuse in the real domain, while they split along the imaginary axis. In other words, the two emerging supermodes will resonate at the same frequency, having two very different quality factors $(Q \sim |\omega_R/\omega_I|)$ – see Fig. 2.16 (c). These two supermodes cam be classified into an even and an odd mode. The even mode overlaps with the central channel – experiencing loss – consequently having a low quality factor and is termed as the *bright state* (because the bus waveguide is bright). On the other hand, the odd mode has a negligible overlap with the lossy central channel and hence has a much higher quality factor – making it

the first mode to start lasing and is termed as the *dark state*. Notice that the dark state has a lower loss compared to the uncoupled modes in the individual rings (Fig. 2.16 (a) and (b)) because unlike the dark state, those individual modes are still coupled to the lossy bus waveguide.

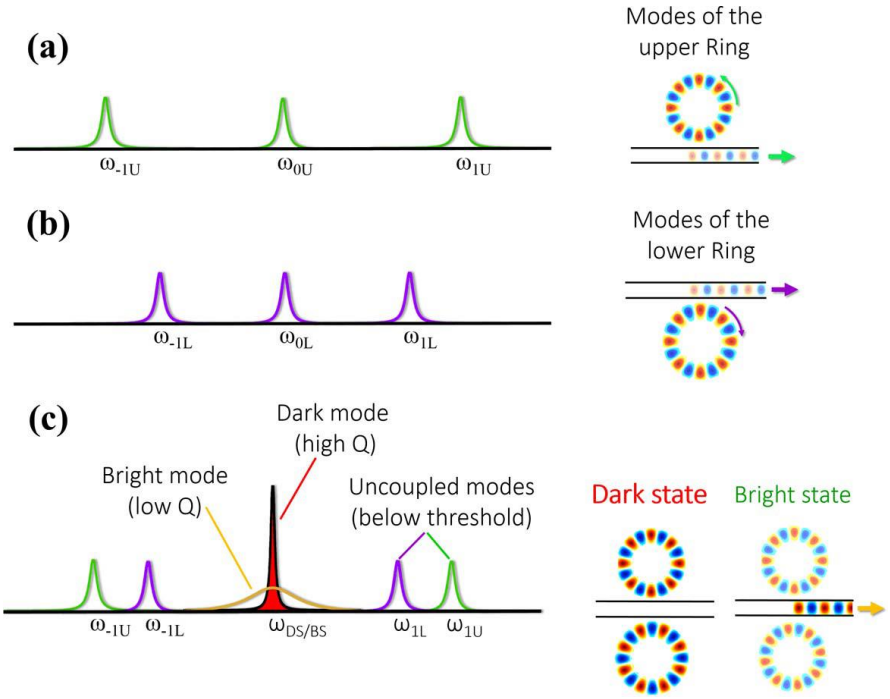

Figure 2.16 Principle of operation of a microring-based dark state laser. (a) Due to out-coupling losses, all the longitudinal modes of the upper microring have a low Q factor and, therefore, a high lasing threshold (dashed line). (b) Similarly, modes of the lower microring cannot reach lasing threshold. (c) In a dark state arrangement, the spectrally coinciding modes of the upper and lower rings form a pair of bright and dark modes. While the bright state loses a significant fraction of its energy to the central waveguide, the dark state has zero overlap with this channel and, therefore, has a high Q-factor and a low lasing threshold. The difference between Q-factors is conveyed in the depicted linewidths of the resulting dark and bright state modes.

We experimentally investigate the formation of dark state modes in a microring system implemented on an InP based semiconductor gain material, as in Fig. 2.15 (b). The central waveguide, as well as the microrings, involve InGaAsP multiple quantum wells and are surrounded by low-index dielectrics (SiO_2 and air). The microrings were optically pumped with a 1064 nm laser beam focused onto a circular area with a diameter

of ~80 μm on the sample surface. A microscope objective is used to project the pump beam on the rings, as well as to collect the output light from the samples. The alignment of the pump beam on the desired cavity was performed by imaging the sample surface through two cascaded 4-f imaging systems onto an IR CCD camera. Output spectra were obtained using a monochromator in conjunction with an LN_2 cooled InGaAs detector. The monochromator resolution was set to 0.4 nm by adjusting the slits. The reported pump power is calculated by taking the ratio of the ring top surface area to the pump laser spot size. Only the output power collected by the objective lens is considered in the reported results.

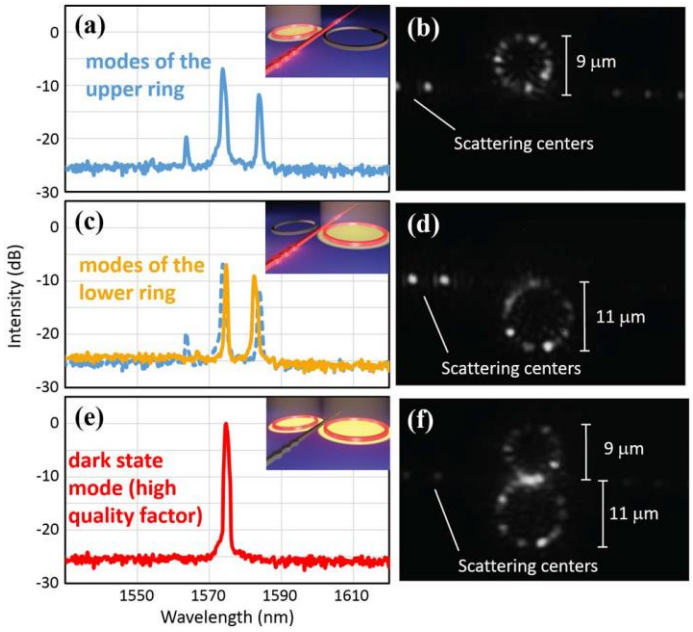

Figure 2.17 Experimental demonstration of dark state formation at room temperature. (a) Emission spectrum of the upper microring when illuminated by the pump beam (peak pump power: 1.2 mW). In this regime, several longitudinal modes are lasing within the gain bandwidth. (b) Corresponding intensity pattern as obtained from scattering imperfections. The presence of light in the central waveguide is observed from the bright scattering centers. (c) and (d) Same as in (a) and (b) when the lower ring is pumped at the same power level; the dotted line in (c) repeats the spectrum of the upper ring for comparison. (e) When both rings are pumped at the same power densities as in (a) and (c), the double-ring system lases in a single dark mode emerged from two coalescing longitudinal frequencies. (f) In this case, a weak emission is seen from the scattering dots, indicating a negligible excitation of the central waveguide, as compared to the first two cases.

Figure 2.17 shows the emission characteristics of a dark state structure composed of two microrings with radii of 9 and 11 μm (width 500 nm; height 210 nm) separated by a waveguide of an identical cross section, centered at a distance of 200 nm from each of the two rings. Single-mode lasing is achieved at room temperature under pulsed pumping conditions (pulse width 15 ns; repetition rate, 290 kHz). To ensure that the observed mode is of the dark state type, the spectrum of this two-ring configuration (Fig. 2.17 (e)) is compared to that obtained from the lower and upper rings when they are pumped individually [Figs. 2.17 (a) and (c)]. As expected, independently, each ring exhibits lasing in a multiple number of modes. However, when a resonance from the upper microring happens to be in close proximity to another one of the lower ring, a dark state mode emerges as the fundamental oscillation in this coupled system [Fig. 2.17 (e) and (f)]. Given that the dark state mode has a larger Q-factor and a lower threshold with respect to the rest of the modes, it can deplete the pool of charge carriers. This prevents the lasing of uncoupled modes in, although the supplied pump intensity is the same as in Figs. 2.17 (a) and 2.17 (c). To observe the light intensity in the middle waveguide, a set of scatterers has been intentionally implanted in the central channel, away from the coupling region shown in Figs. 2.15 (a) and (b). As Figs. 2.17 (b) and (d) show, the scatterers in the middle channel light up when the resonances of the individual rings are excited. On the other hand, these same centers appear dim when both rings are pumped simultaneously, Fig. 2.17 (e)-(f), suggesting that only a dark state mode is present.

Equation (2.27) indicates that under simultaneous pumping conditions and having $\delta \ll 1$, the fields of the two coalesced supermodes are approximately in-phase and π-out-of-phase within these two rings, $(a_0, c_0) = (1, \pm 1)$. Given that the symmetric in-phase mode strongly excites the central waveguide through constructive interference, a considerable amount of energy is expected to be irreversibly lost through this channel. On the other hand, the anti-symmetric π-out-of-phase mode (dark state) does not inject light into the middle channel and, hence, experiences minimum attenuation. In this latter scenario, the mode remains well confined within the two rings, as shown in the inset of Fig. 2.16 (c). Note that this is consistent with the results of Eqs. (2.26) and (2.27). Since any noncoinciding resonance associated with the two dissimilar

rings endures a significant amount of loss through coupling to the central waveguide, in the presence of gain, the anti-symmetric dark state mode is the first in line to lase with a large margin for mode discrimination. By properly choosing the radii of the rings, one can ensure that only one of the dark state resonances coincides with the gain bandwidth of the active system. This then leads to single-mode operation and enables a larger tunability range [42]. In Fig 2.18, we compare the light-light curve (output power versus pump intensity) associated with this configuration when operating in the dark state mode with the case when only one of the rings is pumped. The total output power is measured using a lock-in amplifier and a single-cell cooled InGaAs detector. The lower threshold and higher slope efficiency of the dark state configuration indicate a larger quality factor, in agreement with theoretically anticipated results. Our measurements also show that the dark state laser remains single-mode with SMSR of 30 dB (limited by the dynamic range of the detector) throughout a wide range of pump powers (more than seven times the threshold pump power).

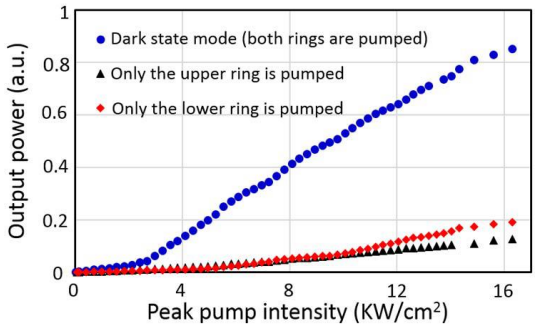

Figure 2.18 Light-light curves associated with dark state mode (when both rings are pumped), and when either the upper or lower rings is pumped. In addition to the remaining single mode for the entire pump power range, the dark state configuration shows lower lasing threshold, higher slope efficiency, and enhanced total output power.

2.5. References

[1] C.M. Bender, D. C. Brody, and H. F. Jones, *Phys. Rev. Lett.* **89**, 270401 (2002).

[2] K.G. Makris et al., *Phys. Rev. Lett.* **100**, 103904 (2008).

[3] C.M. Bender, *Rep. Prog. Phys*. **70**, 947 (2007).

[4] R.El-Ganainy et al., *Opt Lett.* **32**, 2632 (2007).

[5] S.Klaiman, U. Guenther, and N. Moiseyev, *Phys. Rev. Lett*. **101**, 080402 (2008).

[6] T.Kottos, *Nature Physics* **6**, 166 (2010).

[7] C.E. Ruter et al., *Nature Physics* **6**, 192 (2010).

[8] G.Castaldi et al., *Phys. Rev. Lett.* **110**, 173901 (2013).

[9] T.Kato, *Perturbation theory for linear operators*, Springer-Berlin (1996).

[10] J.Zhu et al., *Opt. Express.* **18**, 23535 (2010).

[11] J.Wiersig, *Phys. Rev*. A, **84**, 063828 (2011).

[12] F.Vollmer et al., *Appl. Phys. Lett*. **80** (21) 4057 (2002).

[13] G.Demange and E. M. Graefe, *J. Phys. A: Math. Theor*. **45**, 025303 (2012).

[14] F.Vollmer and S. Arnold, *Nature Methods* **5**, 591 (2008).

[15] A.N. Oraevsky, *Quant. Electron*. **32** (5) 377-400 (2002).

[16] Armani et al., *Science* **317** (5839), 783 (2007).

[17] J.Zhu et al., *Nature Photonics* **4**, 46 (2010).

[18] F.Vollmer et al., *Proc. Natl. Acad. Sci. USA* **105** (52) 20701-20704 (2008).

[19] T.J. Kippenberg, *Nature Photonics* **4**, 9 (2010).

[20] A. Guo, A. et al. Phys. Rev. Lett. 103, 93902 (2009).

[21] H. Hodaei,et. al., Science 346, 975–978 (2014).

[22] L.Feng, et. al., Science 346, 972–975 (2014).

[23] A. Regensburger, et al., Nature 488, 167–171 (2012).

[24] K. Ding,et. al., Phys. Rev. X 6, 21007 (2016).

[25] J. Wiersig, Phys. Rev. Lett. 112, 203901 (2014).

[26] Z.-P. Liu, et al., Phys. Rev. Lett. 117, 110802 (2016).

[27] G. Demange, G. & E. M. Graefe, J. Phys. Math. Theor. 45, 25303 (2012).

[28] C. T. Santis,et. al., Proc. Natl. Acad. Sci. 111, 2879–2884 (2014).

[29] H. Lee, et al. Nat. Photonics 6, 369–373 (2012).

[30] G. P. Agrawal and N. K. Dutta, Semiconductor Lasers (New York, 1993).

[31] L. A. Coldren, Diode Lasers and Photonic Integrated Circuits (Wiley; 2nd ed., 2012).

[32] J. E. Carroll, J. Whiteaway, and D. Plumb, Distributed Feedback Semiconductor Lasers, (1998).

[33] M. Mikulla,et al., IEEE Photon. Technol. Lett. 10, 654 (1998).

[34] J. J. Plant, et al., IEEE Photon. Technol. Lett. 17, 735 (2005).

[35] J. N. Walpole, Opt. Quantum Electron. 28, 623 (1996).

[36] J. N. Walpole, et al., IEEE Photon. Technol. Lett. 14, 756 (2002).

[37] M.-A. Miri, P. LiKamWa, and D. N. Christodoulides, Opt. Lett. 37, 764 (2012).

[38] M. Khajavikhan, et al., Nature 482, 204 (2012).

[39] J. Leidner, and J. Marciante, IEEE J. Quantum Electron. 48, 1269 (2012).

[40] K. J. Vahala, Nature 424, 839 (2003).

[41] V. R. Almeida,et. al., Nature 431, 1081 (2004).

[42] C. M. Gentry and M. A. Popović, Opt. Lett. 39, 4136 (2014).

[43] B. Peng,et. al., Nat. Phys. 10, 394 (2014).

[44] L. Chang, et. al., Nat. Photonics 8, 524 (2014).

[45] B. Peng, et. al., Science 346, 328 (2014).

[46] B. E. Little, et. al., J. Lightwave Technol. 15, 998 (1997).

[47] W. Suh, Z. Wang, and S. Fan, IEEE J. Quantum Electron. 40, 1511 (2004).

CHAPTER 3. SATURABLE PARITY-TIME SYMMETRIC SETTINGS

Over the past few years, there has been a significant research interest in optical systems that simultaneously employ loss and gain in a judicious manner. This area of study came to be known as parity-time (PT) symmetric optics which had its roots in quantum mechanics where a special class of non-Hermitian Hamiltonains was proposed that had completely real eigenvalues. Physically, this implied the existence of constant-amplitude modes despite the presence of inherent amplification and/or attenuation [1-10]. However, if the difference between the amount of gain and loss present in the system exceeds a certain critical value, the spectrum ceases to be real and some modes start experiencing a net amplification – known as the PT-broken phase. One of the most impressive realizations of this phenomenon in optics was that of obtaining single-longitudinal mode lasing from multimode semiconductor laser cavities [11]. It required the selective breaking of PT-symmetry for a single preferred longitudinal mode that lied at the center of the gain spectrum and had the highest gain-loss contrast. On the other hand, all the rest of the possible lasing modes were kept in the PT-symmetric, better known as PT-unbroken, phase – not experiencing any net amplification – hence were prevented from lasing. Even if the laser is divested of unwanted longitudinal modes, there still exists a possibility of lasing in multiple transverse modes. This is especially problematic for broad area structures that inherently allow higher order optical modes to propagate. Earlier, we used a PT symmetric paired configuration of two similar broad cross-sectional-area microrings and obtained mode discrimination by relying on the fact that higher order modes penetrate further out of the periphery of the ring. This implies that in comparison to the preferred fundamental mode, these higher order modes couple more strongly to the lossy counterpart ring resonator and as a result are prevented form lasing. The theoretical results underpinning these effects were all obtained assuming linear dynamics, and studies of nonlinear evolution of optical fields in this regard have been few [12-13]. Since lasers are by nature nonlinear devices, in a separate study we introduced nonlinear gain-saturation into the evolution equations for the optical field and found altogether new results. In particular, a new phase transition behavior was

uncovered for the first time in which the field could transition from the PT-broken phase into the PT-unbroken phase, in opposition to what was previously expected.

In semiconductor structures, both the gain and loss are in fact saturable. This implies that as the field strength in the cavities increases, the effective gain and loss tend to decrease. We theoretically and experimentally studied a pair of coupled microring InGaAsP lasers under different pumping conditions. Under optical excitation, a semiconductor microring provides amplification, while if it is kept in the dark, it acts as an attenuating element. Initially, we equally pumped both the microrings and two lasing lines were observed in the spectrum due to coupling induced mode-splitting. On establishing a PT-symmetric profile by withholding the pump light from one ring, the lasing lines were observed to merge into a single line indicating the onset of a PT-broken phase. According to all previous results in PT-symmetric optics, the lasers should have stayed in this phase even if the gain levels were raised. Our nonlinear theoretical results indicated an altogether different behavior. If this were true, we expected a reverse transition back into the PT-unbroken phase with two lasing lines in the spectrum. And as per expectation, as we increased the pump power in the exposed microring, the single peak bifurcated back to two split lasing peaks. In addition, we introduced parity-time symmetry for the first time in a statistical fiber network. In this realization, we used two optical fibers coupled together through a fiber bragg grating mirror. One fiber included a semiconductor optical amplifier to introduce a controlled amount of gain and a variable optical attenuator was placed in the other fiber for an adjustable loss. This fiber system naturally includes statistical phase variations because of their long lengths. In spite of this, we were able to observe a phase transition from the unbroken to the broken PT regime by simply increasing the amount of loss through the variable optical attenuator. The loss in this system, not the gain, has to be tuned to observe any phase transition. This is because in a laser, the gain always clamps to the value of loss. In addition, we carried out the complete modelling for this configuration where saturation was included in the fiber with gain but the analysis was kept linear in the lossy fiber. The results were impressive in the sense that initially the light output from the gain cavity kept decreasing with loss but after the phase transition, interestingly, the lasing power increased with an increase

in loss. Our results not only further the understanding of lasing phenomena in PT-symmetric optics but also offer opportunities for dynamically modulating the lasing spectrum through adjusting the pump profile. The results obtained also hold true in the case of the much more efficient electrical pumping procedure that could be employed for wide-scale use.

3.1. Nonlinear Dynamics of a Dimer of Semiconductor Laser Cavities

A schematic of a dual micro-ring arrangement is shown in Fig. 3.1. Each micro-ring in our system involves a multiple quantum well InGaAsP-InP structure that is embedded in a silica substrate [11]. The top surface of the rings is exposed to air that serves as a cladding. At 1.55 μm, in this quantum well system, the effective refractive index is $n_e \sim 3$ while the group index in the waveguide rings is $n_g \sim 4$.

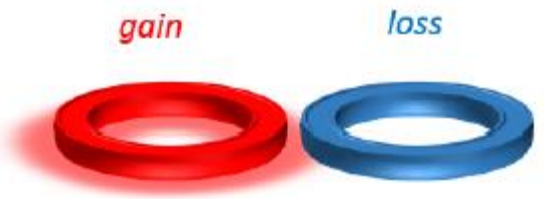

Figure 3.1 A PT-symmetric arrangement of two coupled micro-ring resonators.

For demonstration purposes here we assume that each cavity supports only a single longitudinal and transverse mode [14]. In general, the dynamics in each cavity in isolation are described by a corresponding set of modal field amplitude equations in conjunction with a carrier evolution equation. Yet, once the carriers attain a steady-state, the field equation can be further simplified according to [15]:

$$\frac{dE}{dt} = \frac{1}{2}\left(\frac{\sigma(p-1)}{1+\varepsilon|E|^2} - \gamma_p\right)(1 - i\alpha_H)E. \qquad (3.1)$$

Here $p = \tau_e R_p / N_0$ is a pump parameter, where the carrier generation rate, $R_p = \eta I/(\hbar\omega d)$ and I,η, and d are the pump intensity, the external quantum efficiency and the depth of each micro-ring respectively. In addition, τ_e represents the carrier lifetime, N_0 stands for the transparency carrier population density, ω is

the frequency of the emitted light and $\hbar$ is the Planck' s constant. The parameter ε is inversely proportional to the saturation intensity $\varepsilon = n_e c\epsilon_0 \Gamma a \tau_e/(2\hbar\omega)$ and σ is proportional to the saturated loss in the absence of pumping $\left(\sigma = \Gamma v_g a N_0\right)$. The linear loss γ_p is the inverse of the photon lifetime (τ_p) in the cavity and α_H is the linewidth enhancement factor. Finally, c and ϵ_0 are the speed of light and permittivity in vacuum respectively, Γ is the confinement factor, v_g represents the group velocity and a, the gain constant ($g = a(N - N_0)$). Note that in formulating the evolution equations the material response is assumed to be fast compared to carrier and photon lifetimes and hence is considered here to be instantaneous [15]. In our arrangement we assume that the coupling strength between the two rings is strong and hence any frequency detuning that could result from the α_H factor can be ignored. By adopting this latter assumption and denoting the unsaturated gain as $\tilde{g}_0 = \sigma(p - 1)$, unsaturated loss (at $p = 0$) as $\tilde{f}_0 = \sigma$, we obtain the following two equations describing the dynamics in the aforementioned coupled cavities,

$$\frac{dA_1}{dt} = -\tilde{\gamma}A_1 + \left(\frac{\tilde{g}_0}{1+\varepsilon|A_1|^2}\right)A_1 + i\kappa A_2, \qquad (3.2)$$

$$\frac{dA_2}{dt} = -\tilde{\gamma}A_2 - \left(\frac{\tilde{f}_0}{1+\varepsilon|A_2|^2}\right)A_2 + i\kappa A_1. \qquad (3.3)$$

In Eqs. (3.2)-(3.3), the modal field amplitudes $A_{1,2}$ correspond to the pumped and un-pumped resonators respectively, $\tilde{\gamma}$ is the linear loss present in both cavities and κ is the coupling strength between the resonators. A normalized version of these equations can be easily obtained by adopting the normalized quantities, $a_{1,2} = \sqrt{\varepsilon}A_{1,2}$; $\tau = \kappa t$; $\gamma = \tilde{\gamma}/\kappa$; $f_0 = \tilde{f}_0/\kappa$; and $g_0 = \tilde{g}_0/\kappa$:

$$\dot{a}_1 = -\gamma a_1 + \left(\frac{g_0}{1+|a_1|^2}\right)a_1 + ia_2, \qquad (3.4)$$

$$\dot{a}_2 = -\gamma a_2 - \left(\frac{f_0}{1+|a_2|^2}\right)a_2 + ia_1, \qquad (3.5)$$

where $\dot{a} = da/d\tau$. In what follows we will study the behavior associated with this system of nonlinear evolution equations.

To analyze the response of this arrangement under linear conditions, we assume that the modal field amplitudes are small, i.e.$|a_{1,2}|\sim 0$. Under these assumptions, saturation effects in both the gain and loss mechanisms can be ignored. Hence, this regime can be effectively described by a linearized version of Eqs. (3.4) and (3.5), e.g.,

$$\dot{a}_1 = -\gamma a_1 + g_0 a_1 + i a_2, \qquad (3.6)$$

$$\dot{a}_2 = -\gamma a_2 - f_0 a_2 + i a_1. \qquad (3.7)$$

The eigenvalues of this system, λ, can be directly obtained by adopting the form, $(a_1 \quad a_2) = (a_{01} \quad a_{02})^T e^{-i\lambda\tau}$, where $a_{01,02}$ are complex constants and T represents a transpose operation. In this respect, two regimes can be identified depending on whether$(g_0 + f_0) \lessgtr 2$. In the first case where $(g_0 + f_0) < 2$, the modal solutions of Eqs. (3.6) and (3.7) are given by,

$$\begin{pmatrix} a_1 \\ a_2 \end{pmatrix} = \begin{pmatrix} 1 \\ \pm e^{\pm i\theta} \end{pmatrix} e^{\left(\frac{g_0 - f_0}{2} - \gamma\right)\tau} e^{\pm i(\cos\theta)\tau}, \qquad (3.8)$$

where $\sin\theta = (g_0 + f_0)/2$. We note that the structure of the modal fields closely resembles that expected from an unbroken PT-symmetric coupled arrangement [16]. In particular, the two eigenvectors are by nature non-orthogonal with a phase factor θ that depends on the gain/loss contrast. In addition, a PT-like bifurcation is present around a threshold value given that,

$$\cos\theta = \sqrt{1 - \left(\frac{g_0 + f_0}{2}\right)^2}. \qquad (3.9)$$

If on the other hand $(g_0 + f_0) > 2$, the eigenvectors of Eqs. (3.6) and (3.7) are,

$$\begin{pmatrix} a_1 \\ a_2 \end{pmatrix} = \begin{pmatrix} 1 \\ \pm ie^{\pm\theta} \end{pmatrix} e^{\left(\frac{g_0 - f_0}{2} - \gamma\right)\tau} e^{\mp(\sinh\theta)\tau}, \qquad (3.10)$$

Where $\cosh\theta = (g_0 + f_0)/2$. As opposed to those described by Eq. (3.8), these latter solutions exhibit features of a broken PT-symmetric configuration. In this regime the modal field amplitudes are phase shifted by $\pi/2$ and moreover, they are unequal.

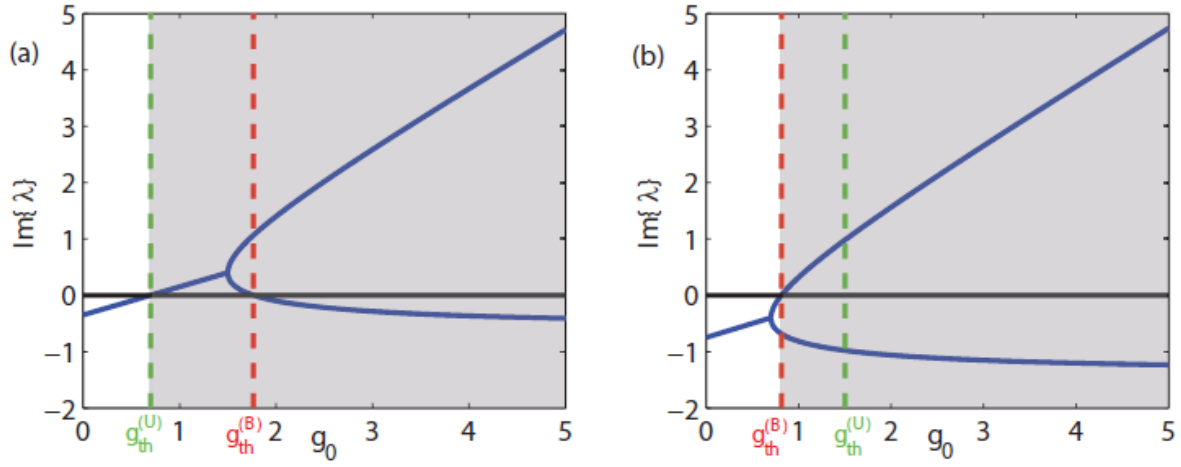

Figure 3.2 Imaginary components of eigenvalues (blue curves) of the linear system are displayed as the gain level increases. In all cases amplification occurs if $Im\{\lambda\} > 0$— represented by the gray regions. The broken PT-symmetric phase appears after a bifurcation takes place. The graph in (a) shows that $Im\{\lambda\} > 0$ before branching occurs, i.e. when $(\gamma + f_0) < 1$, whereas in (b) lasing begins in the broken phase, which takes place when $(\gamma + f_0) > 1$. In both cases the dashed lines indicate the two possible thresholds, where the red line corresponds to the broken phase ($g_{th}^{(B)} = \gamma + 1/(\gamma + f_0)$) and the green to the unbroken ($g_{th}^{(U)} = 2\gamma + f_0$). The system parameters used here are $\gamma = 0.1$ and (a)$f_0 = 0.5$, (b) $f_0 = 1.3$.

If the system is operating in the first regime (unbroken PT-symmetry, given by Eq. (3.8), then the fields will experience linear amplification as long as the gain is above the total loss in the system, i.e.$g_0 > (2\gamma + f_0) = g_{th}^{(U)}$. Conversely, in the broken PT-symmetric phase, described by Eq. (3.10), growth will occur provided that,

$$\left(\frac{g_0-f_0}{2}-\gamma\right)+\sqrt{\left(\frac{g_0+f_0}{2}\right)^2-1}>0. \qquad (3.11)$$

Equation (3.11) implies that in this case, the threshold for lasing is dictated by the following condition,

$$g_0>\gamma+\frac{1}{\gamma+f_0}, \qquad (3.12)$$

i.e. the gain threshold in this broken symmetry is $g_{th}^{(B)}=\gamma+(\gamma+f_0)^{-1}$. In view of the above results, one can conclude that the lasing thresholds corresponding to these two regimes (above/below the PT-symmetry breaking point) are uniquely determined by the parameters, γ, and f_0. To compare these thresholds, one has to consider whether $(\gamma+f_0)>1$ or $(\gamma+f_0)<1$. If for example, $(\gamma+f_0)>1$ then the broken phase – Eq. (3.10), has a lower threshold and therefore will lase ($g_{th}^{(B)}<g_{th}^{(U)}$). Interestingly however, if $(\gamma+f_0)<1$, the situation is reversed and the unbroken PT eigenstate, as given by Eq. (3.8), will experience amplification. The behavior of the system eigenvalues (imaginary part) in these two different domains is depicted in Figs. 3.2 (a) and (b) for various values of the gain, g_0. Figure 3.2 (b) clearly suggests that for $(\gamma+f_0)>1$ i.e. $g_{th}^{(B)}<g_{th}^{(U)}$, the lasing threshold is in fact lower than the total loss in the system $(2\gamma+f_0)$. This counter-intuitive result is attributed to the coupling process which is in this case relatively slow and therefore does not allow the photon energy to see the entire two-ring system. These two lasing thresholds can be summarized by the following inequality,

$$g_0>\min\left[\gamma+\frac{1}{\gamma+f_0},2\gamma+f_0\right]. \qquad (3.13)$$

With these preliminary conditions for g_0, needed for lasing, we can now consider the ensuing nonlinear response of this system.

As the fields in the PT-coupled cavity configuration start to grow, nonlinear saturation effects come into play, as described by Eqs. (3.4) and (3.5). Yet, as we will see, the properties of the linear system (assuming

$|a_{1,2}|^2 \ll 1$) not only determine the lasing thresholds, but also provide valuable information as to how this arrangement will respond in the nonlinear regime. More specifically, if $(\gamma + f_0) > 1$, the system will start from a linear broken PT-symmetry and then enter a broken PT-like nonlinear domain. By further increasing the gain, this same arrangement will transition into a nonlinear unbroken PT phase and will remain there. If on the other hand, $(\gamma + f_0) < 1$, this structure will lase into an unbroken PT-like domain (whether linear or nonlinear) for all values of the gain g_0 above threshold. It is important to emphasize that in the first case, upon increasing the pump level, a reversal in the order in which symmetry breaking occurs is observed, i.e. the solutions transition from a broken to an unbroken state. The two possible nonlinear phases of lasing are described below along with their corresponding gain parameter ranges.

We first describe the regime where lasing takes place in the linear PT-broken regime when $(\gamma + f_0) > 1$. In this scenario, the nonlinear broken-PT supermodes can be directly obtained by assuming stationary solutions for the field amplitudes that have the form, $(a_1 \quad a_2)^T = (a_{01} \quad a_{02})^T$, where $a_{01,02}$ are complex constants. Equations (3.4) and (3.5) are then reduced to,

$$0 = -\gamma a_{01} + \left(\frac{g_0}{1+|a_{01}|^2}\right) a_{01} + i a_{02}, \tag{3.14}$$

$$0 = -\gamma a_{02} - \left(\frac{f_0}{1+|a_{02}|^2}\right) a_{02} + i a_{01}. \tag{3.15}$$

These equations clearly suggest that a_{01} and a_{02} are out of phase by $\pi/2$. This in turn allows one to write $a_{02} = i\rho a_{01}$, where $\rho \in \mathbb{R}^+$ (see Eq. (3.15)) represents the modal ratio. From Eqs. (3.14) and (3.15), we readily obtain the following quartic polynomial equation for ρ,

$$\rho^4 - \left(g_0 + \frac{1}{\gamma} - \gamma\right)\rho^3 + \left(\frac{g_0 - f_0}{\gamma} - 2\right)\rho^2 + \left(-f_0 + \frac{1}{\gamma} - \gamma\right)\rho + 1 = 0. \tag{3.16}$$

In solving Eq. (3.16), we look for a real root in the interval [0,1] since, from a physical perspective, one expects that under steady state conditions, the modal field in the lossy ring will be less than that with gain. In addition, one can show that among all four possible roots, that contained in [0,1] happens to be the only stable one. It is important to note that similar to the broken symmetry modes in linear PT systems, the solution sets in this regime are characterized by an asymmetric distribution of modal fields in the two coupled resonators. For this specific reason, the point $\rho = 1$ is crucial since it marks a PT-restoring transition. The critical gain value (g_c) where this transition occurs is found to be,

$$g_c = f_0\left(\frac{1+\gamma}{1-\gamma}\right). \qquad (3.17)$$

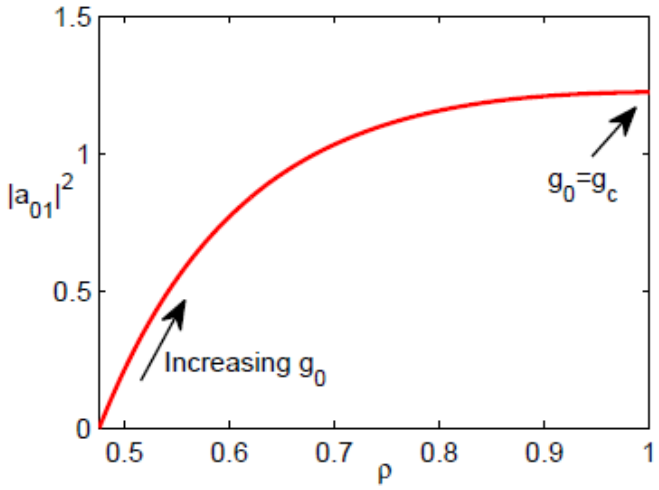

Figure 3.3 Light intensity in the pumped ring as a function of the modal ratio ρ, as obtained from Eqs. (3.14)-(3.16) when $f_0 = 2$ and $\gamma = 0.1$. The linear gain $g_0$is varied between $g_{th}^{(B)} = 0.58$ to $g_c = 2.44$.

Note that this critical gain value is smaller than the lasing threshold needed for the linear unbroken phase, $g_{th}^{(U)}$, that is possible in the parameter range $(\gamma + f_0) < 1$. Hence this nonlinear broken PT phase only arises once lasing begins in the linear broken PT phase which only occurs when $(\gamma + f_0) > 1$, where we also have $g_c > g_{th}^{(B)}$. To demonstrate the energy occupancy in the two cavities, we vary the value of g_0 in the range $g_{th}^{(B)} < g_0 < g_c$. Figure 3.3 depicts these results for $\gamma = 0.1$ and $f_0 = 2$.

As it can be seen in Fig. 3.3, higher values of g_0 not only result in higher steady state intensities in the resonators but also lead to an increased ratio (ρ) that eventually becomes unity. As previously mentioned, an unequal distribution of the fields in the two rings, along with a phase difference of $\pi/2$ clearly indicates that the solution sets in this regime have broken PT-like forms as in Eq. (3.10). Moreover, there is no frequency shift associated with the resonance of the ring system— another indicator of a broken PT-symmetry.

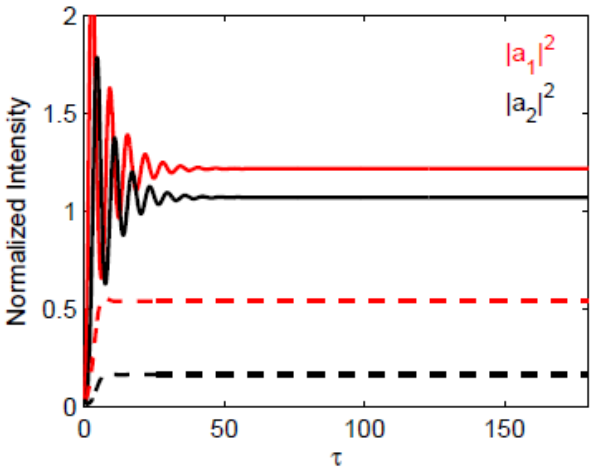

Figure 3.4 The unequal distribution of steady state intensities (broken symmetry) in the rings with gain (red) and loss (black) is shown. The curves are obtained after numerically integrating Eqs. (3.4) and (3.5) for $\gamma = 0.1$ and $f_0 = 2$. Dashed lines represent the solution for $g_0 = 1$ and solid lines are obtained for $g_0 = 2.3$. A higher gain naturally results in higher intensities but at the same time, the intensity contrast between the two resonators decreases.

Remarkably, if one considers linear PT-symmetric dimers, it is well known that the difference between the field intensities in the two components of the dimer becomes larger as we increase the gain-loss contrast beyond the spontaneous symmetry breaking point, indicated by the term $e^{\pm\theta}$ in Eq. (3.10). However, in the nonlinear case, higher pumping levels (larger values of gain) eventually lead the system to the symmetric phase, at $\rho = 1$. Figure 3.4 shows the time evolution of the modal intensities as a function of τ after

solving Eqs. (3.4) and (3.5) for $g_0 = 1$ and$g_0 = 2.3$. This latter figure demonstrates that higher pump levels eventually enforce a transition towards an unbroken phase where the modal ratio is unity. To summarize, the relevant gain range for solutions within this regime is $g_{th}^{(B)} < g_0 < g_c$, provided that $(\gamma + f_0) > 1$.

Before we discuss in detail the properties associated with the nonlienar unbroken PT-symmetry, we note that the results of this subsection are applicable in both regimes, i.e. $(\gamma + f_0) \lessgtr 1$. To obtain the nonlinear eigenmodes in the PT-unbroken phase, we now assume time harmonic solutions, $(a_1 \quad a_2)^T = (a_{01} \quad a_{02})e^{i\lambda\tau}$, where $\lambda \in \mathbb{R}$. In this case, Eqs. (3.4) and (3.5) lead to the following relations:

$$i\lambda a_{01} = -\gamma a_{01} + \left(\frac{g_0}{1+|a_{01}|^2}\right) a_{01} + i a_{02}, \qquad (3.18)$$

$$i\lambda a_{02} = -\gamma a_{02} - \left(\frac{f_0}{1+|a_{02}|^2}\right) a_{02} + i a_{01}. \qquad (3.19)$$

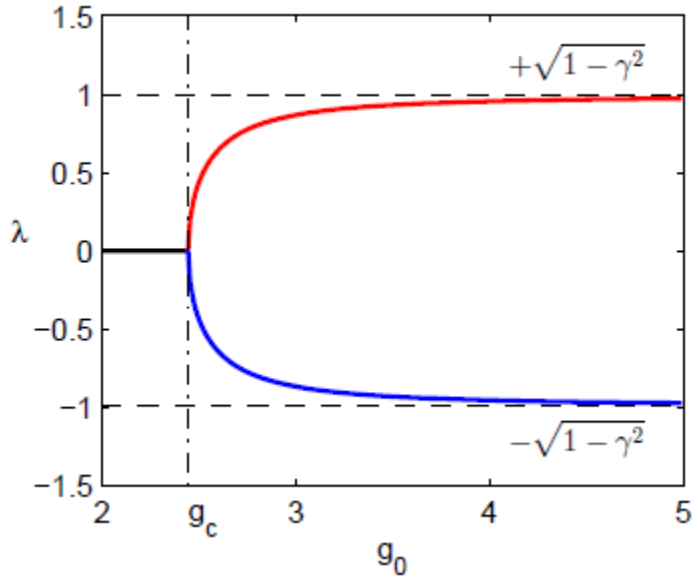

Figure 3.5 The eigenvalues of the nonlinear system exhibit a square-root bifurcation when entering the unbroken symmetry regime. The region $g_0 < g_c$ represents broken symmetry where the eigenvalues are degenerate. The parameter values used here are $\gamma = 0.1$ and $f_0 = 2$. The eigenvalues $\lambda_{1,2}$ approach the asymptotes $\pm\sqrt{1-\gamma^2}$ for large values of g_0.

Using the representation $g_s = g_0/(1 + |a_{01}|^2)$ for the saturated gain and $f_s = f_0/(1 + |a_{02}|^2)$ for the saturated loss and assuming that $a_{01,02} \neq 0$, we get a quadratic equation for the eigenvalues,

$$\lambda^2 - i(2\gamma + f_s - g_s)\lambda - [\gamma^2 + \gamma(f_s - g_s) - g_s f_s + 1] = 0. \quad (3.20)$$

Given that λ is real, it is necessary that,

$$\left(\frac{g_s}{2\gamma}\right) - \left(\frac{f_s}{2\gamma}\right) = 1. \quad (3.21)$$

This last relation is directly satisfied through the parametric representation $g_s = 2\gamma \cosh^2 \eta$ and $f_s = 2\gamma \sinh^2 \eta$, where η is a positive real quantity. In this respect we arrive at the following relations for the intensities,

$$|a_{01}|^2 = \frac{g_0}{2\gamma \cosh^2 \eta} - 1, \quad (3.22)$$

$$|a_{02}|^2 = \frac{f_0}{2\gamma \sinh^2 \eta} - 1. \quad (3.23)$$

The eigenvalue equation Eq. (3.20), now readily reduces to, $\lambda^2 = 1 - \gamma^2 \cosh^2(2\eta)$, in which case, $\lambda_{1,2} = \pm \cos \theta_{\text{nl}}$ provided that $\gamma \cosh(2\eta) = \sin \theta_{\text{nl}}$. Here θ_{nl} represents a nonlinear phase shift ranging between 0 and $\pi/2$. Moreover, after dividing Eq. (3.18) by a_{01} and Eq. (3.19) bya_{02}, upon subtraction we obtain,

$$2i \sin \theta_{\text{nl}} = (\rho - \rho^{-1}) \cos \phi + i(\rho + \rho^{-1}) \sin \phi, \quad (3.24)$$

Where $a_{02} = \rho e^{i\phi} a_{01}$. Equation (3.24) can be solved for the real and imaginary parts, from where one finds that, $\rho = \pm 1$ and $\phi = \pm \theta_{\text{nl}}$, which clearly suggests that $|a_{01}| = |a_{02}|$. This is only possible as long as (by considering Eqs. (3.22) and (3.23)),

$$\tanh \eta = \sqrt{\frac{f_0}{g_0}}, \quad (3.25)$$

i.e. $g_0 > f_0$. The eigenvalue expression in Eq. (3.20) now simplifies to,

$$\lambda^2 = 1 - \gamma^2 \left(\frac{g_0+f_0}{g_0-f_0}\right)^2. \quad (3.26)$$

Equation (3.26) directly indicates that real eigenvalues are only possible if, $g_0 \geq f_0(1+\gamma)/(1-\gamma)$, which is equivalent to $g_0 > g_c$, corroborating the earlier findings. In other words the gain level has to be above this critical value – a necessary condition for observing solution sets in this regime. The unfolding of the nonlinear eigenvalues as a function of the gain level is shown in Fig. 3.5. From these results, one can then determine the unbroken nonlinear PT-symmetric eigenvectors, e.g.,

$$\begin{pmatrix} a_1 \\ a_2 \end{pmatrix} = \sqrt{\frac{g_0-f_0}{2\gamma} - 1} \begin{pmatrix} 1 \\ \pm e^{\pm i\theta_{\mathrm{nl}}} \end{pmatrix} e^{\pm i(\cos\theta_{\mathrm{nl}})\tau}, \quad (3.27)$$

Where $\sin\theta_{\mathrm{nl}} = \gamma(g_0+f_0)/(g_0-f_0)$. When Equations (3.22) and (3.23) are used in conjunction with Eq. (3.25), they provide another restriction on the value of g_0 since $|a_{1,2}|^2 > 0$. More specifically, the restriction is given by $g_0 \geq (2\gamma + f_0) = g_{th}^{(U)}$. Hence, the complete range of g_0 for this solution to exist is:

$$g_0 \geq g_c \cap g_0 \geq g_{th}^{(U)}. \quad (3.28)$$

It should be noted here that under the condition, $(\gamma + f_0) > 1$ i.e. when lasing begins in the broken PT phase, once the gain level exceeds g_c, both conditions in Eq. (3.28) are satisfied and the steady state now assumes the nonlinear unbroken form of Eq. (3.27). This confirms the aforementioned reversal of PT-symmetric phase transition due to the nonlinearity. However, if $(\gamma + f_0) < 1$, where lasing begins in the linear unbroken PT phase, the lasing threshold $g_{th}^{(U)}$ is greater than g_c, which immediately implies that once lasing begins, the system will eventually attain the nonlinear unbroken PT-symmetric steady state solutions, described by Eq. (3.27).

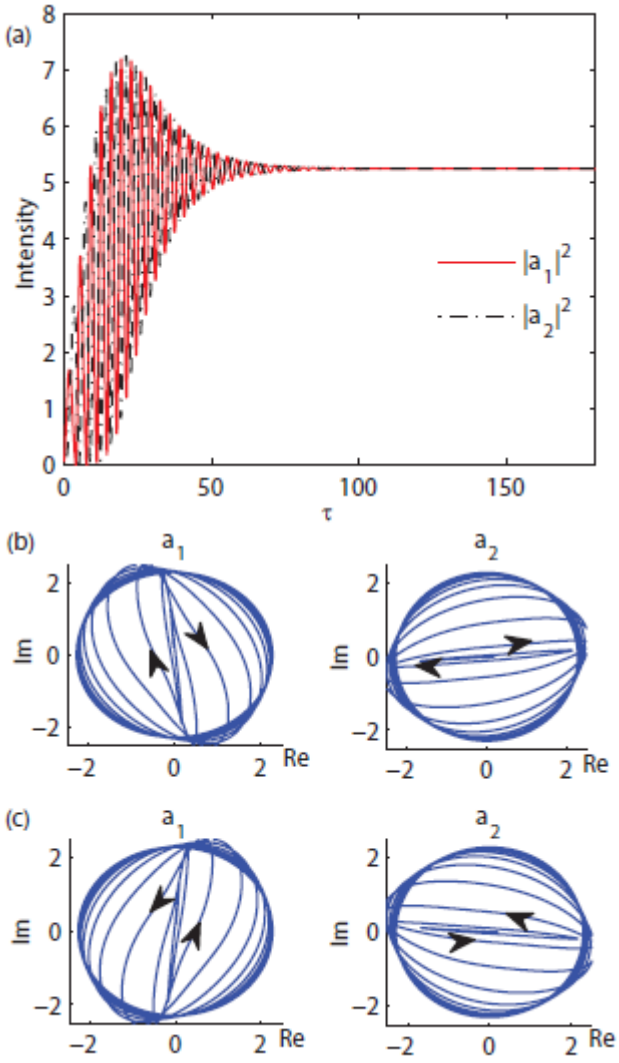

Figure 3.6 Intensity evolution in the two rings is plotted against time τ, when $g_0 = 2.25$, $f_0 = 1$ and $\gamma = 0.1$. Trajectory of the modal fields when (b) $\Delta\phi_0 = \pi/2 + 0.1$ – clockwise rotation and (c) $\Delta\phi_0 = \pi/2 - 0.1$ – counter-clockwise rotation.

The time evolution of intensities in the two coupled resonators can be studied by numerically solving Eqs. (3.4)-(3.5). These results are displayed in Fig. 3.6 (a). Notice that in this domain, the modal amplitudes eventually become equal (irrespective of initial conditions), an indication of nonlinear unbroken PT-symmetry. The analytical expressions in Eq. (3.27) suggest that the system admits two fixed point solutions,

$\lambda_{1,2} = \pm \cos\theta_{\mathrm{nl}}$. The choice between the two depends upon the initial conditions provided. An effective method of deducing which initial conditions correspond to which of the two attractors, is to project the initial vector onto the two nonlinear eigenmodes.

The projection operation has to be carried out in a PT-symmetric sense [17], i.e. respecting bi-orthogonality, which implies that for two vectors $\Phi_1 = \left(\phi_{1x}\ \phi_{1y}\right)^T$ and $\Phi_2 = \left(\phi_{2x}\ \phi_{2y}\right)^T$,

$$\langle \Phi_1 | \Phi_2 \rangle = \begin{pmatrix} \phi_{1y}^* & \phi_{1x}^* \end{pmatrix} \begin{pmatrix} \phi_{2x} \\ \phi_{2y} \end{pmatrix}. \qquad (3.29)$$

By considering the eigenvectors in Eqs. (3.8) or Eq. (3.27), and by letting $v_1 = (1 \quad e^{i\theta})^T$ and $v_2 = (1 \quad -e^{-i\theta})^T$, any initial state $v_0 = (a_{01} \quad a_{02})^T$ can then be projected. Absolute values of the complex coefficients $c_{1,2} = \langle v_0 | v_{1,2} \rangle$ associated with these eigenvectors can then be obtained and are given by,

$$|c_1|^2 = |a_{01}|^2 + |a_{02}|^2 + 2|a_{01}||a_{02}|\cos(\Delta\phi_0 - \theta), \qquad (3.30)$$

$$|c_2|^2 = |a_{01}|^2 + |a_{02}|^2 - 2|a_{01}||a_{02}|\cos(\Delta\phi_0 + \theta), \qquad (3.31)$$

where $\Delta\phi_0 = \phi_{a_{01}} - \phi_{a_{02}}$ is the initial phase difference between the fields a_{01} and a_{02}. As we will see, the eigenvector with the larger initial amplitude will eventually dominate.

The eigenvalue corresponding to the vector v_1 is $\lambda_1 = \cos\theta$ which implies a counter-clockwise rotation in the complex plane. Note that this corresponds to the low frequency supermode since the fast variations in the field, leading to Eq. (1) were assumed to be of the form $e^{-i\omega_0 t}$ where ω_0 is the resonance frequency of

each individual resonator. Similarly, the other eigenvalue, $\lambda_2 = -\cos\theta$ corresponds to its high frequency counterpart.

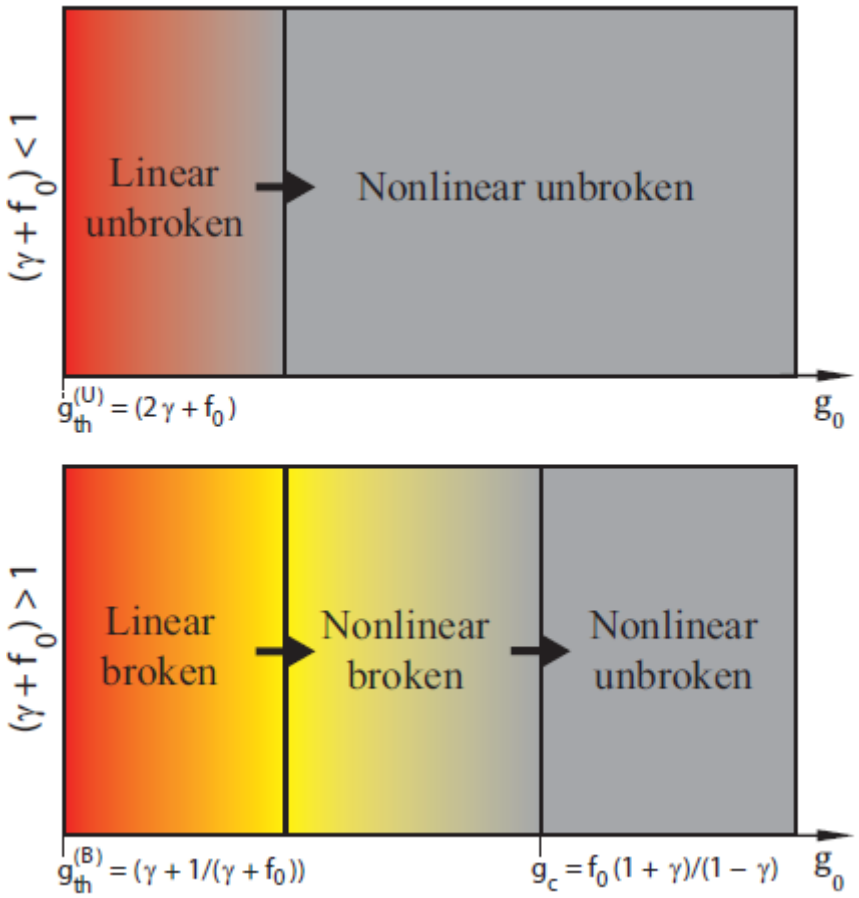

Figure 3.7 System response as a function of gain in two different parameter regimes is schematically shown. In the upper half, where $(\gamma + f_0) < 1$, the system is always in an unbroken PT phase. In the lower half, however, where $(\gamma + f_0) > 1$, the configuration first transitions from a linear broken to a nonlinear broken phase and then eventually enters the nonlinear unbroken domain when g_0 exceedsg_c.

For counter-clockwise rotation, one requires that $|c_1|^2 > |c_2|^2$ and vice versa for clockwise rotation. Since $\cos\theta > 0$ for $\theta = [0, \pi/2\,]$, these conditions can be reduced to, (i) $\Delta\phi_0 \leq \pi/2$, where the low frequency supermode survives and (ii) $\Delta\phi_0 > \pi/2$, favoring its high ferquency counterpart. As an example, let $g_0 = 2.25$, $f_0 = 1$ and $\gamma = 0.1$, that satisfy the conditions in Eq. (23). We now consider two cases for the phase difference in the initial values a_{01} and a_{02}. Figure 6 (b) shows the field evolution when the initla amplitudes

in the two rings are equal, $|a_{01}| = |a_{02}| = 0.2$, but the phase difference is $\Delta\phi_0 = \pi/2 + 0.1$, and (c) shows the same case when $\Delta\phi_0 = \pi/2 - 0.1$. The initla exponential growth is evident and the intensities finally saturate to a common value as given by Eq. (22). We note that in an actual experiment, under PT-unbroken conditions, both eigenmodes will be excited from noise and hence the spectrum will involve two lines at $\pm\kappa \cos\theta_{\text{nl}}$ around ω_0.

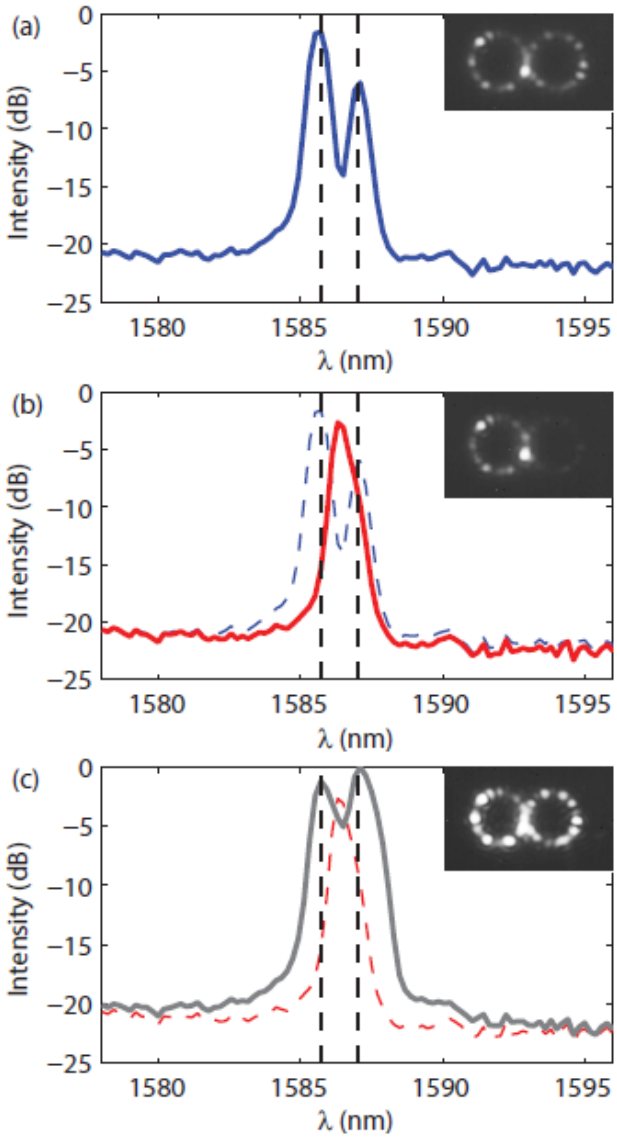

Figure 3.8 Emitted spectrum from (a) uniformly pumped coupled microrings with the pump power of 0.4 mW (b) PT-symmetric structure when 0.4 mW of pump power reaches the active ring (c) PT-symmetric structure when the active ring is subjected to about 10 times the previous power. The insets depict mode

profiles of the different scenarios, recorded by the scattering from the surface of the rings. Dashed vertical lines are used to compare the locations of resonances.

Based on the results presented above, it can be established that in the steady state, the form of the nonlinear solutions is predetermined by the system parameters, specifically by the normalized values of unsaturated absorption (f_0) and linear loss (γ). In the coupled ring resonator arrangement, as the pumping level is increased (as g_0 increases), there are two possible scenarios for the system behavior. If $(\gamma + f_0) < 1$, lasing begins in the linear unbroken PT-symmetric domain (Eq. (3.8)) and then moves into the nonlinear unbroken PT-symmetric regime where the field intensities are equal in both rings albeit with a phase difference, according to Eq. (3.27). If on the other hand $(\gamma + f_0) > 1$, lasing starts in the linear broken

PT-symmetric domain (Eq. (3.10)) and then transitions into the nonlinear broken PT-symmetric phase where the distribution of field strengths in the two coupled resonators is asymmetric and a phase difference of $\pi/2$ exists between them. At even higher gain levels, interestingly, a phase transition occurs from the broken domain into the nonlinear unbroken PT domain when $g_0 > g_c$.

The two scenarios are summarized in Fig. 3.7, where the nonlinear reversal of a PT-symmetric phase transition (broken to unbroken) is displayed in the lower half. It should be noted that the lasing thresholds in these two cases are different and both paths eventually end up in the unbroken PT-like phase as the gain is increased.

To experimentally verify our findings, we used lithographic techniques to fabricate sets of coupled microring resonators comprised of six InGaAsP (Indium-Gallium-Arsenide-Phosphide) quantum wells embedded in InP, capable of providing amplification in the wavelength range $1350 - 1600$ nm. The rings in our experiments have an outer radius of 10 μm, a width of 500 nm, and a height of 210 nm. Such dimensions are deliberately chosen so as the rings support a single transverse mode and to also favor the TE polarization. At first, the two coupled resonators were evenly illuminated using a circular pump beam

with a diameter of 80 μ m. The intensity distribution and spectrum of the modes in the microrings are monitored using a CCD camera and a spectrometer respectively. Figure 3.8 (a) shows the spectrum of the two active rings when are both exposed to a peak pump power of 0.4 mW (15 ns pulses with a repetition rate of 290 kHz).

Under these conditions, coupling-induced mode splitting can clearly be seen. Next, a knife edge is used to selectively withhold the pump power from one of the rings, hence establishing a PT-symmetric gain/loss microring arrangement. Figure 3.8 (b) illustrates the lasing spectrum of this PT system. As expected, lasing occurs exclusively in the active cavity and the frequency of the resonance shifts to the center of the supermode peaks. In other words, the system starts lasing in the broken PT-phase. Next, the pump power illuminating the active ring is increased by a factor of two while keeping again the lossy ring in the dark. The emission spectrum of the PT arrangement subjected to such a high pump power is depicted in Fig. 3.8 (c). In agreement with our theoretical predictions, the PT-symmetry of the combined structure is now restored due to a saturation of nonlinearities. In this regime, both resonators are again contributing equally to lasing and as a result two supermode wavelength peaks are now present in the measured spectrum. Our experimental results confirm the fact that nonlinear processes are indeed capable of reversing the order in which the symmetry breaking occurs.

The discussions in earlier sections are also applicable to the findings in Ref. [11]. In that work, lasing was observed when both microrings were at first equally illuminated (in a way similar to Fig. 3.8 (a)), in which case the system was positioned in the unbroken PT-symmetry phase. This behavior is in agreement with our theoretical results presented, e.g. in Eq. (3.27), provided that one sets $f_0 = -g_0$. In this case, η is purely imaginary and $\theta_{\mathrm{nl}} = 0$, and hence the normalized eigenvalues are $\lambda_{1,2} = \pm 1$, i.e. the mode splitting is twice the coupling between the two cavities—resembling that in standard Hermitian systems. On the other hand, by removing the pump from one of the rings, saturable losses are introduced since now f_0 is positive. In this scenario, Eq. (3.28) is no longer satisfied and as a result the system enters the broken PT phase, in agreement with the observed behavior in Ref. [11].

3.2. Integrable PT-Symmetric Optical Oscillator

In many optical settings, nonlinearity typically manifests itself at high intensities by influencing the real as well as the imaginary part of the refractive index. In general, the imaginary component of the refractive index (gain or loss) is nonlinearly modified through the presence of saturation effects in the effective gain or loss. In addition, the real part of the index also varies with intensity depending on whether the nonlinearity is of the focusing or defocusing type, as dictated by pumping conditions [15]. In semiconductor systems, gain saturation is responsible for clamping the light intensity within a resonator as well as the output power.

Here, we study the case where the light density within a semiconductor structure remains below its saturation limit. This can be achieved by restricting the small-signal gain to relatively low values above the system loss. Moreover, in a travelling waveguide amplifier arrangement, the length of the device provides another degree of freedom in controlling the output optical intensity. Under these considerations, balancing the amount of gain and loss in an evanescently coupled structure composed of two identical elements, renders the system PT-symmetric. In this respect, the optical/electrical pumping level in typical designs based on semiconductor quantum wells allows control over the values of both the gain and loss [11, 18], whereas the spatial separation between the components of a dimer determines the respective coupling strength.

In such a configuration the solution regimes are dictated by the gain (or loss) to coupling ratio which we here represent by $g \in \mathbf{R}^{+}$. By assuming that the linear losses due to scattering and absorption are small in comparison with the coupling strength, the field dynamics in the two components are found to obey the following dimensionless differential equations,

$$\frac{d}{d\tau}u = g(1 - |u|^2)u + iv, \qquad (3.32)$$

$$\frac{d}{d\tau}v = -g(1 - |v|^2)v + iu. \qquad (3.33)$$

In the above equations, u represents the field amplitude in the amplifying element while v that in the lossy counterpart. Both u and v have been normalized with respect to a common gain/loss saturation value. The independent variable τ represents a spatial propagation coordinate (in the case of waveguide geometries) or time (in cavities), and is also scaled with respect to the coupling coefficient, κ. In what follows we determine the critical points of this nonlinear system and through the use of Stokes parameters, identify conservation laws and regimes of oscillatory and stationary responses.

Before we establish the integrability of Eqs. (3.32) and (3.33), it may be beneficial to first study the critical points involved and their associated stability properties. It is important to note that if (u_0, v_0) represents a critical point, then so does $(u_0, v_0)e^{i\phi_0}$, where the phase ϕ_0 is atbitrary. This leads to the conclusion that only the relative phase between the two complex quantities (u_0, v_0) should be considered in the analysis. If we take for convenience u to be real, it then follows from Eq. (3.33) that $v_0 = i\rho u_0$ where $\rho \in \mathbf{R}$. In this case, under steady-state conditions, one finds that,

$$(\rho^2 - 1)(\rho^2 - g\rho + 1) = 0, \tag{3.34}$$

$$u_0^2 = 1 - \frac{\rho}{g}. \tag{3.35}$$

The algebraic roots of Eq.(3.34), signifying the critiocal points, are given by, $\rho = \pm 1, \frac{1}{2}(g \pm \sqrt{g^2 - 4})$. As we will show, among these four possible values of the modal ratio ρ, only one of them happens to be stable. To this end, linear stability analysis is carried out assuming small perturbations, i.e. $(u, v) \rightarrow \left(u_0 + \varepsilon_1(\tau), i\rho u_0 + \varepsilon_2(\tau)\right)$ where in general $\varepsilon_{1,2}$ are complex. Upon substitution in Eqs. (3.32) and (3.33), we obtain the following differential equations concerning these perturbations,

$$\dot{\varepsilon_1} + g u_0^2(\varepsilon_1 + \varepsilon_1^*) - g(1 - u_0^2)\varepsilon_1 - i\varepsilon_2 = 0, \tag{3.36}$$

$$\dot{\varepsilon_2} + g\rho^2 u_0^2(\varepsilon_2^* - \varepsilon_2) + g(1 - \rho^2 u_0^2)\varepsilon_2 - i\varepsilon_1 = 0. \tag{3.37}$$

Given that these relations only feature u_0^2, the sign of u_0 is unimportant for the purposes of stability analysis and henceforth we only consider its positive branch. Breaking down $\varepsilon_{1,2}$ in terms of their real ($\varepsilon_{1R,2R}$) and imaginary ($\varepsilon_{1I,2I}$) parts, one obtains the eigenvalue equation, $MX = \lambda X$ by assuming a temporal dependence of the form $e^{\lambda\tau}$. Here X represents the eigenvector, $X = \left(\varepsilon_{1R_0}, \varepsilon_{1I_0}, \varepsilon_{2R_0}, \varepsilon_{2I_0}\right)^T$ of the matrix M,

$$M = \begin{pmatrix} 3\rho - 2g & 0 & 0 & -1 \\ 0 & \rho & 1 & 0 \\ 0 & -1 & -1/\rho & 0 \\ 1 & 0 & 0 & -(3/\rho - 2g\,) \end{pmatrix} \qquad (3.38)$$

The characteristic equation for this system is given by the following expression,

$$\lambda\left\{\lambda - \left(\rho - \tfrac{1}{\rho}\right)\right\}\left\{\lambda^2 - 3\left(\rho - \tfrac{1}{\rho}\right)\lambda + 1 - (2g - 3\rho)\left(2g - \tfrac{3}{\rho}\right)\right\} = 0. \qquad (3.39)$$

We next separately analyze the stability properties of the four stationary points ρ. In this case we find:

(i) $\rho = -1$

$$\lambda_{1,2} = 0$$

$$\lambda_{3,4} = \pm 2\sqrt{(g+1)(g+2)}$$

Since $g > 0$, there always exists a positive real λ which renders this point unstable.

(ii) $\rho = +1$

$$\lambda_{1,2} = 0$$

$$\lambda_{3,4} = \pm 2\sqrt{(g-1)(g-2)}$$

For $g < 1$ or $g > 2$, it is clear that one eigenvalue is a positive real number so that this point becomes unstable. Moreover, the double eigenvalue ($\lambda_{1,2} = 0$) is not semi-simple [19] (also

true for $1 < g < 2$) and leads to terms proportional to τ in the general solution, thus introducing instability.

(iii) $\rho = \frac{1}{2}(g + \sqrt{g^2 - 4})$

$$\lambda_1 = 0$$

$$\lambda_2 = \sqrt{g^2 - 4}$$

$$\lambda_{3,4} = \frac{\sqrt{g^2 - 4}}{2}(3 \pm 1)$$

If $g > 2$, then all eigenvalues are positive and hence this stationary point is unstable. On the other hand, for $g < 2$, ρ is complex, hence violating Eq. (3.35) for u_0^2.

(iv) $\rho = \frac{1}{2}(g - \sqrt{g^2 - 4})$

$$\lambda_1 = 0$$

$$\lambda_2 = -\sqrt{g^2 - 4}$$

$$\lambda_{3,4} = -\frac{\sqrt{g^2 - 4}}{2}(3 \pm 1)$$

Stability is here ensured for $g > 2$ since all the eigenvalues are negative ($\lambda \leq 0$). On the other hand if $g < 2$, this point does not exist for the same reason mentioned in the previous case. Note that the critical point corresponding to the value of $g = 2$ makes the cases (ii)-(iv) equivalent and is found to be stable.

A bifurcation diagram describing the behavior of the critical points as a function of the gain/loss g constant is shown in Fig. 3.9 (a), where the stable branch of ρ is depicted as a solid line. As the value of gain increases beyond $g = 2$, the ratio between the fields starts decreasing, starting from $\rho = 1$ and asymptotically reaching $\rho = 0$. This behavior is reminsscent of linear PT-symmetric systems where in the broken symmetry domain (after a bifurcation in the eigenvalues beyond an exceptional point) the field strengths in the gain and loss components become unequal [16]. This is shown in Fig. 3.9 (b) for $g > 2$. However, in contrast with a linear PT-symmetric dimer where an exponential increase in intensities is expected with time, the saturation in Eqs.(3.32) and (3.33) will enforce a bounded steady-state for $g > 2$. Furthermore, once this PT-symmetry is broken, light tends to predominantly reside in the cavity that offers amplification, as the gain-loss contrast is increased.

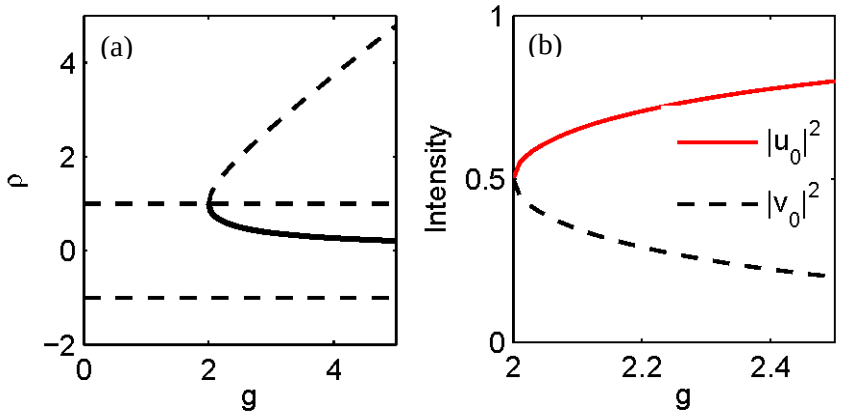

Figure 3.9 The various branches of the ratio ρ associated with the critical points as a function of g are displayed in (a) where the solid line indicates stable behavior while the dashed unstable. (b) Intensities in the two optical elements corresponding to the stable critical point are plotted as the value of g increases.

Moreover, the stability of the trivial critical point at the origin ($u_0 = v_0 = 0$) needs also to be considered. Here, the differential equations for the perturbations assume the following form,

$$\dot{\varepsilon_1} - g\varepsilon_1 - i\varepsilon_2 = 0, \qquad (3.40)$$

$$\dot{\varepsilon_2} + g\varepsilon_2 - i\varepsilon_1 = 0. \qquad (3.41)$$

Again, using the representation, $(\varepsilon_1, \varepsilon_2) = (\varepsilon_{01}, \varepsilon_{02})e^{\lambda\tau}$, the eigenvalues of this system are found to be $\lambda_{1,2} = \pm\sqrt{g^2 - 1}$. In the range $g < 1$, these values are purely imaginary and conjugate to each other, thus implying an unstable saddle point. On the other hand, for $g > 1$, there exists a positive real λ indicating linear exponential growth.

However, it is instructive to notice that, when the fields in both cavitites start from noise where $|u_0|, |v_0| \sim 0$, the dynamics reduce to that of a linear PT-symmetric coupler, governed by Eqs. (3.40) and (3.41), with ε_1 and ε_2 being replaced with u and v respectively. In this linear scenario, it is well known that the PT-symmetric phase transition occurs at the point where the gain/loss contrast to coupling ratio is unity. The role of this spontaneous symmetry breaking point at $g = 1$ is apparent in Fig. 3.10, where the initial values were choosen to be small, $|u(0)|, |v(0)| = 10^{-2}$. Below this breaking point, the intensities evolve sinusoidally – characteristic of unbroken symmetry eigenmodes [20]; For $g > 1$, the linear symmetry breaks and an initial exponential growth occurs up to the point where the intensites get larger and saturation starts to limit this growth.

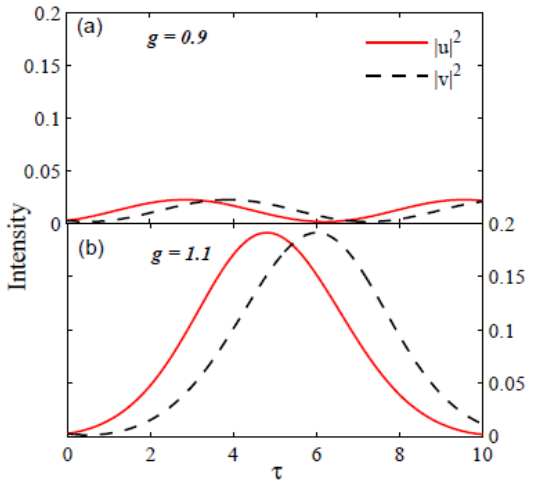

Figure 3.10 The effect of the linear PT symmetry breaking, around $g = 1$, is depicted. (a) For $g = 0.9$ sinusoidal oscillations occur while (b) for $g = 1.1$ an exponential growth takes place until saturation comes into play.

In this section we analyze the properties and behavior of this non-Hermitian nonlinear dynamical system (Eqs. (3.32) and (3.33)) using Stokes parameters. To do so, we first obtain the conservation laws that are needed to establish integrability. The Stokes parameters are defined as follows,

$$S_0 = |u|^2 + |v|^2, \tag{3.42}$$

$$S_1 = |u|^2 - |v|^2, \tag{3.43}$$

$$S_2 = u^* v + u v^*, \tag{3.44}$$

$$S_3 = i(u^* v - u v^*). \tag{3.45}$$

These four real quatnities listed here are interrelated by the expression,

$$S_0^2 = S_1^2 + S_2^2 + S_3^2. \tag{3.46}$$

The dynamical equations for each of these four parameters can be directly obtained using Eq.(3.32)-(3.33), i.e.

$$\dot{S_0} = -2gS_0S_1 + 2gS_1, \tag{3.47}$$

$$\dot{S_1} = -g(S_0^2 + S_1^2) + 2gS_0 + 2S_3, \tag{3.48}$$

$$\dot{S_2} = -gS_1S_2, \tag{3.49}$$

$$\dot{S_3} = -(2 + gS_3)S_1. \tag{3.50}$$

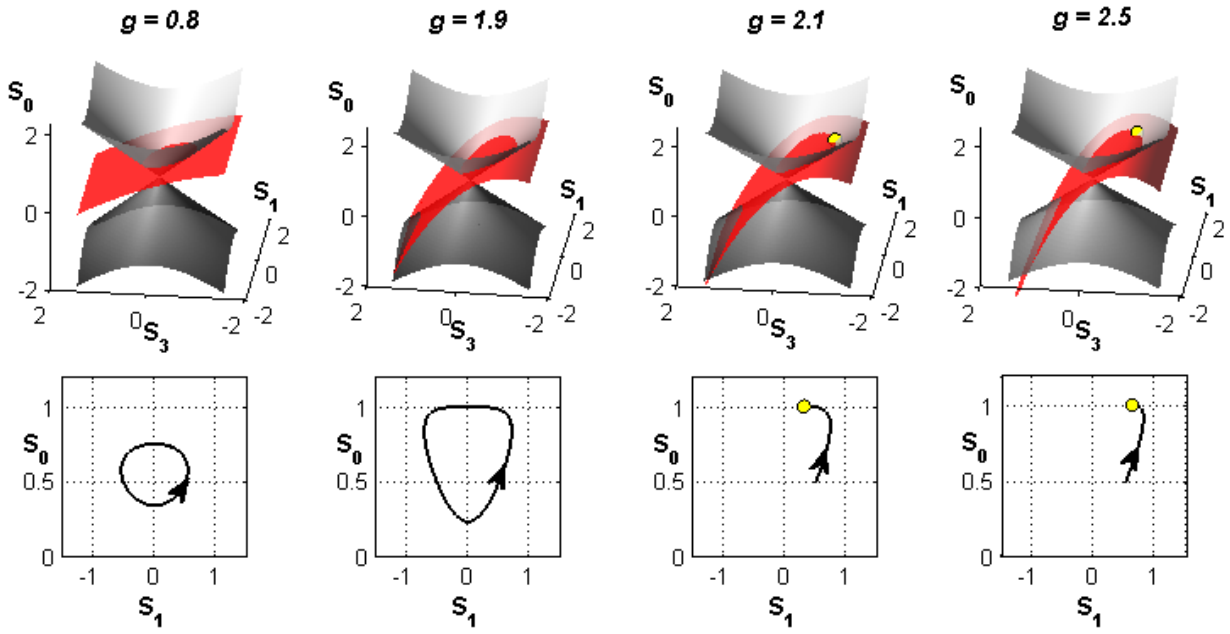

Figure 3.11 Intersections between two surfaces in the $(S_1, S_3 S_0)$-space are plotted that describe the solution trajectories. These are shown for two values of g both below, (a) and (b), and above, (c) and (d), the nonlinear phase transition point $g = 2$. Corresponding plots in the lower panel depict the intersections in the (S_1, S_0) plane. The stable critical point appears for $g > 2$ and is shown as a yellow dot. In all cases, the initial values of the fields are $u_0 = 0.7(1 + 0.1i)$ and $v_0 = 0$.

From Eqs. (3.47), (3.49) and (3.50), one can establish that, $S_1 = -\frac{\dot{S}_2}{gS_2} = -\frac{\dot{S}_3}{(2+gS_3)} = -\frac{\dot{S}_0}{2gS_0 - 2g}$, which immediately leads to the following two conservation laws,

$$A = \frac{S_2}{(2+gS_3)}, \qquad (3.51)$$

$$B = \frac{S_2^2}{(S_0 - 1)}. \qquad (3.52)$$

Clearly, the existence of these two constants of motion implies integrability. These two constants are determined by the initial values of the Stokes parameters and the gain-loss contrast. To find the evolution trajectory of $u(\tau)$ and $v(\tau)$, it suffices to know the dynamics of only one Stokes parameter. In this case, by

first expressing S_3 and S_0 in terms of S_2 [using Eq. (3.51) and Eq. (3.52)] in Eq. (3.46) and finally using Eq. (3.49) that relates S_1 to S_2 and $\dot{S_2}$, we obtain a differential equation solely involving S_2,

$$\left(\dot{S_2}\right)^2 = g^2 S_2^2 \left\{\left(1+\frac{S_2^2}{B}\right)^2 - S_2^2 - \frac{1}{g^2}\left(\frac{S_2}{A}-2\right)^2\right\}. \qquad (3.53)$$

In principle, Eq.(3.53) can be solved by quadrature. Hence from $S_2(\tau)$, $S_3(\tau)$ and $S_0(\tau)$ can then be recovered from the conservation laws and finally $S_1(\tau)$ can be found using Eq. (3.49) or Eq.(3.46). This enables the dynamics of all four Stokes parameters to be determined. From here one can obtain the original field amplitudes and phases via Eqs. (3.42)-(3.45), e.g. $|u(\tau)|^2 = (S_0(\tau) + S_1(\tau))/2$ etc.

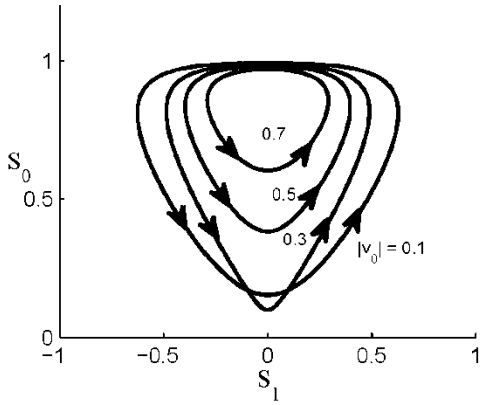

Figure 3.12 Different solution trajectories in the (S_1, S_0)-space are found as the initial conditions are changed. For these plots, u_0 is fixed at $u_0 = 0.7$, while v_0 is varied in the imaginary space from $v_0 = 0.1i$ to $v_0 = 0.7i$. The gain/loss value used here is $g = 1.8$. Arrows indicate the evolution over time.

The trajectories followed by the solutions can be conveniently described through plots in the Stokes space of (S_1, S_3, S_0). These are governed by the intersections between a hyperboloid and a parabola, as dictated by Eqs. (3.46), (3.51) and (3.52),

$$\left(B - \frac{B^2}{4}\right) = S_1^2 + S_3^2 - \left(S_0 - \frac{B}{2}\right)^2, \qquad (3.54)$$

$$S_0 = 1 + \frac{A^2}{B}(2 + gS_3)^2. \qquad (3.55)$$

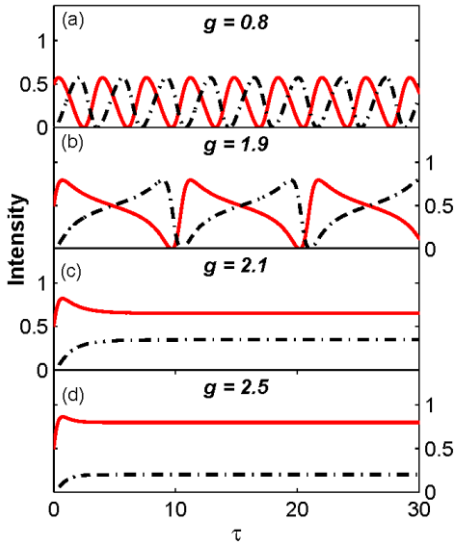

Figure 3.13 The behavior of the intensities over time in the two cavities is shown. The four graphs correspond to the four values of g used in Fig. 3. Parts (a) and (b) depict a Van der Pol-like oscillatory regime and (c) and (d) the PT-broken phase.

Following this approach, it is possible to determine the domains pertaining to instability, i.e. the conditions leading to open-ended intersections or trajectories. When this system is initiated within the linear regime ($|u_0|^2, |v_0|^2 \ll 1$), no such domains of instability were identified as g was varied. To explore the behavior of the system we chose to map the Stokes dynamics on the hyperboloid of Eq.(3.54) since it is independent of g. Figure 3.11 shows relevant plots for four different values of g. For $g < 2$, the Stokes parameters follow periodic trajectories. On the other hand, when $g > 2$, the intersection of the paraboloid and hyperboloid passes through the critical point which is stable under these conditions, see part (iv) of the earlier listed conditions. Here, instead of a periodic evolution, the field values attain a steady state of unequal values analogous to that occurring in a PT-symmetry broken scenario. This case is shown in (c) and (d) of Fig. 3.11. Note that the solution profiles depicted in Figs. 3.11 (a) and (b) indicate the presence of oscillations akin to stable limit cycles. On the other hand, by changing the initial conditions (keeping g

fixed), these orbits become modified. This implies that these are not exactly limit cycles but instead neutrally stable cycles. To demonstrate this, in Fig. 3.12 we set the field in the cavity with gain to be $u_0 = 0.7$ and we then increase the initial value of the field in the cavity with loss. In this case, the cycles in the (S_1, S_0) space are found to change accordingly.

Considering the results presented, one can infer the existence of two distinct responses associated with Eqs.(3.32) and (3.33). The first corresponds to solutions expected in a system like the well-known Van der Pol oscillator [21]. This domain is defined by $g < 2$, and here the intensities in both cavities behave in a very similar manner (reflected versions of each other) having the same period and lying within an identical bounded interval. Whereas in the second regime, the fields are pulled into the stable critical point given earlier in the condition of part (iv). The former relates to the PT-symmetric phase since $|u|^2$ and $|v|^2$ oscillate symmetrically over time, while the latter is analogous to the symmetry broken phase where the two intensities are unequal. Numerical results from a Runge-Kutta simulation for these two phases (corresponding to values of g used in Fig. 3.11) are depicted in Fig. 3.13 where panels (a) and (b) show intensities in the symmetric domain and panels (c) and (d) display the broken phase. In this latter scenario, we also found that the fields in both components of the dimer are locked at the common resonant frequency (or propagation constant) of the cavities (or waveguides) —a feature of a spontaneously broken PT-symmetry. Another characteristic of this PT-phase can be deduced from the fact that as g incereases, the ratio $|v_0|^2/|u_0|^2$ becomes gradually smaller. In addition, once the system starts to oscillate within the symmetric regime, the transition between the two domains occurs at the nonlinear boundary $g = 2$ as the gain-loss value is increased. This is in contrast to a linear PT-symmetric coupler where the transition occurs instead at $g = 1$. Although nonlinear saturation effects tend to modify the location of this transition in the parameter space, the order in which it takes place is not affected-unlike in other nonlinear PT-symmetric settings [18].

Finally, an interesting feature associated with of this oscillator is the fact that within the exact PT-symmetry domain, as the system gets closer to the nonlinear phase transition point, the period of oscillations tens to

approach infinity. Hence, operation close to $g = 2$, for instance in a coupled micro-ring resonator configuration, could lead to periodic flashes of light observable at much longer time scales compared to coupling times which are typically on the order of picoseconds.

3.3. Lasing Dynamics of Non-Hermitian Coupled Fiber Cavities

Since PT-symmetry has been thought of as fragile [22], experimental realizations to date have been usually restricted to on-chip micro-devices. Here, we demonstrate that certain features of PT-symmetry are sufficiently robust to survive the statistical fluctuations associated with a macroscopic optical cavity. We construct optical-fiber-based coupled-cavities in excess of a kilometer in length (the free spectral range is less than 0.8 fm) with balanced gain and loss in two sub-cavities and examine the lasing dynamics. In such a macroscopic system, fluctuations can lead to a cavity-detuning exceeding the free spectral range. Nevertheless, by varying the gain-loss contrast, we observe that both the lasing threshold and the growth of the laser power follow the predicted behavior of a stable PT-symmetric structure. Furthermore, a statistical symmetry-breaking point is observed upon varying the cavity loss. These findings indicate that PT-symmetry is a more robust optical phenomenon than previously expected, and points to potential applications in optical fiber networks and fiber lasers.

Here, we demonstrate that many features of PT-symmetry are sufficiently robust so as to survive the statistical fluctuations associated with macroscopic fiber cavities – even ones having a length in excess of 1 km. Starting from a generic linear PT-symmetric laser cavity model, we construct a conceptually analogous lumped-component model that we experimentally realize in a single-mode-fiber cavity. Coherent coupling and feedback from the interfaces in the traditional model are replaced by partially reflective fiber Bragg mirrors connecting two sub-cavities in which optical amplification and attenuation are provided by localized components in lieu of the distributed gain and loss used in previous approaches. In such an arrangement, the gain-loss balance is readily maintained and varied deterministically, but the sub-cavity phases *cannot* be held fixed due to unavoidable fluctuations in such a large system – thereby leading to

resonance detuning. Nevertheless, we demonstrate experimentally and theoretically that the lasing threshold and the post-lasing output-power scaling in the PT-symmetric configuration survives the statistical detuning effects of the sub-cavity resonances – even when this detuning spans the full FSR. We present the first *quantitative* identification of lasing thresholds and broken and unbroken PT-symmetric lasing phases, which is made possible by the unambiguous separation of the power emitted by the gain and loss sub-cavities. Furthermore, we find that although detuning precludes the existence of an *exact* unbroken PT-symmetric phase, observation of the signature of symmetry breaking is nevertheless enabled through tuning the attenuation of the loss sub-cavity. The demonstrated robustness of PT-symmetry in macroscopic fiber systems could pave the way to applications of such concepts in telecommunications and fiber lasers.

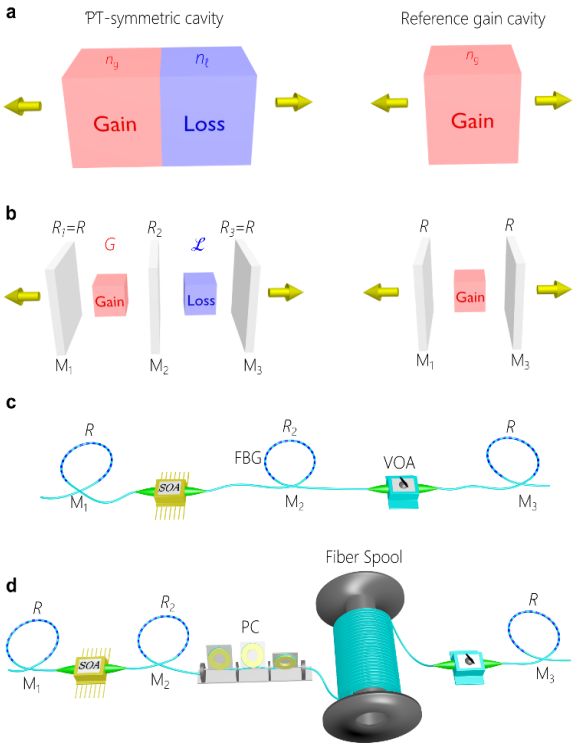

Figure 3.14 A lumped-component model of a PT-symmetric laser cavity. (a), A PT-symmetric structure formed of two homogeneous layers of refractive indices n_g and n_ℓ, (corresponding to optical gain and loss, respectively) and equal thicknesses. PT-symmetry requires $n_g = n_\ell^*$. A continuous version of the reference cavity given in Table 1 (d) is also shown on the right. As a reference, we also depict the gain layer only after removing the loss segment. (b**)**, A model composed of discrete components to replace the continuum model in (a): the interfaces are replaced with localized mirrors, and the distributed gain and loss are replaced

with lumped components – an amplifier (amplification factor G) and an attenuator (attenuation factor $\mathcal{L}$), respectively. PT-symmetry requires that $R_1 = R_3 = R$. The cavity corresponding to the gain layer alone is formed of the side mirrors containing the amplifier. (c), Schematic of an experimental realization of the system shown on the left in (b) using single-mode optical fibers. Specially designed fiber Bragg grating (FBGs) are used as partially reflecting mirrors with reflectivies R, R_2, and R from left to right. Gain is provided by a semiconductor optical amplifier (SOA) and attenuation by a variable optical attenuator (VOA). (d), Optical setup in (c) after inserting an additional 1-km-long fiber spool. A polarization controller (PC) is added to maintain the state of polarization throughout the cavity.

We start by abstracting from an archetypical optical PT-symmetric configuration (Fig. 3.14 (a)) an equivalent discrete 'lumped-component' system (Fig. 3.14 (b)-(d)). The arrangement shown in Fig. 3.14 (a) consists of equal lengths of homogeneous materials of refractive indices n_{g} and n_{ℓ} in intimate contact and surrounded with symmetric external media. The imaginary part of the index corresponds to either optical loss (n_{ℓ}) or gain (n_{g}), depending on its sign. If the indices satisfy $n_{\mathrm{g}}^{*} = n_{\ell}$, then the structure is said to be PT-symmetric. This condition entails that the real part of the refractive index has an even distribution (it is equal in both layers), whereas the imaginary part has an odd distribution (optical gain in one layer and matching losses in the other). Index discontinuities at all three interfaces provide reflection that is particularly weak at the interface between the two layers (where it depends on only the contrast between the imaginary components of n_{g} and n_{ℓ}) – resulting in strong coupling between the two layers. Despite the simplicity of this fundamental model, it has not been experimentally realized to date – in part due to the constraints placed by the Kramers-Kronig relationships on the commensurate values of the real and imaginary components of the refractive index of any material [23]. To date, many physical realizations of PT-symmetric cavities have focused instead on other micro-systems such as coupled ring cavities, or parallel waveguides.

The optical structure shown in Fig. 3.14 (b) that comprises two coupled sub-cavities is conceptually equivalent to that in Fig. 3.14 (a). Fresnel reflection at the interfaces is replaced by partially reflecting mirrors: outer symmetric mirrors M_1 and M_3 having equal reflectivities $R_1 = R_3 = R$ that correspond to the interfaces with the external media, and a middle mirror M_2 of reflectivity R_2 that couples the two sub-cavities and corresponds to the interface between the gain and loss layers. Discrete optical amplifiers and attenuators provide amplification G and attenuation $\mathcal{L}$ in the sub-cavities. Crucially, in such a configuration the reflections are no longer constrained by the physical limitations on the refractive indices of materials as dictated by the Kramers-Kronig relationships. Instead, coherent feedback between the sub-cavities becomes *independent* of the gain/loss contrast.

To realize the lumped-component PT-symmetric structure shown in Fig. 3.14 (b), we have constructed a C-band single-mode-fiber-based cavity in which all the degrees of freedom are independently accessible, as illustrated in Fig. 3.14 (c). Gain is produced by a fiber-pigtailed semiconductor optical amplifier (SOA), the loss is induced by a variable optical attenuator (VOA), and optical feedback is provided by custom-made fiber Bragg gratings (FBG) with desired reflectivity, central wavelength, and bandwidth (Methods). A single polarization is maintained by utilizing a polarization-sensitive SOA and polarization-maintaining optical components. Here we keep the reflectivities of the side mirrors fixed (R, representing left and right external FBGs M_1 and M_3) and vary the reflectivity R_2 for the intra-sub-cavity coupling FBG M_2:

$$R \approx 82\%, R_2 = 7\% - 99\%. \qquad (3.56)$$

In the nonlinear regime, we employ a mean-field temporal coupled-mode approach [44] in which the averaged field amplitudes in the gain sub-cavity a and the loss sub-cavity b are coupled through,

$$\frac{da}{dt} = -\gamma_1 a + i\frac{\Delta}{2}a + \frac{g}{1+|a|^2}a + i\kappa b, \qquad (3.57)$$

$$\frac{db}{dt} = -\gamma_2 b - i\frac{\Delta}{2}b + i\kappa a. \qquad (3.58)$$

Here we have introduced an effective temporal coupling coefficient κ between the sub-cavities (to be defined below); γ_1 and γ_2 are temporal linear losses in the amplifying and attenuating sub-cavities, respectively, which incorporate leakage from the side mirrors and the loss imposed by the VOA; Δ is the frequency detuning between the resonances of the sub-cavities (Fig. 3.15 (a)-(b)); and g is the small-signal gain. These parameters are all related to the mirror reflectivities and fiber lengths. We introduce gain saturation in Eq. (3.58) to capture the power dynamics after the onset of lasing [18]. A useful feature of this model is that it can apply to a wide range of non-Hermitian photonic systems beyond ours. The coupling κ can be obtained from [24,25],

$$\kappa = \frac{v_g}{2n_0^2 L}(1-R)\sqrt{\frac{1-R_2}{R_2}}. \qquad (3.59)$$

In light of the macroscopic nature of the fiber-based cavity, we assume that the detuning Δ is a random variable. Indeed, given the long cavity length, and thus the extremely small free spectral range (FSR), slight perturbations in the experimental conditions may cause Δ to potentially vary across the whole FSR. The solutions are obtained numerically by carrying out an ensemble average over a distribution for Δ, either a Gaussian distribution $P(\Delta) \propto \exp\{-\Delta^2/(2\sigma^2)\}$ (Fig. 3.15 (c)) or a uniform distribution (Fig. 3.15 (d)) as candidate models. Analysis under these considerations leads to the intriguing conclusion that features associated with the presence of an exceptional point (a non-Hermitian degeneracy) can – in principle – still be detected.

The lasing modes can be obtained from Eqs. (3.57) and (3.58) in the steady-state. However, this model is valid both before and after lasing occurs. To ensure the consistency of our analysis, we first obtain the lasing threshold of the PT-symmetric arrangement from the linear transfer matrix method which is given below.

$$G_{\mathrm{PT}} = \frac{1-R}{2\tilde{R}} + \sqrt{1+\left(\frac{1-R}{2\tilde{R}}\right)^2}. \qquad (3.60)$$

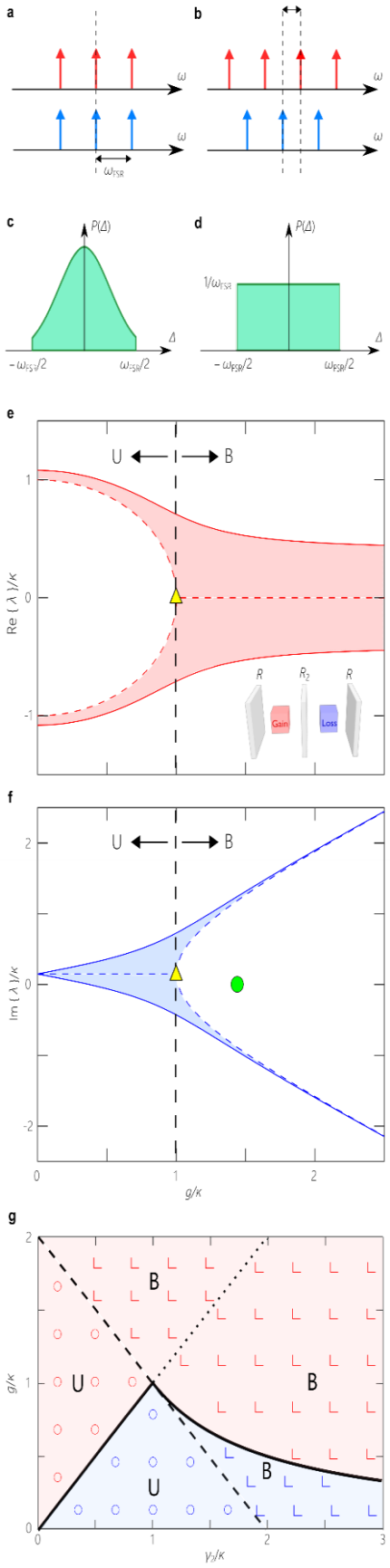

Figure 3.15 (a), Without detuning, the resonance frequencies of the gain (red) and lossy (blue) sub-cavities

are aligned. (b), In the presence of detuning Δ, the sub-cavity resonances are no longer aligned. (c) Gaussian or (d) Uniform distributions as candidates for the detuning probability distribution $P(\Delta)$ (e)-(f), Trajectories of (e) the real and (f) imaginary components of the eigenvalues $\lambda_{1,2}$ for a linear PT-symmetric configuration $g + \gamma_1 = \gamma_2$. Dashed curves represent $\Delta = 0$, and solid curves depict $\Delta = \omega_{FSR}/10$. Shaded regions correspond to all the intermediate detuning values. As g increases, Re$\{\lambda\}$ tend to coalesce whereas Im$\{\lambda\}$ bifurcate. The exceptional point at zero-detuning (yellow triangle) occurs at $g = \kappa$, whereupon Re$\{\lambda\} = 0$ and Im$\{\lambda\} = \gamma_1$. We define a transition between an unbroken PT-symmetric phase (U) and a broken PT-symmetric phase (B) at the EP. Lasing occurs when Im$\{\lambda\} < 0$, which may occur before or after the bifurcation. The green circle depicts the experimental values for the lasing threshold corresponding to $R_2 =$ 6.8%. Inset in (e) shows the PT-cavity configuration. (g), A general schematic for the lasing domains is provided when $\gamma_1 = 0$. Along the dotted line, the PT-symmetric condition $g = \gamma_2$ is satisfied and the dashed line corresponds to $g + \gamma_2 = 2\kappa$. From Eq. (3.61), the system is in the unbroken domain if $g <$ $2\kappa - \gamma_2$ – circles, and is instead in the broken domain beyond this region – edges. The lasing and non-lasing regions are depicted with red and blue colors, respectively. Lasing thresholds are shown with a solid line. In U, lasing occurs when $g > \gamma_2$, whereas in B, when $g > \kappa^2/\gamma_2$.

In Eq. (3.60), $\tilde{R} = \sqrt{RR_2}$. This expression remains unaffected whether the cavities are deterministic or if we assume randomly varying phases inserted in the sub-cavities. The values of gain required for onset of lasing can also be obtained based on Eqs. (3.57) and (3.58). To achieve this, we linearize Eq. (3.57) by ignoring gain saturation and set the detuning to $\Delta = 0$, and then determine the lasing thresholds by assuming a harmonic ansatz of the form $\begin{pmatrix} a(t) \\ b(t) \end{pmatrix} = \begin{pmatrix} a_0 \\ b_0 \end{pmatrix} e^{i\lambda t}$, where $\begin{pmatrix} a_0 \\ b_0 \end{pmatrix}$ is a constant vector. The general solution for the eigenvalues has the form

$$\lambda_{1,2} = -\frac{i}{2}(g - \gamma_1 - \gamma_2) \pm \kappa\sqrt{1 - \left(\frac{g - \gamma_1 + \gamma_2}{2\kappa}\right)^2}. \qquad (3.61)$$

Within the linear, zero-detuning, PT-symmetric configuration ($g + \gamma_1 = \gamma_2$), the two eigenvalues are $\lambda_{1,2} = i\gamma_1 \pm \sqrt{\kappa^2 - g^2}$. The lasing threshold is then easily identified by determining the onset for a negative imaginary component of the eigenvalues, $g_{\text{th}} = \sqrt{\gamma_1^2 + \kappa^2}$. Computing the lasing threshold based on this model Eq. (3.61) reveals excellent agreement with the predictions of the transfer matrix method, Eq. (3.60), for the PT-symmetric structure.

The behavior of the eigenvalues while varying g displays a bifurcation, as illustrated in Fig. 3.15 (e)-(f) (dashed curves). When $g < \kappa$, the eigenvalues have the same imaginary part $i\gamma_1$ but distinct real parts $\pm\sqrt{\kappa^2 - g^2}$. As $g \to \kappa$, the real parts coalesce at zero (Fig. 3.15 (e)) whereas the imaginary components diverge along forked trajectories (Fig. 3.15 (f)). We denote the range $g < \kappa$ as the 'unbroken' PT-symmetry regime (U), and the range $g > \kappa$ the 'broken' PT-symmetry regime (B), separated by the exceptional point at $g = \kappa$. The behavior of the field is quite distinct in these two regimes. The unbroken-PT regime features equal field amplitudes in the two sub-cavities $\binom{a_0}{b_0} = \binom{1}{\pm e^{\pm i\theta}}$, where $\sin\theta = g/\kappa$. The power emitted from the gain and loss sub-cavity ports are thus expected to be equal. In the broken-PT regime, the modal field is more concentrated in the gain (or loss) sub-cavity having unequal amplitudes $\binom{a_0}{b_0} = \binom{1}{ie^{\pm\theta}}$, where $\cosh\theta = g/\kappa$, leading to unequal power emission from the two ports.

We now consider the impact of detuning Δ on the system while retaining the linear PT-symmetric condition ($G\mathcal{L} = 1$). As Δ increases, the bifurcation in the real and imaginary parts of the eigenvalues is 'smoothed out' in a complementary fashion. Prior to the EP, the real part closely resembles the zero-detuning results, but deviates considerably after the EP. The opposite is observed in the imaginary part: it closely follows the zero-detuning results after the EP and diverges beforehand. It can be shown on theoretical grounds that there is an absence of a pure unbroken-PT mode ($|a_0| \neq |b_0|$) in the presence of detuning. We can nevertheless define a pseudo-unbroken symmetry regime, whereupon the amplitudes $|a_0|$ and $|b_0|$ are approximately equal and are affected in a similar manner upon changing the gain and loss [18].

Note that in a *strict* PT-symmetric configuration (the dashed zero-detuning curves in Fig. 3.15 (e)-(f) corresponding to $G\mathcal{L} = 1$), lasing will only occur in the broken-symmetry regime, which has been the case in previous experiments [11,26,27]. This restriction can be relaxed by relying on unbalanced gain and loss ($G\mathcal{L} \neq 1$) [18]. The calculation in Fig. 3.15 (e)-(f) show that detuning $\Delta \neq 0$ can result in lasing in the unbroken-PT regime.

Lately, various models have been put forward to study the interplay of nonlinearity and PT-symmetry [12,13,28,29]. In the structure under consideration, the lasing field dynamics, such as power-scaling with gain, can be conveniently analyzed using the nonlinear model in Eqs. (3.57)-(2.58). An important property of lasing structures in the steady-state is that the saturated gain always clamps to the net amount of attenuation present in the system [15,23]. A critical consequence of this general physical restriction is that the gain/loss contrast no longer determines the transition between different symmetry phases, only the loss does. We confirm this prediction by again employing a harmonic ansatz (with $\Delta = 0$) but without imposing a balance of the gain and loss. Instead we regard them as independent variables. By allowing for only *real* eigenvalue solutions (as a result of gain clamping), we obtain analytical expressions for two distinct phases of field oscillation, which we map to the unbroken (U) and broken (B) PT-symmetry regimes,

$$\gamma_2 \leq \kappa\text{: } \binom{a}{b}_{\mathrm{U}} = \sqrt{\frac{g}{\gamma_1+\gamma_2} - 1}\, \binom{1}{\pm e^{\pm i\theta}} e^{\pm i(\kappa\cos\theta)t}, \tag{3.62}$$

$$\gamma_2 > \kappa\text{: } \binom{a}{b}_{\mathrm{B}} = \sqrt{\frac{g}{\gamma_1+\kappa^2/\gamma_2} - 1}\, \binom{1}{i\kappa/\gamma_2}, \tag{3.63}$$

where the parameter θ in Eq. (3.62) is obtained from $\sin\theta = \gamma_2/\kappa$. Two new features emerge here. In contrast to the linear model in which the gain/loss contrast determines the boundary between the broken and unbroken regimes, here in the nonlinear regime, this boundary is dictated by the loss γ_2 in the lossy sub-cavity alone. The unbroken PT-phase, U, in Eq. (3.62), is characterized by equal intensities $|a|^2 = |b|^2$ in the sub-cavities and the two nonlinear supermodes are split in frequency by $2\kappa\cos\theta$. On the other hand, the broken PT-phase, B, entails an unequal distribution of intensities with $|a|^2 > |b|^2$. Another important feature is that the supermodes now exhibit fixed amplitudes because of nonlinearity, dictated by the cavity gain and loss values, in contradistinction to the linear regime.

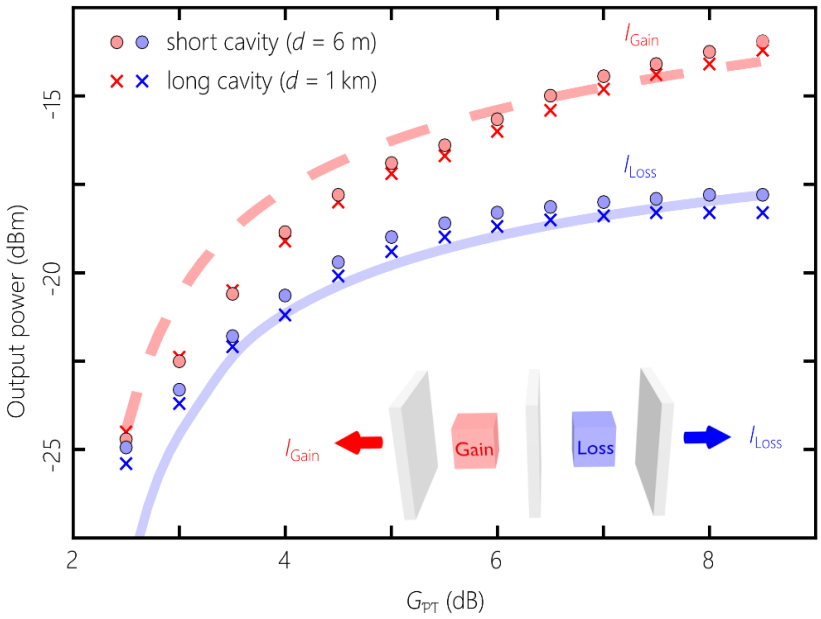

Figure 3.16 Growth in output power from a PT-symmetric laser with gain-loss contrast. Plot of the output power from the loss and gain laser cavity ports as the gain-loss contrast is increased while maintaining PT-symmetry, $G\mathcal{L} = 1$; inset shows the cavity configuration. Measured values are shown as circles and crosses for two different cavity configurations of total lengths $d = 6$ m and $d = 1$ km, respectively. The solid and dashed curves are simulations of the output power from loss and gain ports, respectively, obtained from the nonlinear model of the coupled fiber system in Eqs. (3.57)-(3.58) after making use of the actual experimental values of parameters.

In our experiment conducted on a macroscopic fiber system extending for many meters, a pertinent question is whether the observation of such prominent broken and unbroken phases is still possible in the presence of the unavoidable resonance detunings. As a first demonstration of the validity of the nonlinear analysis described above, we measure the power-scaling characteristics of the $\mathcal{PT}$-laser while holding $R_2 = 6.8\%$ fixed and increasing the gain-loss contrast (maintaining $G\mathcal{L} = 1$). A unique feature of our experimental arrangement is that the output power from the loss and gain sub-cavity ports ($I_{\mathrm{Gain}} = |a|^2$ and $I_{\mathrm{Loss}} = |b|^2$) can be recorded separately and quantitatively; see Fig. 3.16. It is thus possible to determine unambiguously whether lasing is initiated in the broken or unbroken symmetry phases. The data reveals clearly that lasing occurs in the broken regime. Note however that I_{Gain} and I_{Loss} approach each other at low gain/loss contrasts, which indicates that an unbroken phase is approached.

To compare the data on power-scaling with predicted values based on the nonlinear model, we must include the impact of phase detuning in the system of Eqs. (3.57)-(3.58). We compute an ensemble average over a Gaussian distribution for Δ over one free spectral range; Fig. 3.16 (c). The standard deviation σ plays an important role in determining the lasing characteristics. We fitted the results of the coupled model for different values of σ and obtained a good match for $\sigma = \omega_{FSR}/10$. This quantifies the amount of average resonance detuning between the two coupled fiber sub-cavities. Utilizing a uniform probability distribution (Fig. 3.15 (d)) predicts a substantially larger contrast between I_{Gain} and I_{Loss} than that observed experimentally. Furthermore, we inserted an extra 1-km-long fiber spool in the loss sub-cavity (Fig. 3.14 (d)), which exacerbates the detuning between the two sub-cavities. Nevertheless, we observe the same contrast between I_{Gain} and I_{Loss} at the output.

Furthermore, the trends in Fig. 3.16 clearly show that the disparity between I_{Gain} and I_{Loss} continues to grow with g, thus confirming that the mode in the gain sub-cavity further localizes as the gain-loss contrast in the PT-system is enhanced [1-6]. This is a well-known feature of the broken PT phase. Since the steady-states always remain in this phase for the values of $\gamma_2 = g + \gamma_1$ considered here, we deduce from the results in Eq. (3.63) that the range over which the loss (and gain) is varied is actually higher than the coupling

strength between the fiber cavities for $R_2 = 7\%$. It is also interesting that an extremely large cavity (> 1 km) as that employed here does not change the final data as shown in Fig. 3.16 by crosses.

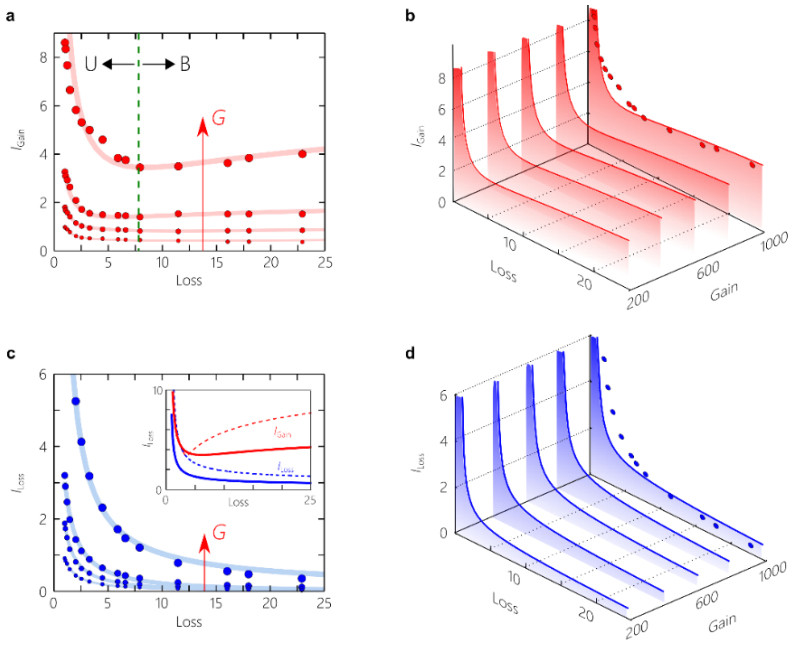

Figure 3.17 Lasing characteristics of the PT-symmetric cavity around the exceptional points. (a), Measured values of the output power from the gain port I_{Gain} (red circles) at different gain values G (30, 25, 20, and 15 dB). The solid curves are fits to guide the eye. As the loss is gradually increased at fixed gain, I_{Gain} is non-monotonic. First I_{Gain} decreases, goes through a minimum at the exceptional point (indicated by the vertical dashed line), and then increases with loss as the gain and loss subcavities decouple. (b), Simulations for I_{Gain} at different values of G obtained from Eqs. (3.57)-(3.58). The red circles correspond to the data in the top-most graph in (a) for $G = 30$ dB. (c), Same as (a) for the power from the loss port – I_{Loss}. Inset shows theoretical plots of I_{Gain} and I_{Loss} at $G = 30$ dB for the statistical PT-symmetric configuration of our experiment (solid curves) and the ideal deterministic configuration (dashed curve – $\Delta = 0$) highlighting the bifurcation in output power as a consequence of PT-symmetry breaking upon passing through the system's exceptional point. (d), Same as (b) for I_{Loss} in lieu of I_{Gain}.

Finally, we demonstrate that our macroscopic fiber-based laser-cavity system – despite the random detuning between the sub-cavities – still displays the features of an exceptional point. As described above,

transitioning between the unbroken and broken symmetry phases in the nonlinear regime (associated with a lasing system in the steady state) is determined by the loss γ_2 alone. In carrying out such an experiment, it is crucial that the gain and loss are tunable in an independent manner and the two output ports are accessible to obtain quantitative results that may be compared to theoretical predictions. Both of these requirements are satisfied in our experimental arrangement.

The loss is tuned via the VOA while the gain provided by the SOA is held fixed at a value well above the lasing threshold of the gain sub-cavity, such that lasing appears in both cavity outputs regardless of the amount of the induced loss. We then sweep the loss of the VOA from zero to a large value while recording the lasing power at the two sub-cavity output ports. Increasing the loss results in a power drop from the loss port as might be expected (Fig. 3.17 (c)-(d)). However, the result for the gain port is counterintuitive: the power initially drops with increasing loss, but then increases with further increase in the added loss (Fig. 3.17 (a)-(b)). This increase in lasing power with additional loss is particularly visible when the gain is held at 30 dB. At a gain of 15 dB, this effect has vanished and a transition is no longer detectable.

Loss-induced enhancement of lasing power has been observed in microcavities and is attributed to the notion of an exceptional point. While the same effect is observed in this macroscopic cavity, it is worth mentioning that there are no pure broken or unbroken phases in this cavity, since the propagation phase is not deterministic. Yet, even in this statistical environment, we have proved for the first time that a PT-phase transition is still observable in large-scale active cavities.

In terms of lasing powers from the gain and loss ports of our system, we have not only observed the two well-known phases of unbroken and broken symmetry in this statistical system but also the transition between the two phases occurring around an exceptional point (EP). The presence of random phase fluctuations has one drawback in the sense that it prevents a complete coalescence of eigenvalues and hence the lasing powers from the gain and loss ports are never equal. More importantly, in this nonlinear system the transition behavior between the unbroken and broken PT-phases is dictated only by the loss in the lossy cavity. Despite the statistical nature of the experimental setup, with increasing cavity loss, optical power

decays in unison from both the loss and gain cavities up to a certain critical point (i.e., the EP) after which it counterintuitively begins to rise from the gain port. Such loss-induced transparency effects and other lasing characteristics had so far been thought to be observable only in micrometer-scale devices. Our results are thus promising in advancing PT-symmetry and non-Hermitian optics in general to large scale non-deterministic platforms such as fiber networks.

3.4. References

[1] K. G. Makris,et. al., Phys. Rev. Lett. 100, 103904 (2008); R. El-Ganainy,et. al., Opt. Lett. 32, 2632 (2007).

[2] A. Guo,et. al., Phys. Rev. Lett. 103, 093902 (2009).

[3] S. Klaiman, U. G¨unther, and N. Moiseyev, Phys. Rev. Lett. 101, 080402 (2008).

[4] S. Longhi, Phys. Rev. A 82, 031801 (2010).

[5] C. E. R¨uter,et. al., Nat. Phys. 6, 192 (2010).

[6] A. Regensburger,et. al., Nature 488, 167 (2012).

[7] E.-M. Graefe and H. F. Jones, Phys. Rev. A 84, 013818 (2011).

[8] T. Kottos, Nat. Phys. 6, 166 (2010).

[9] S. V. Suchkov, et. al., Phys. Rev. A 85, 033825 (2012).

[10] H. Ramezani, et. al., Phys. Rev. A 82, 043803 (2010).

[11] H. Hodaei,et. al., Science 346, 975–978 (2014).

[12] Y. Lumer, et. al., Phys. Rev. Lett. 111, 263901 (2013).

[13] V. Barashenkov and M. Gianfreda, Journal of Physics A: Mathematical and Theoretical 47, 282001 (2014); I. V. Barashenkov, D. E. Pelinovsky, and P. Dubard, ibid. 48, 325201 (2015).

[14] B. E. Little, et. al., J. Lightwave Technol. 15, 998 (1997).

[15] G. P. Agrawal and N. K. Dutta, Semiconductor Lasers, New York (1993).

[16] M.-A. Miri, P. LiKamWa, and D. N. Christodoulides, Opt. Lett. 37, 764 (2012).

[17] C.M. Bender, D. C. Brody, and H. F. Jones, *Phys. Rev. Lett.* **89**, 270401 (2002).

[18] A. U. Hassan, et. al., Phys. Rev. A 92, 063807 (2015).

[19] A. P. Seyranian & A. A. Mailybaev, Multiparameter stability theory with mechanical applications, Vol. 13 (World Scientific, 2003).

[20] M. Wimmer, et. al., Nat. Commun. 6, 7782 (2015).

[21] B. V. der Pol, The London, Edinburgh and Dublin Phil. Mag. & J. of Sci. 2, 978 (1927).

[22] Oliver Bendix, et. al., Physical review letters, 103, 030402 (2009)

[23] B. E. A. Saleh & M. C. Teich, Introduction to Photonics 2nd edn. (Wiley, 2007).

[24] M. B. Spencer and W.E. Lamb, Phys. Rev. A. 5, 884–892 (1972).

[25] M. E. Spencer, and W. E. Lamb, Phys. Rev. A. 5, 893–898 (1972).

[26] L. Chang, et al., Nat. Photon. 8, 524–529 (2014).

[27] M. Brandstatter et al., Nat. Commun. 5, 4034 (2014).

[28] A. U. Hassan, et al., Phys. Rev. E 93, 042219 (2016).

[29] V. V. Konotop, V. V., Yang, J. & Zezyulin, D. A., Rev. Mod. Phys. 88, 035002 (2016).

CHAPTER 4. DYNAMICAL PHENOMENA AROUND EXCEPTIONAL POINTS

In physical systems, a degeneracy occurs if two or more eigenvalues or energy levels coalesce. Degeneracies play an important role in understanding various physical phenomena, from energy levels in atoms to band theory and Zeeman and Stark splitting [1]. The topological structure of these entities has also been extensively explored. One particular example is the accumulation of a geometric phase, known as the Berry phase, upon adiabatic parameter changes around such points [2]. All such effects and similar studies in quantum mechanics were largely restricted to the Hermitian domain where degeneracies only exist for eigenvalues of a system. On the other hand, if one removes this restriction of Hermiticity and considers non-conservative arrangements, better known as non-Hermitian systems, the nature of degeneracies becomes more drastic. At non-Hermitian degeneracies called exceptional points (EPs), not only do two or more eigenvalues coalesce, but their corresponding eigenvectors also merge onto a single eigenvector [3-6]. Some very intriguing phenomena have been found to occur around these non-Hermitian degeneracies including band merging, mode-selection and unidirectional transmission, to mention a few [7-12]. Modulating the governing parameters of the system, such as the gain/loss or coupling strengths, allows for the possibility of tuning the input-output relationship. If one dynamically changes the system parameters along a contour that encloses an EP of order 2 (where two eigenvalues and eigenvectors merge), remarkably only a single eigenstate was found to emerge at the end of the cycle.

Moreover, this effect occurred independently of what input the system was excited with, and the final state just depended on the direction of encirclement around the EP, i.e. clockwise or counter-clockwise. We studied such a dynamical system that comprised two coupled elements that could represent optical/electrical fields in two cavities, waveguides or even the two components of polarized light, e.g. horizontal and vertical polarizations. The coupling strength was considered as constant while variations were introduced in the

gain/loss contrast and propagation constants (or resonant frequencies for cavities) between the two channels. The variations imposed were in the form of circles centered on the location of the EP in the gain(x)-detuning(y) parameter plane. In doing so, we successfully obtained analytical solutions describing the complete field evolution during the parameter cycle. In addition, to prove the existence of a robust mode conversion effect, we used asymptotic expansions of these solutions after an extensive search in the digital library of mathematical functions from NIST. The results obtained firmly establish the fact that in this dynamical evolution, any input leads to the fist eigenvector at the output if the encirclement occurs in a clockwise sense and it instead leads to the second eigenvector if it occurs in the counter-clockwise sense. This was the first analytical explanation of this chiral mode conversion process in non-Hermitian systems. We then used our model to propose an optical omni-polarizing device that is capable of converting any input polarization of light into a desired polarization eigenstate (e.g. horizontal or vertical) along a single waveguide channel. This was designed in a GaAs-AlGaAs ridge waveguide configuration with a slanted side-wall to couple x-y polarizations. The gain and detuning were varied by respectively changing the optical/electrical pump profile and waveguide width along the propagation direction. We are currently pursuing experimental realizations of this physically realizable design on semiconductor platforms and other variants of this design using fiber optics The intriguing topological properties of exceptional points constitute hot research topics and definitely hold promise for developing new and useful optical functionalities.

4.1. Chiral Mode Conversion Through Dynamic Exceptional Point Encirclement

Eigenvectors, by their very nature, are states of a system that remain invariant as they evolve. However, if the Hamiltonian governing the dynamics itself happens to change with time, it becomes naive to expect invariance for any initial eigenstate. One special case is that of cyclic variations whereby the initial and final Hamitonians are equivalent. Here, the excited eigenstate at the start might appear at the end of the cycle given that the so-called adiabatic theorem holds [13]. The theorem holds true but only as far as

Hermitian systems are concerned. Parameter variations in such settings not only introduce the usual dynamical phase but also a measurable topological phase that depends on the geometry of the specific path followed. Better known as Berry's phase, it is a gauge-invariant geometric phase that carries the information of which (parameter) path the system followed, as opposed to the regular dynamical phase that simply depends upon the time it took for the adiabatic cycle [2]. Of particular interest is the case where eigenvalue degeneracies (diabolic points DP) are enclosed within the parameter loop. In this latter scenario, the geometric phase is robust against perturbations in the control path since it is related to the flux generated from the degeneracies that act as topological sources. Since its discovery, it has appeared in widespread manifestations, from optical fibers to neutron beams and can even be used to explain the rotation of the Foucault pendulum [14-16].

Such results were then naturally extended to the non-conservative regime in dissipative systems where, in contrast with the Hermitian case, the complex multipliers of eigenstates no longer have unit moduli [17]. The situation is much different when Hermiticity is dispensed with: the eigenvectors are no longer orthogonal to each other and branch points are known to arise. Recently, there has been a growing interest in the dynamics of systems where parameter excursions occur around such branch points. In these non-Hermitian scenarios, the adiabatic theorem may not hold altogether [18-19]. A peculiar consequence of this is the dominance of one eigenstate over the other depending upon the sense of rotation of the parameter cycle [20-21].

As opposed to DPs in Hermitian systems, where the eigenvalues converge while still supporting linearly independent eigenvectors, a non-Hermitian configuration supports a branch point known as an exceptional point (EP). Here, besides the eigenvalues, the eigenvectors also tend to converge on to a single self-orthogonal eigenvector [3-6] while unfolding associated vectors of the Jordan form [22]. Encircling of EPs leads to richer phenomena such as eigenstate-flips and asymmetric state-exchange mechanisms. Specifically, one eigenstate happens to be preferred over the other depending on the sense of rotation in the parameter space. Recently, two experiments confirming this remarkable phenomenon were reported in

optomechanics [23] and coupled waveguides in the microwave domain [24]. We describe closed form solutions in terms of Hypergeometric functions for the occupancies of two coupled states whose dynamics are governed by a non-Hermitian Hamiltonian undergoing cyclic parameter variations. In the past, a few studies have been aimed at explaining the asymmetry of state exchanges based on numerical schemes but a clear understanding of the dynamics of the process is still lacking. A noteworthy analysis was that of Ref. [25] where a certain non-Hermitian Hamiltonian was shown to possess solutions in terms of Bessel functions and the precedence of one state over the other was traced to the Stokes phenomenon of asymptotics. Our analysis reveals Bessel functions as a special case and the underlying state conversions are shown to unfold through asymptotic expansions of the relevant solutions. We theoretically analyze the behavior of two coupled states whose dynamics are governed by a non-Hermitian Hamiltonian undergoing cyclic variations in the diagonal terms. The model presented here is readily realizable and even more importantly, allows one to track the modal populations at all times without imposing restrictions on the degree of adiabaticity or the size of EP encirclement. Analytical solutions obtained via confluent hypergeometric functions clearly explain the underlying asymmetric conversion into a preferred mode and the chiral nature of this mechanism is brought to the fore through appropriate transformations.

The generic system under consideration is composed of two coupled entities that could represent energy levels, cavities or waveguides. If the respective lifetimes or gain-loss values are different in the two elements, one can reduce the dynamics to a balanced gain-loss form via a gauge transformation. Such a description is then akin to standard parity-time symmetric couplers in optical systems, but with an additional detuning term, that are natural hosts for observing EP-related phenomena. EPs have been reported in a number of other physical systems as well such as in chaotic microcavities and exciton polariton systems. In the Schrodinger description, also applicable to paraxial optics, the dynamics of the optical field are governed by $i\partial_t\psi(t) = H(t)\psi(t)$. Here the time-dependent Hamiltonian is,

$$H(t) = \begin{pmatrix} i\tilde{g}(t) + \tilde{\beta}(t) & -\kappa \\ -\kappa & -i\tilde{g}(t) - \tilde{\beta}(t) \end{pmatrix}. \qquad (4.1)$$

The state vector is given by $\psi(t) = (a(t), b(t))^T$, where $a(t)$ represents the amplitude in the element that undergoes relative amplification, $b(t)$ describes its lossy counterpart, $\tilde{\beta}(t)$ and κ denote the resonance detuning and coupling strength, respectively. Since variations in at least two parameters are required to complete a cycle around an EP, in our analysis we choose the gain-loss contrast $\tilde{g}(t)$ and $\tilde{\beta}(t)$ while assuming the coupling to be fixed over time. It is important to note that other combinations are also possible which might lead to different solutions. Henceforth we use the normalized variables, $(g(t), \beta(t), \tau) = \left(\tilde{g}(t)/\kappa, \tilde{\beta}(t)/\kappa, \kappa t\right)$. The EP in this representation lies at $\left(g(t), \beta(t)\right) = (1,0)$ where the eigenvalues are $\lambda_{1,2} = 0$ with a single eigenvector $\psi = (1, i)^T$. A circular trajectory around this EP is defined by,

$$g(\tau) = 1 - \rho\cos(\gamma\tau)\,,\ \beta(\tau) = \rho\sin(\gamma\tau). \qquad (4.2)$$

This describes a clockwise (c.w.) loop with a radius of ρ ($\rho \leq 1$) and γ being the measure of adiabaticity. A counterclockwise (c.c.w.) loop simply corresponds to $\gamma \to -\gamma$. In analogy with previous studies in PT-symmetric systems, the trajectory is chosen to start ($\tau = 0$) and end ($\tau = 2\pi\gamma^{-1} = \tau_{\text{end}}$) at the point that corresponds to the unbroken PT-symmetric phase (where detuning is zero and the gain-loss contrast is less than the coupling κ) so that one does not have to deal with amplifying or decaying modes at the input-output interfaces in experimental realizations. At these terminal points, the eigenvectors and eigenvalues are $\psi_{1,2} = \left(1, \pm e^{\pm i\theta}\right)^T$ and $\lambda_{1,2} = \pm\cos\theta$, where $\sin\theta = (1 - \rho)$. Notice that $\psi_{1,2}$ are not orthogonal to each other but are in fact biorthogonal with their corresponding left eigenvectors $\tilde{\psi}_{1,2} = \left(1, \pm e^{\mp i\theta}\right)^T$.

The motion of the *instantaneous* eigenvalues and the eigenvector component $b(\tau)/a(\tau)$ is shown in Fig. 4.1 for three types of parameter loops. Figure 4.1 (a) – 4.1 (c) clearly reveals the eigenvalue and eigenvector switching attribute associated with quasi-static EP-encircling [26,27]. In a compact form, it can be described as, $(\lambda_1, \lambda_2) \to (\lambda_2, \lambda_1), (\Psi_1, \Psi_2) \to (\Psi_2, -\Psi_1)$ with reversed signs of eigenvectors for the opposite loop. Most importantly, the gain-loss component of the dynamical phase, $e^{-\int_0^\tau dt' Im[\lambda(t')]}$ where 'Im' represents the imaginary part, is quite different for the two eigenvalue paths. As is shown in Fig. 4.1 (b), one of these

stays longer in the negative imaginary plane and hence experiences a much higher gain compared to the other. This, together with the coupling arising between the *instantaneous* eigenstates due to non-orthogonality in such non-Hermitian settings, leads to the preferential output of the eigenvector associated with the amplified eigenvalue – to give this process an intuitive garb. The fact that no switching of eigenvalues and their associated eigenvectors takes place if the EP is not encircled, is also shown in panels (d)-(f) of Fig. 4.1.

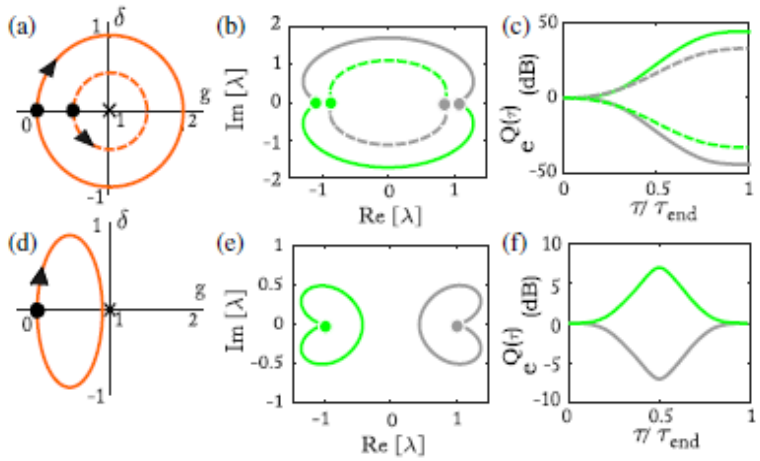

Figure 4.1 The upper [(a)–(c)] and lower [(d)–(f)] panels represent eigenvalue trajectories when the EP (marked with ×) is quasi-statically encircled (a) or excluded (d), respectively, from the parameter loop. Path directions are shown with arrows in (a) and (d) and black dots depict the starting points. Solid lines throughout indicate results for a CW path and dashed lines the CCW. The eigenvalues ($\lambda_{1,2}$) at the start of the loop are depicted as green and gray dots in (b) and (e) where their trajectories are also shown in the corresponding colors.When the EP is enclosed, the eigenvalues swap with each other—(b) and when it is excluded, they return to themselves—(e). The accumulated gain, e^{Q} (see text) corresponding to the different eigenvalue paths is plotted in (c) and (f) against time τ.

Analytical solutions underlying these graphical aides can be obtained by first following the dynamics of a single component of the dimer. Based on the geometry defined in Eq. (4.2), a second order differential equation for each dependent quantity, e.g. for $a(\tau)$, can be expressed as,

$$\gamma^2 \frac{d^2a}{d\tau^2} - \left(\rho^2 e^{2i\gamma\tau} - \rho(2+i\gamma)e^{i\gamma\tau}\right)a(\tau) = 0, \qquad (4.3)$$

At the outset, we would like to mention that if the solutions corresponding to the c.w. loop are obtained, they suffice also for the c.c.w. case. A transformation of the form $(a, b) \rightarrow (a^*, -b^*)$ allows one to immediately write down the field trajectories for the opposite loop.

Hypergeometric solutions – Confluent hypergeometric functions are commonly encountered when solving for the radial component of the wavefunction for atom-like potentials; in describing the velocity distribution of electrons in high frequency gas discharges; and some diffusion problems. To the best of our knowledge, we here report the first occurrence of these functions in the domain of classical optics as a result of dynamically changing the geometry of a wave-guiding element. In Eq (4.3), upon using the substitution $\eta = -2i\rho\gamma^{-1}\, e^{i\gamma\tau}$ and $a(\eta) = e^{-\frac{\eta}{2}}w(\eta)$, the second order differential equation for $w(\eta)$ can be expressed in the degenerate hypergeometric differential form [28],

$$\eta \frac{d^2w}{d\eta^2} + (1-\eta)\frac{dw}{d\eta} - \left(\frac{i}{\gamma}\right)w = 0. \qquad (4.4)$$

This immediately results in the following solution for $a(\eta)$,

$$a(\eta) = e^{-\eta/2}\left[c_1 F_1\left(\frac{i}{\gamma}, 1, \eta\right) + c_2 U\left(\frac{i}{\gamma}, 1, \eta\right)\right].$$

Here F_1 and U are the confluent hypergeometric functions of the first and second kind respectively. The coefficients $c_{1,2}$ depend on the initial conditions concerning the field, $a(0)$ and its derivative at the start. Retracting to the scaled time variable τ, we can express the complete solution in the form of a transfer matrix,

$$\begin{bmatrix} a(\tau) \\ b(\tau) \end{bmatrix} = \sigma(\tau) M_1(\tau) M_2 M_3 \begin{bmatrix} a(0) \\ b(0) \end{bmatrix}. \qquad (4.5)$$

Notice that only the scalar, σ and the matrix M_1 are τ-dependent. These and the other matrices are described below.

$$\sigma(\tau) = i\Gamma(i\gamma^{-1})\gamma^{-2}e^{i\frac{\rho}{\gamma}\left(1+e^{i\gamma\tau}\right)}, \tag{4.6}$$

$$M_1(\tau) = \begin{bmatrix} F_1^{(0)} & U^{(0)} \\ iF_1^{(0)} + 2\rho\gamma^{-1}e^{i\gamma\tau}F_1^{(1)} & iU^{(0)} - 2\rho\gamma^{-1}e^{i\gamma\tau}U^{(1)} \end{bmatrix}, \tag{4.7}$$

$$M_2 = \begin{bmatrix} -\rho\gamma U_{\tau=0}^{(0)} - 2i\rho U_{\tau=0}^{(1)} & -\gamma^2 U_{\tau=0}^{(0)} \\ \rho\gamma {F_1}_{\tau=0}^{(0)} - 2i\rho {F_1}_{\tau=0}^{(1)} & \gamma^2 {F_1}_{\tau=0}^{(0)} \end{bmatrix}, \tag{4.8}$$

$$M_3 = \begin{bmatrix} 1 & 0 \\ (1-\rho)\gamma^{-1} & i\gamma^{-1} \end{bmatrix}. \tag{4.9}$$

The abbreviated forms of the hypergeometric functions, $F_1^{(n)}$ and $U^{(n)}$, represent $F_1(n+i\gamma^{-1}, n+1, -2i\rho\gamma^{-1}e^{i\gamma\tau})$ and $U(n+i\gamma^{-1}, n+1, -2i\rho\gamma^{-1}e^{i\gamma\tau})$, respectively. The generic function $F_1(p_1, p_2, x)$ is single-valued for all complex x, where $p_{1,2}$ are some complex parameters. However, $U(p_1, p_2, x)$ is a many-valued function of x and its principal value is defined in the range $-\pi < \arg(x) \leq \pi$. In the case at hand, starting from -0.5π, the relevant argument $\arg\left(-2i\rho\gamma^{-1}e^{i\gamma\tau}\right)$ reaches π when $\tau = 1.5\pi\gamma^{-1}$. Outside this range, i.e. for $\tau \in [1.5\pi\gamma^{-1}, 2\pi\gamma^{-1}]$, one has to use the connection formula according to [28],

$$U(p_1, p_2, x) = \Gamma(p_2 - p_1)e^{-i\pi p_1}\left[\frac{F_1(p_1, p_2 x)}{\Gamma(p_2)} - \frac{e^{-i\pi(p_2-p_1)}}{\Gamma(p_1)}e^{x}U\left(p_2 - p_1, p_2, e^{-i\pi}x\right)\right]. \tag{4.10}$$

Here Γ is the gamma function. In view of the results above, intensity evolution $(|a|^2, |b|^2)$ in the two coupled entities according to Eqs. (4.6)-(4.9) is shown in Fig. 4.2 for $\gamma = 0.4$ and $\rho = 1$, i.e. $\theta = 0$. Figures 4.2 (a)-4.2 (c) depict the CW case whereas Figs. 4.2 (d)-4.2 (f) show similar results for a CCW scenario. Upon observing the real and imaginary components of the fields, it was revealed that excitation with either of the eigenvectors $|\psi_{1,2}\rangle$ at $\tau = 0$, leads to $|\psi(\tau_{end})\rangle \propto |\psi_1\rangle = \left(1, e^{i\theta}\right)^T$ at the output for a CW loop –

Figs. 4.2 (b) and 4.2 (c). Moreover, $|\psi(\tau_{end})\rangle \propto |\psi_2\rangle = \left(1, -e^{-i\theta}\right)^T$ for a CCW parameter trajectory for both excitations $|\psi_{1,2}\rangle$. The analytic explanation of this mode-conversion follows from first noticing the dependence of the ratio $\chi(\tau) = b(\tau)/a(\tau)$ on the matrix elements of $M(\tau) = M_1(\tau)M_2M_3$ and the initial values $a(0), b(0)$,

$$\frac{b(\tau)}{a(\tau)} = \frac{m_{21}a(0)+m_{22}b(0)}{m_{11}a(0)+m_{12}b(0)}. \qquad (4.11)$$

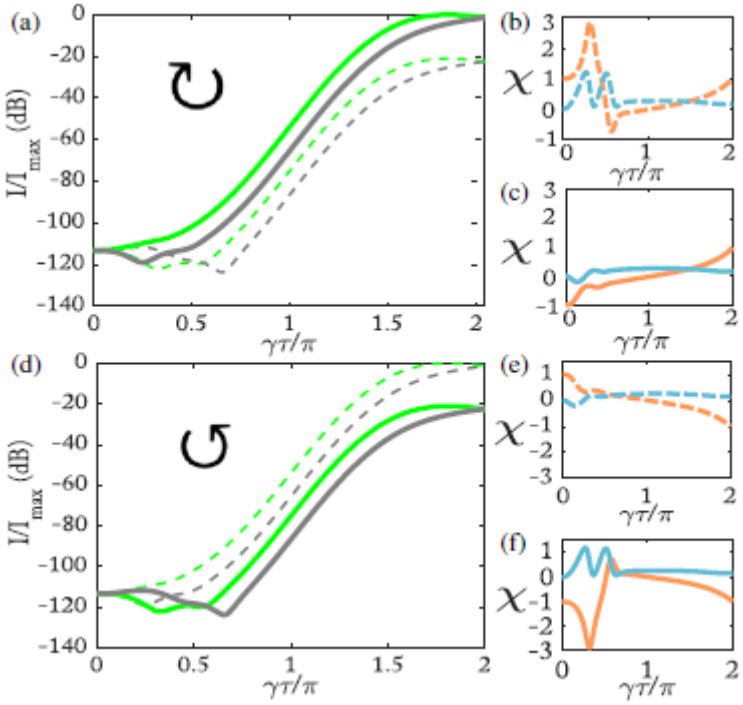

Figure 4.2 Intensity evolutions ($|a(\tau)|^2$, green; $|b(\tau)|^2$, gray) for a CW loop are shown in (a), normalized with respect to the maximum value I_{max}. The real (orange) and imaginary (blue) parts of the ratio $\chi(\tau) = b(\tau)/a(\tau)$ are depicted in (b) and (c). Dashed lines correspond to the input $|\psi_1\rangle$ and solid to $|\psi_2\rangle$. The same scenario for a CCW parameter loop is shown in (d)–(f). At the end of the excursion ($\tau = 2\pi\gamma^{-1}$), in the CW case, $Re[\chi] \to 1$ and $Im[\chi] \to 0$ for both local eigenvector inputs – showing the dominance of the mode $|\psi_1\rangle$. While in the CCW case $Re[\chi] \to -1$ and $Im[\chi] \to 0$, indicating that the mode $|\psi_2\rangle$ is observed at the output.

At the end of the parameter excursion $\tau = \tau_{end}$ the asymptotic behavior of the matrix elements can be shown to assume the form $\frac{m_{21}}{m_{11}} = \frac{m_{22}}{m_{12}} = i + \frac{2\rho F_{1,\tau=0}^{(1)}}{\gamma F_{1,\tau=0}^{(0)}}$. It remains then to observe the expansion of F_1 at $\tau = 0$. Since the terms $i\gamma^{-1}$ and $-2i\rho\gamma^{-1}$ are both large for $\gamma \ll 1$, we use the expansion of $F_1(p_1, p_2, x)$ for large p_1 which is given by [28,29],

$$F_1(p_1, p_2, x) \sim \Gamma(p_2) e^{\frac{x}{2}} (kx)^{\frac{1-2p_2}{4}} \cos\left(2\sqrt{kx} - \frac{\pi p_2}{2} + \frac{\pi}{4}\right), \quad (4.12)$$

where $k = p_2/2 - p_1$. As a result we find that $F_{1,\tau=0}^{(1)}/F_{1,\tau=0}^{(0)} \sim \gamma\left(e^{i\theta} - i\right)/(2\rho)$. This leads to the concluding remark that explains the input-independent mode-conversion process:

$$\frac{m_{21}}{m_{11}} = \frac{m_{22}}{m_{12}} \sim e^{i\theta}. \quad (4.13).$$

Therefore for a CW loop, $\chi(\tau_{\text{end}}) = \frac{b(\tau_{end})}{a(\tau_{end})} \to e^{i\theta}$. Equations (4.11) and (4.13) lie at the heart of our results since they explain in a comprehensive manner why this mode-conversion process takes place, with all possible inputs converging towards $|\psi_1\rangle = \left(1, e^{i\theta}\right)^T$. Moreover, given the fact that $(a, b) \to (a^*, -b^*)$ for the counterclockwise loop, while leaving the matrix elements unchanged, trivially leads to the result that for a CCW encirclement of an EP, $\chi(\tau_{\text{end}}) \to -e^{-i\theta}$. In this case, as a result, the mode that appears at the output is instead $|\psi_2\rangle = \left(1, -e^{-i\theta}\right)^T$.

4.2. Realization of An Optical Omni-Polarizer

In many applications it is often required to control the polarization state at the output of a system. In particular, significant effort has been invested in overcoming the polarization dependent performance of

components such as optical amplifiers and wavelength filters [30]. Based on the results presented earlier, we here propose a single channel omnipolarizer. This structure is expected to transform any input into a desired state of polarization ($|\psi_1\rangle$) when light traverses it in one direction.

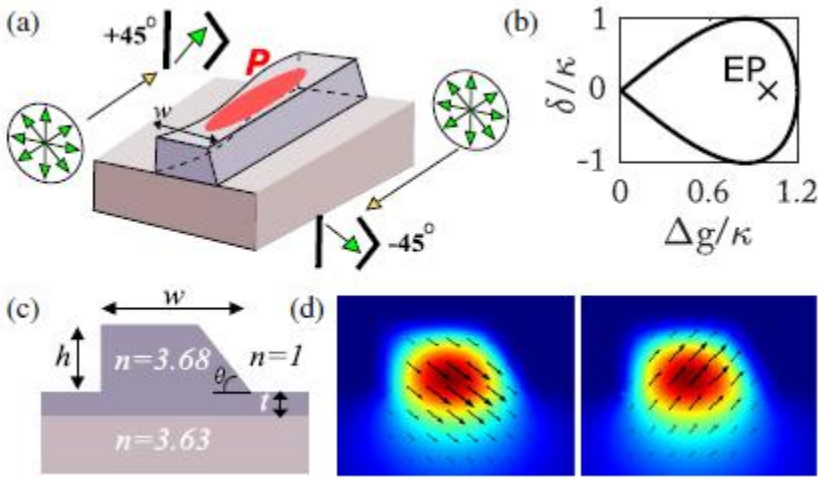

Figure 4.3 (a) A possible realization of an omnipolarizer is shown that highlights the variations in the width—w (sinusoidal) and pumping—P (strongest in the center). Direction-dependent polarization conversions are also schematically illustrated with green arrowheads. (b) To limit the required maximum amplification, the parameter loop around the EP (×) is here chosen to be skewed. Detuning is given by δ and Δg represents the difference between the TE and TM modal gains, i.e.,$(\Delta g = g_x/2 - g_y/2)$. (c) A cross section at $z = 0, \frac{L}{2}$ and L (L—length of the device) is shown where the dimensions are $(h, w, t) = (0.8, 1.42, 0.1)$μm and $\theta = 70°$. In this system h, t, and θ are kept constant throughout, while w varies as, e.g., $w = 1.42 - 0.08\sin(2\pi z/L)$. The refractive indices for this GaAs-AlGaAs structure are also shown in (c) at the wavelength of 800 nm. (d) The two resulting orthogonal eigenmodes with their electric field polarizations.

Conversely, in the opposite direction, any arbitrary input is mapped into the biorthogonal vector ($|\psi_2\rangle$). A possible realization is shown in Fig. 4.3 (a). In this case, the slanted sidewall [31] allows for coupling (κ) between the TE ($\hat{x}$) and TM ($\hat{y}$) polarizations while variations in the width of the waveguide w can introduce a variable birefringence. To achieve the aforementioned conversion of any input to a single polarization, w

and the amount of carrier injection P (optical or electrical) need to be varied along propagation so as to encircle the EP, as shown for example in Fig. 4.3 (b). Note that the w and P are directly related to the detuning δ and the gain differential Δg, respectively. The TE and TM polarization gains vary linearly with P, only the latter being less by a factor of ε, typically $\varepsilon \sim 1-3$. A crosssectional view of this structure is shown in Fig. 4.3 (c) where the birefringence (δ) is negligible and the eigenpolarizations ($\pm 45°$) are $|\psi_{12}\rangle = (1, \pm 1)^T$—Fig. 4.3 (d).

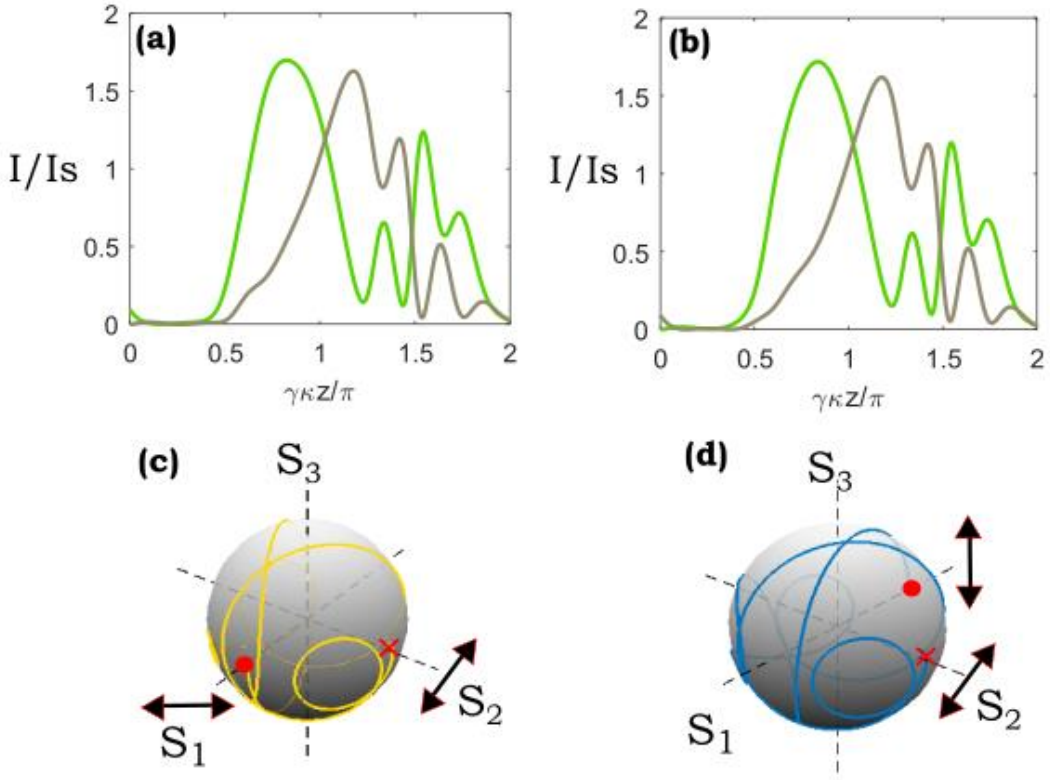

Figure 4.4 Evolution of intensities ($|E_x|^2$, green and $|E_y|^2$, gray) for the nonlinear system are shown in (a) and (b) corresponding to a TE and TM input, respectively. The results are scaled with respect to the saturation intensity (Is) of the gain medium. Polarization dynamics on the Poincaré sphere corresponding to these two cases are depicted in (c) and (d), where yellow dots indicate the input light state and crosses that of the output.

In the design presented, κ remains nearly constant at $\kappa \sim 1.4 \times 10^3$ m^{-1}. The corresponding value of maximum gain (intensity wise) required is 100 cm^{-1} near the middle of the device. Meanwhile w needs to be gradually varied according to $w = 1.42 \rightarrow 1.34 \rightarrow 1.50 \rightarrow 1.42$ μm, as schematically shown in Fig. 4.3 (a). Here the nonlinear evolution dynamics are given by [32],

$$\frac{dE_x}{dz} = \frac{g_x E_x}{1 + |E_x|^2 + \epsilon\left|E_y\right|^2} - (\alpha + i\delta)E_x + i\kappa E_y, \qquad (3.2.11a)$$

$$\frac{dE_y}{dz} = \frac{\epsilon g_y E_y}{1 + |E_x|^2 + \epsilon\left|E_y\right|^2} - (\alpha - i\delta)E_x + i\kappa E_x, \qquad (3.2.11b)$$

where $\alpha \sim 0.9\kappa$ is a linear absorption loss, adiabaticity parameter γ is here chosen to be $\gamma = 0.3$ corresponding to a device length of $L = 1.5$ cm. For a CW loop shown in Fig. 4.3 (b), gain and detuning are dynamically varied as $g_x = 3.6\kappa \sin(\gamma\kappa z/2)$ and $\delta = \kappa \sin(\gamma\kappa z)$ for $\kappa z \in [0, 2\pi\gamma^{-1}]$. The ensuing evolution of intensities $|E_x|^2$ and $\left|E_y\right|^2$, scaled with the saturation level, is shown in Fig. 4.4 (a) for a TE and in Fig. 4.4 (b) for a TM input. Unlike the linear case studied before, here the intensities evolve within reasonable limits due to saturation effects. The nature of the underlying polarization conversion is revealed in Figs. 4.4 (c) and 4.4 (d) where the corresponding field trajectories are plotted on the Poincaré sphere. Clearly, both TE and TM polarizations end up in the same eigenstate, i.e., $+45°$ linearly polarized.

We intend to realize this omni-polarizing functionality via repeated circulation of an optical pulse in a fiber loop. All previous studies in this regard were based on continuous variation of parameters such as gain-loss and detuning between the optical elements. In a fiber loop setting, we create a discrete analog of this process which can be modeled using first order coupled difference equations instead of differential equations. This will not only be a first discrete treatment of dynamic EP-encirclement but it would also provide a mechanism to monitor the polarization state of the pulse along the parameter contour. A schematic of the experimental setup is shown in Fig. 4.5. An optical pulse of a few nanoseconds is injected into the main loop through a 90/10 coupler which then keeps circulating inside in a round-trip time of a few microseconds.

The TE and TM components of the pulse constitute the two coupled channels of this optical system where coupling is introduced using a polarization controller (PC). For EP-encirclement, external modulations would be applied on these two polarization components of the pulse. In this case, the parameter space is comprised of the gain-loss and phase difference between these two orthogonal constituents. For separate control of the TE and TM parts, a small polarizing fiber beam-splitting section is incorporated in the loop. Whenever the pulse traverses this section, the gain-loss difference between the two arms is changed using a $LiNbO_3$ loss modulator whereas the phase difference is modified using a phase-modulator. During this process, the temporal dependence of these variations are imposed in a manner such that the parameters follow a closed contour that includes the EP. In addition, to prevent the pulse from dying out due to losses, an EDFA is included in the main loop that imposes a constant but equal amount of gain in the two polarization components. An exclusive advantage afforded by this fiber based setting is the possibility of monitoring the polarization state of the pulse in each round-trip using a tap-out port connected to a polarimeter.

Figure 4.5 A fiber-based omni-polarizing setup is depicted. An injected optical pulse, shown as green, is split into its TE (blue) and TM (yellow) components in a beam-splitting section. Loss modulation (LM) is imposed in the TE branch whereas phase modulation (PM) is introduced in the TM branch. After these modulated parts are combined together, the pulse passes through a polarization controller (PC) to couple the two orthogonal polarizations. The pulse then goes through an EDFA to in order to compensate for losses. Polarization evolution towards a single state can be monitored on a polarimeter connected via a tap-out port.

We intend to complete this project in the coming few months. During the course of this work, preliminary simulations suggest that after approximately 300 roundtrips, any arbitrary input polarization state is topologically converted into linearly polarized light, described by $(\mathrm{TE}, \mathrm{TM}) = (1,1)$. The chirality of this process becomes evident by simply reversing the direction in which the input pulse is injected inside the fiber loop, keeping the modulation functions the same as before. In this case, the final polarization state is the orthogonal linearly polarized state, i.e. $(\mathrm{TE}, \mathrm{TM}) = (1, -1)$. Our setup also opens up the possibility of studying other linear discrete maps or even non-linear settings such as gain-saturated dynamics through the use of semiconductor optical amplifiers inside the fiber loop. In addition, if one considers higher pulse powers in such optical settings, other nonlinear effects such as self-phase modulation can be induced that would significantly enrich the study of non-Hermitian arrangements. The intriguing topological properties of exceptional points warrant a significant further investigation and definitely hold promise for developing new and useful optical functionalities.

4.3. Chiral Mode Conversion Through Dynamic Loops Not Encolsing An Exceptional Point

A quasi-static encirclement of an EP allows the instantaneous eigenstates to swap with each other [26,27] at the end of the parameter cycle while at the same time imparting a geometric phase [19]. On the other hand, if the same parameters are varied dynamically, i.e. when the field is forced to evolve alongside the parameters, only one of the eigenstates remarkably dominates at the end of the cycle [18,20,21]. Importantly, this effect occurs in a faithful manner and is inherently chiral. Experiments carried out in the microwave [24] and optomechanical [23] domains have recently confirmed this unconventional behavior. An analytical explanation of this asymmetric (or chiral) mode selection mechanism was provided, along with the fact that this effect can persist even in the presence of nonlinearities [33]. In addition, the possibility of a single-channel optical omni-polarizer was proposed. At this point, one might ask the following fundamental question: is this effect exclusive to contours that enclose an EP or is it more generic in nature?

Here we analytically show that this phenomenon can manifest itself under more general conditions. In other words, chiral state conversion can faithfully occur even when the trajectory along which the parameters are varied does not enclose an exceptional point. We demonstrate that in the limit of slow variations, only a single eigenstate will emerge at the output, regardless of initial conditions. In a two-level system, the sense of rotation of the parameters, clock-wise (c.w.) or counter-clockwise (c.c.w.) is the only factor that determines the prevailing eigenstate. The model considered here is exactly solved in terms of Bessel functions, thus allowing one to continuously track the modal populations. Asymptotic expansions of these functions furnish an analytical proof of chiral mode selection *even for non-EP enclosing loops*.

To analyze the dynamics of two coupled states, constantly exchanging energy in space or time, we consider a non-Hermitian Hamiltonian undergoing circular variations in the diagonal terms. For example, in optics, this can be implemented using dielectric cavities (in the temporal t-domain) or waveguides (in the spatial z-coordinate). For this 2×2 system, the modal dynamics obey a Schrödinger-type equation,

$$\frac{id}{dt}\Psi = \begin{pmatrix} ig(t) + \delta(t) & -1 \\ -1 & -ig(t) - \delta(t) \end{pmatrix}\Psi. \qquad (4.14)$$

In Eq. (4.14), the state vector $\Psi(t) = [a(t), b(t)]^T$ describes the optical fields in the two coupled elements. The quantities $g(t)$ and $\delta(t)$ represent variations in the gain/loss and resonance-detuning, respectively. All variables are normalized with respect to the coupling constant (off-diagonal entries). Based on the values $g(t)$ and δ(t) assume at any given time t, the instantaneous eigenvalues λ_i and eigenvectors ψ_i can be always found by using the ansatz $\Psi = \psi_i e^{\{-i\lambda_i t\}}$. A circular trajectory in the (g, δ)-space can be parametrically described by: $g(t) = g_0 - \rho cos(\gamma t)$, $\delta(t) = \rho sin(\gamma t)$. This circle, centered at g_0, has a radius of ρ while γ provides a measure as to how slowly the variations are performed. A c.w. (c.c.w.) loop is described by $\gamma > 0$ ($\gamma < 0$). In this framework, g and δ return to their initial values at the end ($\tilde{T} = 2\pi/\gamma$) of a cycle. Hence the forthcoming discussion is centered on the two eigenvectors corresponding to the terminal point $(g, \delta) = (g_0 - \rho, 0)$. At this location, one obtains,

$$\psi_1 = \begin{pmatrix} 1 \\ e^{i\theta} \end{pmatrix}, \psi_2 = \begin{pmatrix} 1 \\ -e^{-i\theta} \end{pmatrix}. \quad (4.15)$$

The two corresponding eigenvalues are given by, $\lambda_{\{1,2\}} = \pm cos\theta$, where θ can be obtained from $sin\theta = (g_0 - \rho)$he two vectors in Eq. (2) are biorthogonal with the left eigenvectors $\tilde{\psi}_{\{1,2\}} = \left(1 + e^{\mp i2\theta}\right)^{-1}\left[1, \pm e^{\{\mp i\theta\}}\right]^T$, $\langle\tilde{\psi}_m|\psi_n\rangle = d_{mn}$ (d_{mn} represents the Kronecker delta function). In this non-Hermitian arrangement, the point of extreme degeneracy (EP) occurs in parameter space at $g = 1$ and $\delta = 0$, where the two eigenvalues coalesce at $\lambda_{\{1,2\}} = 0$ and the corresponding eigenvectors collapse to $\psi_{1,2} = [1, i]^T$. As previously shown, if this EP is enclosed in a single cycle parameter loop, then any input state will robustly transform into $\psi_{\{1\}}$ if the encirclement is carried out in a c.w. sense. However, upon changing the direction of encirclement to c.c.w., $\psi_{\{2\}}$ instead dominates the output [18].

In what follows, we will reexamine this same effect even when the EP is excluded from the parameter loop. To do so, we recast Eq. (4.14) into a second order differential equation for the first element $a(t)$, according to,

$$\frac{d^2a(t)}{dt^2} = \left[\rho^2 e^{2i\gamma t} - \rho(2g_0 + i\gamma)e^{i\gamma t} + g_0^2 - 1\right]a(t). \quad (4.16)$$

A similar equation also holds for $b(t)$. For all practical purposes, it is sufficient to solve the system of Eq. (4.14) [and Eq.(4.16)] for a c.w. trajectory only. Solutions obtained as such can then be directly used to describe the counterpart c.c.w. case, simply by employing the transformation $(a, b) \rightarrow (a^*, -b^*)$ or by replacing γ with $-\gamma$. In general, Eq. (4.16) can be solved through hypergeometric functions [28]. However, considerable insight into the system's behavior can be gained if we assume small encirclements, $\rho \ll 1$, which allows the ρ^2 term to be neglected in Eq. (4.16). In this case, this system can be reduced to a modified Bessel differential equation of ν^{th}order (one might use the regular Bessel differential equation as well but the asymptotic expansions for the modified equation are much more convenient to deal with). For example, by employing the substitution $x = x_0 e^{\frac{i\gamma t}{2}}$ where $x_0 = 2\gamma^{-1}\sqrt{\rho(2g_0 + i\gamma)}$, one finds that $\nu =$

$2\gamma^{-1}\sqrt{1-g_0^2}$. As in previous studies, $g_0 = 1$ can be used to describe contours that are centered at the EP. Here on the other hand, we allow g_0 to vary in the domain $[0,1]$ when ρ is sufficiently small. Under these conditions, one finds that $a(t) = c_1 I_\nu(x_0 e^{i\gamma t/2}) + c_2 K_\nu(x_0 e^{i\gamma t/2})$ where $c_{\{1,2\}}$ depend on initial conditions and I_ν, K_ν are modified Bessel functions of the first and second kind, respectively, of order ν. From here, one can directly determine the field $b(t)$ in the second element from Eq. (4.14). Therefore, the complete solution of this problem is given by,

$$\Psi(t) = \begin{bmatrix} I_\nu\left(x_0 e^{\frac{i\gamma t}{2}}\right) & K_\nu\left(x_0 e^{\frac{i\gamma t}{2}}\right) \\ i\left(g_0 - \rho e^{i\gamma t}\right) I_\nu\left(x_0 e^{\frac{i\gamma t}{2}}\right) - i\dfrac{dI_\nu\left(x_0 e^{\frac{i\gamma t}{2}}\right)}{dt} & i\left(g_0 - \rho e^{i\gamma t}\right) K_\nu\left(x_0 e^{\frac{i\gamma t}{2}}\right) - i\dfrac{dK_\nu\left(x_0 e^{\frac{i\gamma t}{2}}\right)}{dt} \end{bmatrix} \begin{bmatrix} c_1 \\ c_2 \end{bmatrix}$$

$$\begin{bmatrix} c_1 \\ c_2 \end{bmatrix} = -\frac{2}{\gamma} \begin{bmatrix} i(g_0 - \rho)\, K_\nu(x_0) - i\frac{dK_\nu(x_0)}{dt} & -K_\nu(x_0) \\ -i(g_0 - \rho)\, I_\nu(x_0) + i\frac{dI_\nu(x_0)}{dt} & I_\nu(\eta_0) \end{bmatrix} \Psi(0). \qquad (4.17)$$

Equations (4.17) describe the behavior of the fields in both elements at all times, from the start to the end of the cycle. For slow cycles, where $\gamma \ll 1$, the Bessel functions can be asymptotically expanded in terms of elementary functions in order to find the modal content at the output in terms of the eigenvectors $\psi_{1,2}$. To do so, notice that the time variable only appears in the form of an exponential and results in a complex phase inside the arguments of the Bessel functions. In this regard, the end of the parameter loop amounts to acquiring a phase of $e^{i\pi}$ which reduces the analysis to finding expansions of: $I_\nu(x_0 e^{i\pi}), K_\nu(x_0 e^{i\pi}), I'_\nu(x_0 e^{i\pi})$ and $K'_\nu(x_0 e^{i\pi})$, where prime indicates a time derivative Expansions for either a large argument or a large order do not apply since both ν and x_0 happen to be large in the adiabatic limit (even though $\nu \gg |x_0|$) as $\gamma \to 0$. In fact, one requires uniform asymptotic expansions as given in Eqs. (10.41.3)-(10.41.6) of Ref. [29] where the order and argument simultaneously go to large values. Moreover, to accommodate (cancel out) the extra phase of $e^{i\pi}$, we use analytic continuation according to:

$$I_\nu\left(x_0 e^{\frac{i\gamma t}{2}}\right) = e^{i\nu\pi} I_\nu\left(x_0 e^{\frac{i\gamma t}{2}} e^{-i\pi}\right), \tag{4.18}$$

$$K_\nu\left(x_0 e^{\frac{i\gamma t}{2}}\right) = e^{-i\nu\pi} K_\nu\left(x_0 e^{\frac{i\gamma t}{2}} e^{-i\pi}\right) - i\pi I_\nu\left(x_0 e^{\frac{i\gamma t}{2}} e^{-i\pi}\right). \tag{4.19}$$

Finally, to conform with the notation in Ref. [21], we substitute $z = x_0/\nu$, $\eta = \sqrt{1+z^2} + \ln\left(\frac{z}{1+\sqrt{1+z^2}}\right)$, and using the fact that $|e^{\nu\eta}| \gg |e^{-\nu\eta}|$, which only happens when $\mathrm{Re}[\eta] > 0$, the modal fields at the end of the parameter cycle $\left(\tilde{T} = 2\pi\gamma^{-1}\right)$ assume a simplified structure,

$$\Psi(\tilde{T}) \sim \frac{e^{i\nu\pi}}{\sqrt{2\nu\pi}} (1+z^2)^{-\frac{1}{4}} e^{\nu\eta} \begin{bmatrix} 1 & -i\pi e^{-i\nu\pi} \\ i(g_0-\rho) + \frac{\gamma x_0}{2}\sqrt{1+\frac{1}{z^2}} & -i\pi e^{-i\nu\pi}\left[i(g_0-\rho) + \frac{\gamma x_0}{2}\sqrt{1+\frac{1}{z^2}}\right] \end{bmatrix} \begin{bmatrix} c_1 \\ c_2 \end{bmatrix}. \tag{4.20}$$

To see whether $\Psi(\tilde{T})$ has any semblance of $\psi_{\{1,2\}}$, it is more convenient to convert it into the form $\Psi(\tilde{T}) \propto [1, \chi]^T$, where $\chi = b(\tilde{T})/a(\tilde{T})$. Mode conversion into ψ_1 or ψ_2 would be established only if $\chi \to e^{i\theta}$ or $\chi \to -e^{-i\theta}$, respectively. From Eq. (4.20) it can be found that $\chi \to i(g_0-\rho) + \frac{\gamma x_0}{2}\sqrt{1+z^{-2}}$, and substituting back $z = x_0/\nu$ we directly find that,

$$\chi_{\mathrm{cw}} \to i(g_0-\rho) + \sqrt{1 - g_0^2 + 2\rho g_0} = e^{i\theta}. \tag{4.21}$$

Thus the final state at the output is indeed only ψ_1. The result in Eq. (4.21) holds for a c.w. loop since $\gamma > 0$ was assumed. If instead, one solves for the c.c.w. loop, the only change in the analysis will be a reflection $\gamma \to -\gamma$. In this regard, the following relation can be immediately inferred:

$$\chi_{\mathrm{ccw}} \to i(g_0-\rho) - \sqrt{1 - g_0^2 + 2\rho g_0} = -e^{-i\theta}. \tag{4.22}$$

Here, mode conversion occurs into the state ψ_2 instead. The above results not only prove that robust state conversion is possible even in the absence of an EP encirclement, but also reaffirm the inherent chirality of this process. The reason why this mechanism is input independent becomes clear after inspecting the matrix elements of M in Eq. (4.21) when it is written as $\Psi(\tilde{T}) \sim M[c_1, c_2]^T$. For example, in the c.w. case, both $m_{21} = e^{i\theta} m_{11}$ and $m_{22} = e^{i\theta} m_{12}$, which directly leads to the conclusion that χ is independent of any initial conditions $a(0), b(0)$ – since $c_{1,2}$ are just simple linear combinations of them. Similar conclusions hold for a c.c.w. contour.

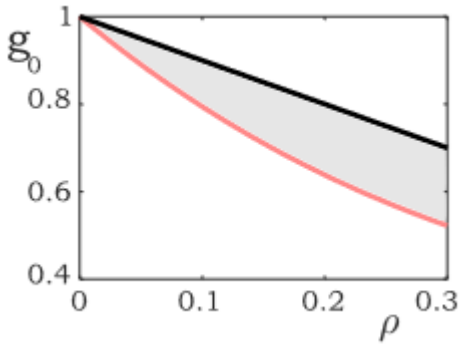

Figure 4.6 Assuming adiabatic conditions (small values of γ), the shaded area shows the range of values of the loop center g_0 and radius ρ, for which chiral mode conversion can take place even without enclosing an EP. Red line is the curve obtained from Eq. (4.23) and the black line depicts the boundary where the loop starts touching the EP located at $(g_0 + \rho = 1)$.

We would like to mention that robust chiral mode conversion is not realized for any arbitrary loop in the $g - \delta$ plane, but takes place only if the loop is close to an EP. Our analysis suggests that as the loop center g_0 moves further away from the EP, the radius of this circle must be kept larger if mode conversion is desired. In this regard, we were able to obtain an approximate analytical form for this demarcation by analyzing the condition, i.e. $Re[\eta] > 0$, so that $|e^{\nu\eta}| \gg |e^{-\nu\eta}|$. For small values of $z = x_0/\nu$, this latter requirement is satisfied provided that the following approximate expression holds true:

$$\rho > 2\left(\frac{1}{g_0} - g_0\right) e^{-2\sinh^{-1}\left(\frac{e}{2}\right)}, \qquad (4.23)$$

where e is Euler's number. The region that excludes the EP but still gives mode conversion is depicted as shaded in Fig. 4.6.

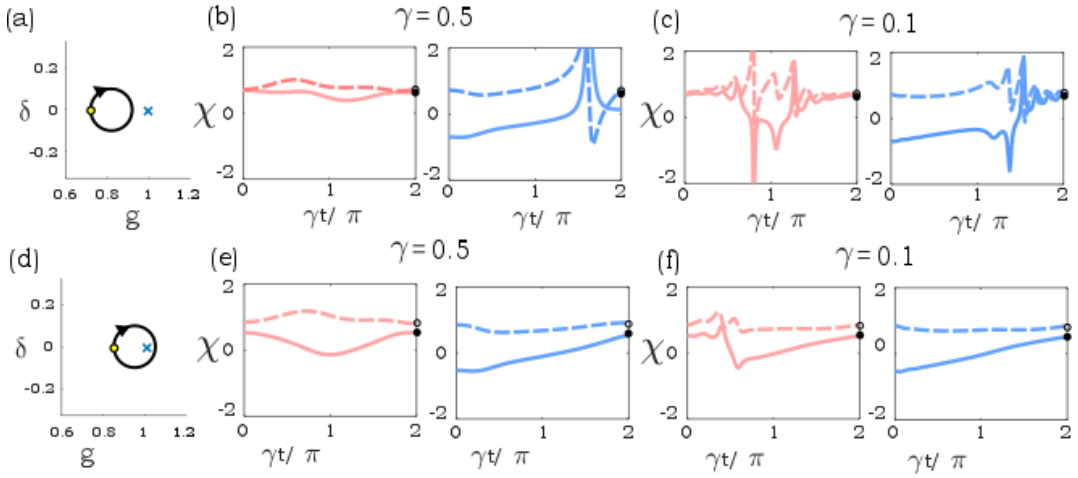

Figure 4.7 Two different c.w. parameter cycles are shown in panels (a) and (d) along with the ensuing behavior of χ in the corresponding panels [(b),(c)] and [(e),(f)] in each row. The loop in panel (a) lies away from the EP (EP is shown as a cross) with $(g_0, \rho) = (0.82, 0.1)$. In the one shown in panel (d), the contour includes the EP with $(g_0, \rho) = (0.95, 0.1)$. The terminal points, where the two eigenvectors $|\psi_{1,2}\rangle$ are found, are marked by a yellow circle and the arrow shows the direction of encirclement. In panels (b) and (e), the resulting variation in χ at all times is shown when the rate of cycling is relatively large, i.e. $\gamma = 0.5$. Plots on the left (shown in red) depict the case when the system is excited with $|\psi_1\rangle$ and those on the right (shown in blue) provide results for excitations with $|\psi_2\rangle$. In these plots, solid (dashed) lines represent real (imaginary) parts of χ. As mentioned in the text, for this c.w. cycle, the state expected at the output is $|\psi_1\rangle$ that corresponds to $\chi \to e^{i\theta}$. The real (imaginary) part of this expected result is shown as a filled (empty) circle at $\tilde{T} = 2\pi\gamma^{-1}$. In the upper panels, these two circles lie very close to each other. In panels (c) and (f), the rate of cycling is reduced to $\gamma = 0.1$ and both excitations end up at the correct location even for the non-EP enclosing case, panel (c). Although mode conversion is not robust in panel (b) (consider the plot on the right), results for the EP-inclusive loop show robust state conversion not only when the encirclement is slow [in panel (f)], but also when it is fast, $\gamma = 0.5$, as in panel (e).

At this point, one might ask what benefit, if any, accrues from including the EP in a dynamic parameter contour, if mode conversion can take place even through non-EP encircling loops? To this end, we found that for a given rate of change of parameters (or adiabaticity γ), mode conversion becomes more robust as the contour moves closer to and eventually encloses the EP. In Fig.4.7, we show two distinct c.w. circular trajectories on the (g, δ)-plane [(a) and (d)], with a radius $\rho = 0.1$. In the upper panel, the loop is deliberately centered at$g_0 = 0.82$ so that it excludes the EP. While in the lower panel, we set $g_0 = 0.95$ so that the EP lies inside the contour. In both rows of Fig. 4.7, the ensuing behavior of χ is shown for $\gamma = 0.5$ [middle column – (b) and (e)] and for $\gamma = 0.1$ [last column – (c) and (f)]. In doing so, the fields were expressed as $\propto [1, \chi]^T$ at all times. When the cycle is not adiabatic enough, both initial eigenvectors, $\psi_{\{1,2\}}$ do not end up in the anticipated location ($\chi \rightarrow e^{i\theta}$), see the right plot in (b). However, when the loop is traversed in a more adiabatic fashion, i.e. $\gamma = 0.1$, state conversion is apparent in (c), even in the non-EP inclusive case. On the other hand, when the EP is located inside the parameter path (lower panel), robust mode conversion takes place for both large (e) and small (f) values of adiabaticity γ. We would also like to point out that for paths that are not circular, e.g. deformed loops, one can still obtain the aforementioned chiral mode conversion – another indication as to how robust this mechanism is.

We have theoretically demonstrated that asymmetric (or chiral) mode conversion is not exclusive to parameter loops that include an EP. Instead, it can also take place even if the contour lies in the vicinity of an exceptional point, provided that the parameters are varied in an adiabatic manner. An immediate ramification of this result could be the potential reduction of the amount of gain-loss contrast needed in coupled optical configurations to observe this effect. For example, instead of cycling around $g = \kappa$ (where κ is the coupling strength), one can achieve the same outcome by staying longer around, say $g = 0.5\kappa$ – hence reducing the maximum amount of gain-loss needed. This could facilitate the observation of the aforementioned chiral effects in various settings such as meta-surfaces and optical waveguide arrangements, as well as in atomic systems [34-36]. The inclusion of nonlinearities in such non-EP enclosing loops could be an interesting aspect for further study.

4.4. References

[1] D. J. Griffiths, Introduction to Quantum Mechanics (2nd ed. Prentice Hall, 2004).

[2] M. V. Berry, Proc. R. Soc. A 392, 45 (1984).

[3] Kato, T. Perturbation Theory for Linear Operators (Springer, 2013).

[4] W. D. Heiss, Eur. Phys. J. D 7, 1–4 (1999).

[5] W. D. Heiss, Phys. Rev. E 61, 929 (2000);

[6] M. V. Berry, Czech. J. Phys. **54**, 1039 (2004).

[7] B. Zhen, et. al., Nature (London) 525, 354 (2015).

[8] A. Regensburger, et. al., Nature (London) 488, 167 (2012).

[9] H. Hodaei, Science 346, 975 (2014);

[10] L. Feng, Science 346, 972 (2014).

[11] Z. Lin, et. al., Phys. Rev. Lett. 106, 213901 (2011).

[12] L. Feng, et. al., Nat. Mater. 12, 108 (2013).

[13] A. Messiah, Quantum Mechanics (Dover, New York, 1961).

[14] A. Tomita & R. Y. Chiao, Phys. Rev. Lett. 57, 937 (1986)

[15] T. Bitter & D. Dubbers, Phys. Rev. Lett. 59 251 (1987)

[16] J. V. Bergmann & H. V. Bergmann. Am. J. Phys. 75 (10): 888–892 (2007).

[17] J. Garrison & E. Wright, Phys. Lett. A 128, 177 (1988).

[18] R. Uzdin, A. Mailybaev, and N. Moiseyev, J. Phys. A 44, 435302 (2011).

[19] I. Gilary, A. A. Mailybaev, and N. Moiseyev, Phys. Rev. A 88, 010102 (2013).

[20] E.-M. Graefe, A. A. Mailybaev, and N. Moiseyev, Phys. Rev. A 88, 033842 (2013).

[21] H. Cartarius, J. Main, and G. Wunner, Phys. Rev. Lett. 99, 173003 (2007).

[22] A. P. Seyranian & A. A. Mailybaev, Multiparameter stability theory with mechanical applications, Vol. 13 (World Scientific, 2003).

[23] H. Xu, et. al., Nature (London) 537, 80 (2016).

[24] J. Doppler, et. al., Nature (London) 537, 76 (2016).

[25] M. V. Berry and R. Uzdin, J. Phys. A 44, 435303 (2011).

[26] C. Dembowski, et. al., Phys. Rev. Lett. 86, 787 (2001).

[27] T. Gao, et. al., Nature (London) 526, 554 (2015).

[28] L. J. Slater, Confluent Hypergeometric Functions (Cambridge University Press, Cambridge, England, 1960).

[29] DLMF, NIST Digital Library of Mathematical Functions, http://dlmf.nist.gov/, Release 1.0.15 (2017).

[30] T. Barwicz, et. al., Nat. Photonics 1, 57 (2007).

[31] B. M. A. Rahman,et. al., J. Lightwave Technol. 19, 512 (2001).

[32] S. Ramanujan, et. al., IEEE J. Quantum Electron. 32, 213 (1996).

[33] A. U. Hassan, et. al., Physical Review Letters 118, 093002 (2017).

[34] M. Kang, J. Chen, and Y. D. Chong, Phys. Rev. A 94, 033834 (2016).

[35] S. Ghosh and Y. D. Chong, Scientific reports 6, 19837 (2016).

[36] H. Menke, et. al., Phys. Rev. A 93, 013401 (2016).

CHAPTER 5. CONCLUSIONS

Non-Hermitian optics is the study of optical structures where the distribution of gain and loss is tailored in a judicious manner – something that leads to various interesting functionalities. In standard quantum mechanics, the possibility of incorporating gain and loss for a particle's wavefunction is an extremely complex problem to deal with, if not altogether neglected because of its absurd nature. However, gain and loss are natural ingredients in many classical optical systems such as photonic waveguides and resonators.

In this dissertation, we have explored how PT-symmetry and its associated degeneracies can be utilized to obtain certain desired outcomes such as significantly enhanced sensitivity of micro-sensors, transverse and longitudinal mode-selection in on-chip ring-lasers and dark-state lasing action. We introduced gain-saturation in these settings which lead to the prediction of anomalous phase transition behavior which we successfully confirmed in a coupled semiconductor micro-ring geometry. The dynamics of gain-loss balanced optical fields, along with their counter-intuitive phase transitions such as loss-induced increase of lasing power, were extended to the statistical domain of fiber cavities.

In the last part of this dissertation, we ventured into the analysis of optical field evolution around non-Hermitian degeneracies known as exceptional points where the system's phase space dramatically reduces. Recently, a quite unexpected behavior was observed upon a dynamic parameter contour around these points, namely, the breakdown of the adiabatic theorem and the dominance of one eigenstate over the other regardless of initial conditions. We were able to rigorously explain this phenomenon using closed form solutions and appropriate asymptotic expansions. Our effort also revealed the possibility of realizing omni-polarizing functionalities based on exceptional points. Such devices are envisioned to convert arbitrary incoming polarizations into a desired polarization state which could have immense implications in fiber transmission systems, for example. It was believed that one necessarily has to include an exceptional point within a parameter contour to obtain the aforementioned behavior. We analytically proved that this is in

fact not the case and that a parameter loop only needs to be adiabatic and to be in the vicinity of an exceptional point to observe such counter-intuitive effects. Such results could reduce the stringent requirements on experimental realizations by bringing the parameter variations to much more accessible domains.